

TEL AVIV UNIVERSITY
RAYMOND AND BEVERLY SACKLER
FACULTY OF EXACT SCIENCES

**Uniformity of detector prototypes for
instrumentation in the very forward
region of future linear colliders**

Thesis submitted toward the M.Sc. Degree
at Tel Aviv University
School of Physics and Astronomy

by

Oron Rosenblat

September 12, 2016

The research work for this thesis was carried out in the Particle Physics
Department of the Tel Aviv University under the supervision of Prof.
Halina Abramowicz and Prof. **Aharon Levy**.

Abstract

The design of the luminosity calorimeter (LumiCal) for a future linear collider is based on a tungsten-silicon sandwich calorimeter. Three silicon-sensor prototypes were tested and characterized in the silicon lab of Tel Aviv University. Results show uniformity among the different sensors. Measured leakage current and capacitance of pads in corresponding sectors of different sensors display similar trends as a function of pad size. An array of four sensors equipped with read-out electronics was tested with 5 GeV muons in CERN's PS test-beam facility. Being the first test with muons, it is an important milestone in the process of achieving stability in sensor response using muon calibration. Results obtained with a muon beam point to a uniform sensor response within each individual sensor, with signals from different pads in the same sensor being in agreement within the uncertainty. However, a slight difference in response was observed among the sensors, with differing signal amplitudes from pads in different sensors. A technique for reconstruction of MIP hit position using charge sharing information is also presented.

Contents

1	Introduction	1
1.1	Future Linear Colliders	1
1.1.1	Why a linear collider?	1
1.1.2	The international linear collider	4
1.1.3	The compact linear collider	5
1.2	Detector concepts	7
1.2.1	The main detector	7
1.2.2	The very forward region	10
1.3	The luminosity calorimeter: LumiCal	11
1.4	Work Scope	13
2	LumiCal sensor prototype	14
2.1	Sensor prototype design	15
2.2	Lab Measurements of Si sensor characteristics	16
2.2.1	System description and measurement	16
2.2.2	Changes and upgrades to the sensor measurement system	17
2.2.3	Capacitance measurements	19
2.2.4	Current measurement	25
2.3	Conclusion	29
3	Beam Test of LumiCal sensor prototype	30

3.1	The proton synchrotron test-beam facility at CERN	31
3.2	The telescope	32
3.3	Beam test setup	33
3.3.1	Physical layout	33
3.3.2	Trigger system	37
3.3.3	Connections and data taking	37
4	Analysis results of data from LumiCal beam test	40
4.1	Tracking information from telescope	40
4.1.1	Signal processing	40
4.1.2	Results	41
4.1.3	Track selection	45
4.2	LumiCal data analysis	47
4.2.1	Signal processing	47
4.2.2	Muon selection	55
4.2.3	Synchronization with telescope and plane alignment . .	57
4.2.4	Sensor signal strength	60
4.2.5	Charge sharing and position reconstruction	66
4.3	Conclusion	74
	Summary	75
	Acknowledgements	76
	Appendix - Additional Plots	77

Chapter 1

Introduction

1.1 Future Linear Colliders

1.1.1 Why a linear collider?

Since the beginning of time man has tried to understand the foundations of nature. At first, theories were drawn up on the basis of mere observations, but with the progress of time and, with it, technological capabilities, precise and complex experiments became the primary source of information.

Today, at the frontier of research of elementary particle physics stands the Large Hadron Collider (LHC). The LHC is a proton-proton collider situated in a circular accelerator of about 27 km in circumference. The LHC aims at the study of the Higgs particle and of rare events with center-of-mass collision energies of up to 14 TeV [1]. The leading theory which exists today in the field of particle physics is the Standard Model (SM) of elementary particles. The LHC, located in a facility of the European Organization for Nuclear Research (CERN), is the platform in which it can be tested, and also in which phenomena beyond the SM may be observed.

LHC began running in 2010, collecting data at 7 TeV center-of-mass energy (CME) through 2010 and 2011 and moving up to 8 TeV CME in 2012. By July 2012, the first objective of LHC was achieved: the discovery of the Higgs boson [2, 3].

The LHC is a very promising discovery machine since both initial state colliding particles (the protons) are complex. Colliding them creates an opportunity for many different and perhaps unknown processes. However, two main disadvantages of hadron colliders like the LHC are worth mentioning:

the first is a loss of precision since the exact properties such as CME or spin state of the constituents of the protons (the partons) cannot be known to a high level of confidence. The second is the fact that since collisions occur between the partons who carry only a certain fraction of the protons' momenta, not all of the CME is available in such a collision. An e^+e^- collider provides an option to not only determine the conditions of the initial state particle but also to set them, and since the accelerated leptons are fundamental particles all of the CME is available in a collision. One might say that an e^+e^- collider is complementary to the LHC; it could allow for deeper and more precise probing of SM processes observed at the LHC (e.g. the Higgs mechanism and electroweak symmetry breakdown) and it would help determine the properties of physics beyond the SM, should it be found at the LHC.

One good example for this is related to the Higgs boson. Once discovered at the LHC, an essential measurement to be made is the magnitude of its coupling constants g_{HXX} , where H stands for Higgs and X can be any other (fermionic or bosonic) field. The SM gives predictions on the expected values of the coupling constants, and these can be checked against experimental results. In table 1.1 (taken from [4]) the expected precisions are presented for LHC and different e^+e^- machines in different operating scenarios, for the couplings of Higgs to particle-antiparticle states. It can be seen clearly that, with the exception of the coupling to photons, e^+e^- machines provide a much better precision than the hadron experiments and thus increase the sensitivity to the discovery of new physics through different processes.

Such an interplay between hadron and lepton colliders has been operated successfully in the past, as in the case of the Super Proton Synchrotron (SPS) and the Large Electron Positron (LEP) colliders. The former was used to establish the SM, while the latter was used for precision measurements. More details about the potential of such an interplay for LHC and a lepton collider can be found in [5].

At CME energies in the TeV scale, the limit has been reached for a circular e^+e^- machines. The power, P , radiated by a charged particle moving in a relativistic circular motion is given by

$$P = \frac{2e^2}{3R^2} \left(\frac{E}{m} \right)^4, \quad (1.1)$$

where e , E and m are the particle's charge, energy and mass, respectively and R is the radius of the circular motion. Due to the power being inversely proportional to the fourth power of the mass, energy losses are very high for light

Facility	LHC	HL-LHC	ILC500	ILC500-up	ILC1000	ILC1000-up	CLIC	TLEP (4 IPs)
\sqrt{s} (GeV)	14,000	14,000	250/500	250/500	250/500/1000	250/500/1000	350/1400/3000	240/350
$\int \mathcal{L} dt$ (fb $^{-1}$)	300/expt	3000/expt	250+500	1150+1600	250+500+1000	1150+1600+2500	500+1500+2000	10,000+2600
κ_γ	5 – 7%	2 – 5%	8.3%	4.4%	3.8%	2.3%	–/5.5/<5.5%	1.45%
κ_g	6 – 8%	3 – 5%	2.0%	1.1%	1.1%	0.67%	3.6/0.79/0.56%	0.79%
κ_W	4 – 6%	2 – 5%	0.39%	0.21%	0.21%	0.2%	1.5/0.15/0.11%	0.10%
κ_Z	4 – 6%	2 – 4%	0.49%	0.24%	0.50%	0.3%	0.49/0.33/0.24%	0.05%
κ_ℓ	6 – 8%	2 – 5%	1.9%	0.98%	1.3%	0.72%	3.5/1.4/<1.3%	0.51%
$\kappa_d = \kappa_b$	10 – 13%	4 – 7%	0.93%	0.60%	0.51%	0.4%	1.7/0.32/0.19%	0.39%
$\kappa_u = \kappa_t$	14 – 15%	7 – 10%	2.5%	1.3%	1.3%	0.9%	3.1/1.0/0.7%	0.69%

Table 1.1: Higgs coupling precision in different facilities and operating scenarios. The parameterization that is used

$$\text{is } \kappa_A = \frac{g_{HA\bar{A}}}{(g_{HA\bar{A}})_{SM}}.$$

particles. As an example, consider an 1 TeV electron travelling in a 200 km radius accelerator (this is much larger than any existing or planned accelerator project). According to equation (1.1) the electron will lose ~ 1 TeV per turn in such a setup. This implies that accelerating electrons to high energies would be technologically and economically feasible only in a linear accelerator, where energy losses are much lower and therefore acceleration to high energies demands less power.

As of today, there are two leading projects for the next high energy linear accelerator to be built: the international linear collider (ILC) and the compact linear collider (CLIC).

1.1.2 The international linear collider

Following many studies in Europe, Asia and the Americas in the past decades, the ILC project is now deep in its technical design phase. On June 2013, a 4 volume technical design report was published [6]. In this report a detailed description of the physics background and physics program for the collider, the accelerator design and the detector design are presented. This document is a very important milestone in the project, testifying to its maturity.

In its foundation, the ILC is a high-luminosity linear electron-positron collider based on 1.3 GHz superconducting radio-frequency (SCRF) accelerating technology. Its CME range is 200-500 GeV. Figure 1.1 shows an overview of the accelerator complex.

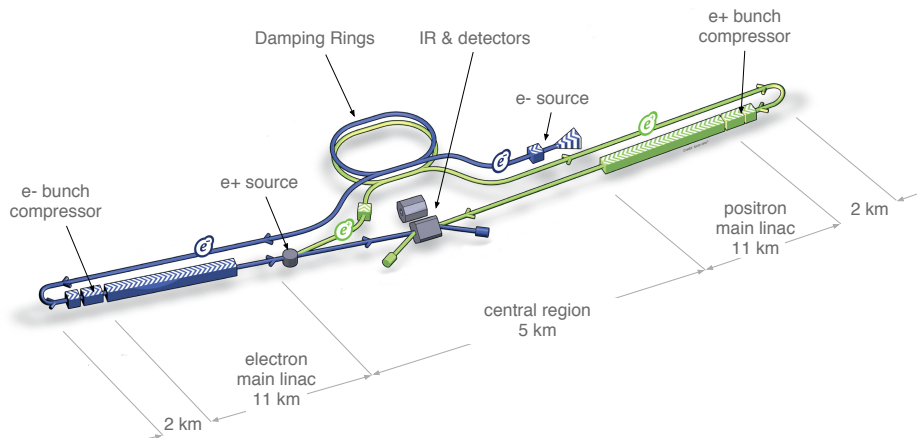


Figure 1.1: Schematic layout of the ILC, indicating all the major subsystems (not to scale).

The ILC is expected to fulfill (among others) the following requirements [6]:

- CME of 500 GeV, upgradable to 1 TeV;
- a luminosity of $1.8 \cdot 10^{34} \text{ cm}^{-2}\text{s}^{-1}$ for 500 GeV CME. For other CME values, luminosity is expected to scale as \sqrt{s} ;
- electron (positron) beam polarization $> 80\%$ ($> 50\%$).

Also emphasized is the ability to scan the available CME energy range, in order to fulfill different running scenarios (e.g as described in [7]). The beam structure is shown in Fig. 1.2. The collider operates at a repetition rate of 5 Hz with a bunch-train length of roughly 1 ms. One bunch-train contains 2625 bunches of $\sim 2 \cdot 10^{10}$ particles.

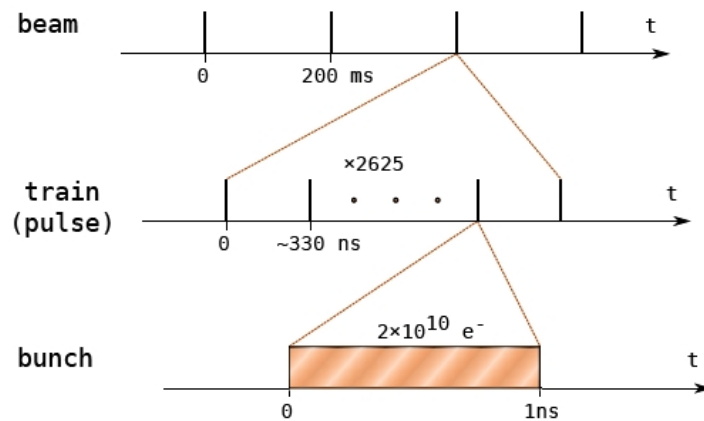


Figure 1.2: The ILC beam structure.

1.1.3 The compact linear collider

The CLIC project is now in the project implementation phase. In February 2012 the first volume of the conceptual design report, the physics and detector volume, were published [8]. Following this, in September-October 2012 two other volumes were released: the accelerator volume [9] and the

program volume [10], which summarizes the two technical volumes and addresses other issues such as schedule and cost. The most current update in terms of the physics case is a report published as an input to the Snowmass process in October 2013 [11].

CLIC offers the option of a linear collider in the CME range of 380 GeV – 3 TeV, using a non-standard acceleration mechanism. Instead of the regular RF accelerating technology (based on cavities), CLIC is based on a two-beam accelerator scheme. As is shown in Fig. 1.3, particles for the main beam are generated and pre-accelerated in the injector linacs. The Drive Beams are generated in two linacs and undergo time compression, resulting in high current and low energy beams. The Drive Beams are then directed to pulsed extraction elements for the final RF power generation, thus accelerating the main beams. The result is a beam with high bunch charge and very small interval between bunches.

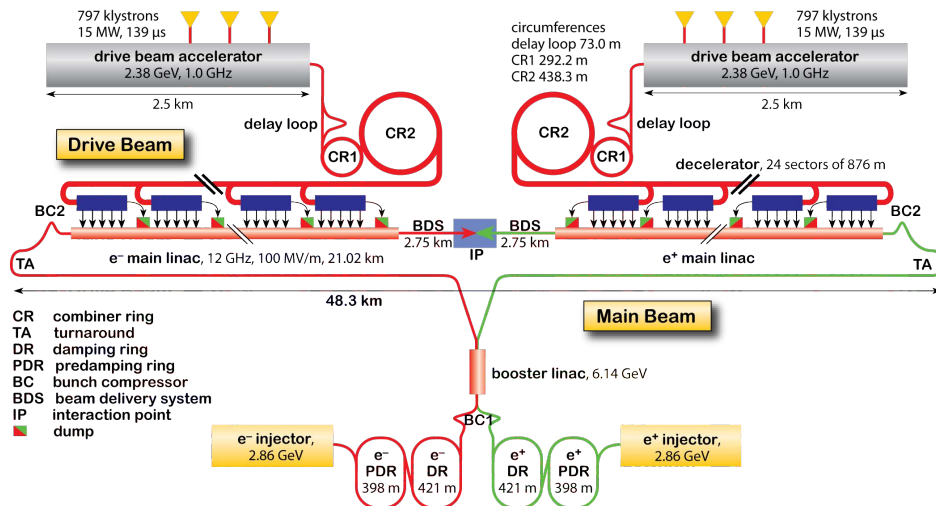


Figure 1.3: CLIC layout at 3 TeV.

The CLIC expected parameters are [9]:

- CME from 380 GeV to 3 TeV;
- a luminosity of $2 \cdot 10^{34} \text{ cm}^{-2}\text{s}^{-1}$;
- bunch charge $3.7 \cdot 10^9 \text{ nC}$, with a separation of 0.5 ns between bunches;
- polarized electron beam (as of now, the positron beam will be unpolarized).

The structure of the beam is similar to that shown in Fig. 1.2. The collider operates at a repetition rate of 50 Hz with a bunch-train length of roughly 150 ns in each repetition. One bunch-train contains 312 bunches of $\sim 4 \cdot 10^9$ particles.

CLIC presents a huge potential but also a great challenge. Achieving the parameters mentioned above must be done in a cost effective, technically feasible manner.

1.2 Detector concepts

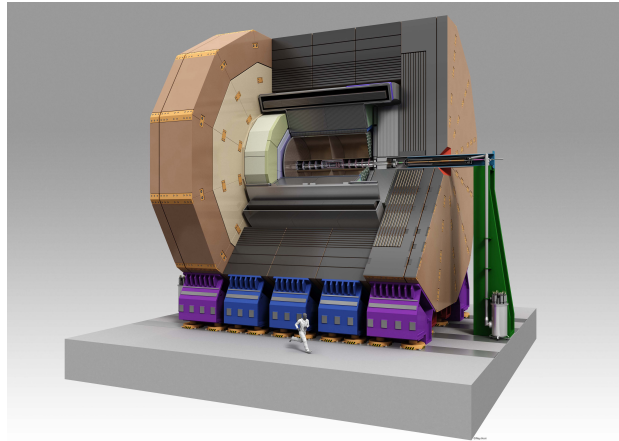
Currently, two detector concepts are being considered for ILC. Data taking will alternate between the two using a push-and-pull scheme, so that while one detector takes data the other will be available for maintenance. Both detectors will contain all the required elements for such experiments: a vertex detector, a tracking detector, a muon spectrometer, a main calorimeter and forward region calorimeters (discussed in Section 1.2.2).

1.2.1 The main detector

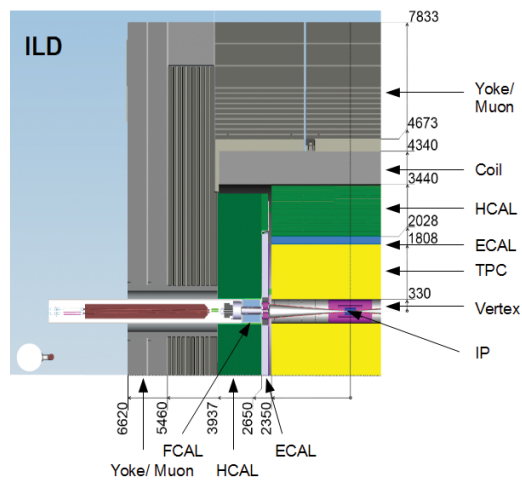
For ILC, the two concepts presented below have been developed into mature designs and were evaluated and validated by the International Detector Advisory Group (IDAG).

The International Large Detector (ILD) concept introduces a large detector with robust and stable performance over a wide range of energies [12]. The concept uses a tracking system based on a continuous-readout time-projection chamber combined with silicon tracking for excellent efficiency and robust pattern-recognition performance. A granular calorimeter system contained inside a 3.5 T magnetic field provides very good particle-flow reconstruction [6]. Figure 1.4 displays the structure of the proposed detector.

The Silicon Detector (SiD) concept is a compact, cost-constrained detector made possible with a 5 T magnetic field and silicon tracking [13]. The highly granular calorimeter is optimized for particle-flow analysis. The structure is shown in Fig. 1.5.

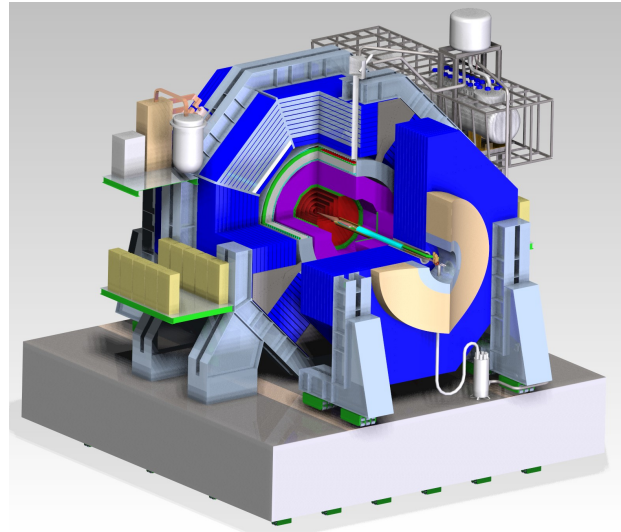


(a)

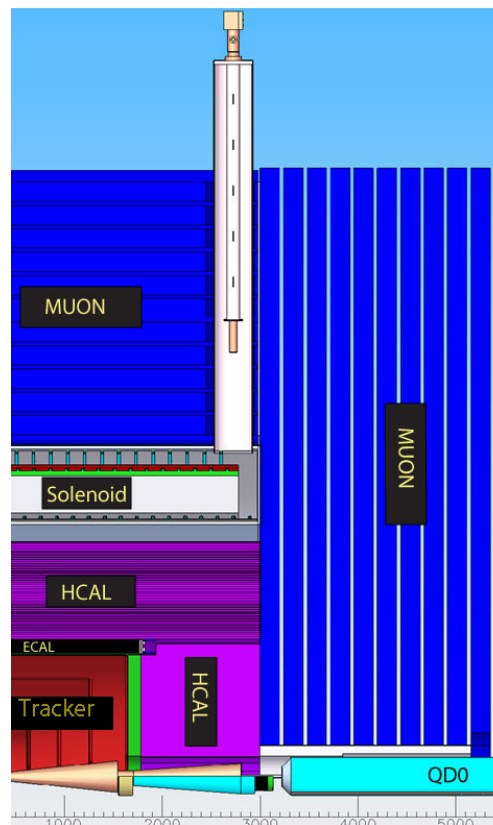


(b)

Figure 1.4: The ILD detector concept. (a) General overview, (b) A longitudinal cross section of a top quadrant, with the interaction point in the lower right corner of the picture.



(a)



(b)

Figure 1.5: The SiD detector concept. (a) General overview, (b) A longitudinal cross section of a top quadrant, with the interaction point in the lower left corner of the picture.

For the case of CLIC, the ILD and SiD designs served as a starting point for the development a single detector concept named CLICdet_2015. Some of the design concepts would be used as are, while others had to be adjusted or completely changed in order to deal with the CLIC environment i.e. 3 TeV CME and 0.5 ns interval between bunches. As of now, a draft of a technical note describing the detector has been written but not yet released. For more details see [14].

1.2.2 The very forward region

Special calorimeters are foreseen for the very forward regions of the linear collider detectors. The first is LumiCal, which will be used to measure the beam luminosity (see also Section 1.3). The second is the BeamCal, positioned adjacent to the beampipe. BeamCal will be used to provide a bunch-by-bunch luminosity estimate and a determination of the beam parameters. LumiCal and BeamCal will improve the hermeticity of the main detector, providing an altogether coverage of almost 4π . Three more detectors are expected in the forward region: a third calorimeter, GamCal, about 100 m downstream of the detector. A pair monitor positioned just in front of the BeamCal which has a fast feedback system to the accelerator. Both GamCal and the pair monitor will be used for beam-tuning. The final detector expected in the forward region is a low angle hadronic calorimeter (LHCAL), extending the coverage angle of the main hadronic calorimeter to the polar angle range of LumiCal.

These forward detectors have to withstand relatively high occupancies, requiring special front-end electronics and data transfer systems. The conceptual designs of the LumiCal and BeamCal are based on the detailed work performed for ILC and documented in [15]. The detector design is similar for both experiments in ILC and CLIC, but the structure of the forward region and the exact position of each element varies according to the specific needs of each project. This of course affects the coverage angle of each calorimeter, as listed in Table 1.2. Figure 1.6 displays for example the forward region of the CLIC detector.

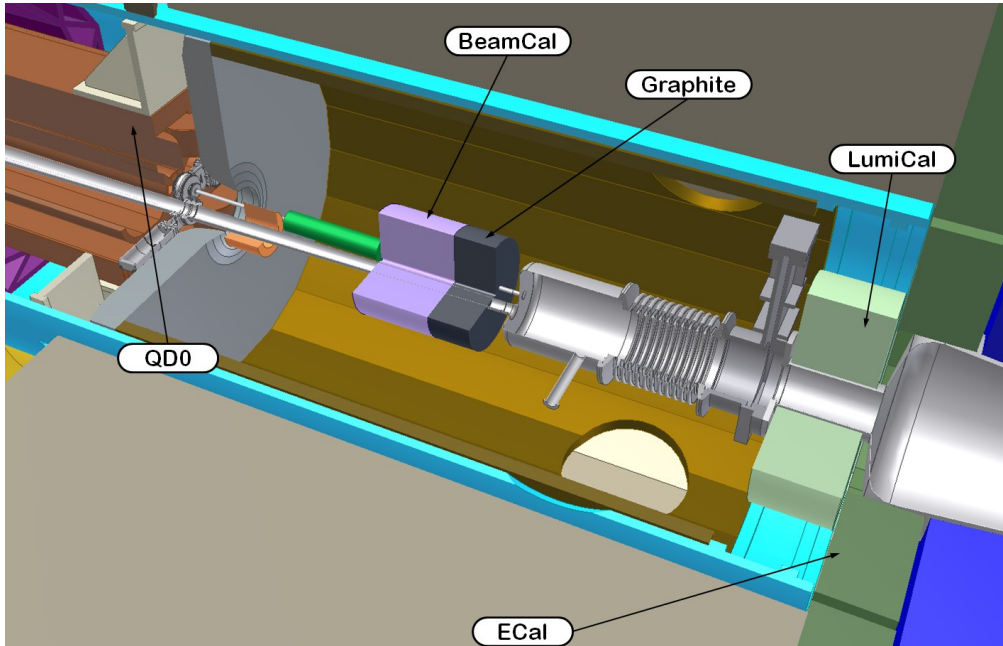


Figure 1.6: The forward region of the CLIC detector.

Table 1.2: Comparison of the LumiCal and BeamCal designs in the ILC and in CLIC.

		ILC(ILD)	CLICdet_2015
LumiCal	geometrical acceptance [mrad]	31 - 77	38 - 110
	fiducial acceptance [mrad]	41 - 67	44 - 80
	z (start from IP) [mm]	2450	2654
	number of layers (W + Si)	30	40
BeamCal	geometrical acceptance [mrad]	5 - 40	10 - 40
	z (start from IP) [mm]	3600	3281
	number of layers (W + sensor)	30	40
	graphite layer thickness [mm]	100	100

1.3 The luminosity calorimeter: LumiCal

Luminosity is a key quantity to extract the cross section values of all physical processes at a given collider. In the linear e^+e^- collider, as in many other e^+e^- experiments, the integrated luminosity will be determined by counting of Bhabha scattering events ($e^+e^- \rightarrow e^+e^-(\gamma)$) and using the well known

theoretical calculation of the Bhabha cross section [16]:

$$\mathcal{L}_{\text{int}} = \frac{N_B}{\sigma_B} \quad (1.2)$$

where \mathcal{L}_{int} is the integrated luminosity, N_B is the number of observed Bhabha events, and σ_B is the relevant cross-section.

Bhabha scattering was chosen since it is a very well known process theoretically in which QED calculations result in a precision of the order of 10^{-3} [17]. Thus, using it as reference process allows for very precise determination of the luminosity.

The main purpose of the LumiCal detector is to determine the luminosity with very good precision by counting Bhabha events. To match the ILC physics benchmarks, an accuracy of better than 10^{-3} is needed at a CME of 500 GeV [12]. For the GigaZ option, where the ILC would be operated for precision measurements at CME energies around the Z boson, an accuracy of 10^{-4} is required [18]. To reach these accuracies, a precision device is needed, with particularly challenging requirements on the mechanics and position control.

Another important purpose for LumiCal is worth mentioning: improving the hermeticity of the main detector by providing identification of electrons and photons at low polar angles.

On the basis of the simulation results presented in [15], mechanical designs of LumiCal were developed. The detector will consist of 30 layers of radiation length tungsten absorbers. Within each layer are silicon sensors providing a coverage of 360° in the azimuthal direction. To allow installation after the beam-pipe is in place, the calorimeter consists of two half-cylinders. Since it is a precision device, special care is devoted to the mechanical stability and position control. The tungsten half-discs are held by special bolts which are stabilized by additional steel rings on both sides of the cylinder. This is depicted in Fig. 1.7.

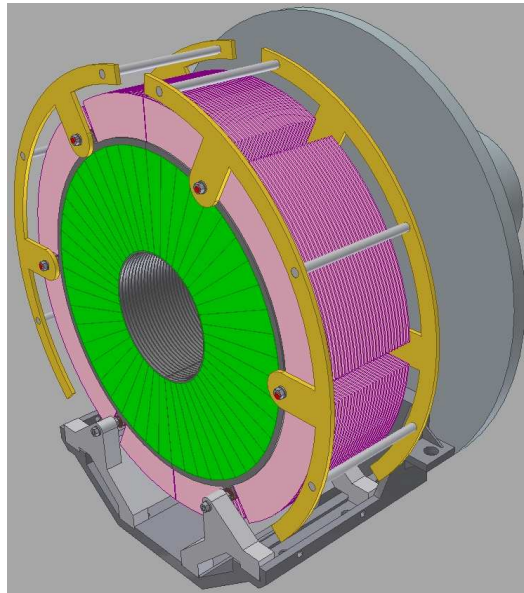


Figure 1.7: The mechanical structure of LumiCal.

1.4 Work Scope

The current development and study of the LumiCal sensor prototype is the general subject of this work.

[Chapter 2](#) presents the design of the manufactured LumiCal silicon sensors, and describes the results of lab measurements performed on prototypes in the Tel Aviv University silicon lab.

The LumiCal sensor prototypes were tested for the first time in a muon test beam at CERN. [Chapter 3](#) describes the general layout of the beam test system, and its results are presented in [chapter 4](#).

A [summary](#) is presented at the end of this thesis.

Chapter 2

LumiCal sensor prototype

Optimization studies [19, 20, 21, 22] of the LumiCal have allowed to design the detector layout as described in Section 1.3. Under this layout, Si sensor tiles were designed. The tiles were custom fabricated by Hamamatsu. As part of the effort to characterize and compare the performances of different tiles and in preparation for bonding of the Si sensor to the readout chain in the Tel Aviv Si laboratory, extensive measurements have been performed on three sensors. The characteristics measurements consist of current and capacitance dependence on voltage. Temperature was controlled by a water based cooling system and humidity was reduced using a nitrogen spraying mechanism.

In total, 40 such sensors were produced: 20 for IFJ PAN Cracow, 10 for DESY Zeuthen and 10 for Tel Aviv University (labeled 13,14,16-18 and 20-24). Previous results from measurements of sensor 16 can be found in [21]. Following the addition of the water cooling system (see Section 2.2.2.2) three sensors were measured,

- sensor 16 was fully measured again, this time under constant temperature;
- sensor 14 was almost fully measured, until in winter 2015 it was found broken inside its case. At the time of writing these lines the reason for the braking remains unknown;
- sensor 17 was also fully measured.

In this chapter the results of the aforementioned measurements are presented. Also, for the first time, a comparison of the results obtained for different sensors is presented.

2.1 Sensor prototype design

As a result of Monte Carlo studies of sensor granularity, each of the 30 Si-layers will be sliced to 48 sectors (7.5° each) in the azimuthal direction which goes around the beam pipe. A single sensor tile contains 4 azimuthal sectors, which for 12 tiles completes a full 360° layer, and is $320\ \mu\text{m}$ thick. In the polar direction, which goes away from the beam pipe, the layers will be segmented to 64 rings. A segment of these rings in each of the sectors is the smallest unit in the sensor and is called a pad. These sensor tiles are made of n-type Si, with p+ strips on n+ back-plane. The Si sensor tiles were produced by Hamamatsu in 2009. An illustration of the sensor can be seen in Fig. 2.1. The Si sensors have the following basic parameters:

- pad pitch 1.8mm;
- pad p+ width 1.6mm;
- pad Al metalization width 1.7mm;
- three guard rings.

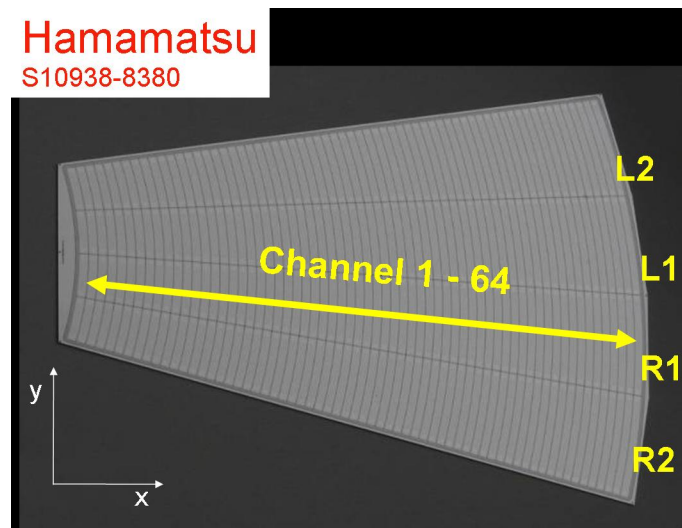


Figure 2.1: The Si-sensor tile with 4 sectors 7.5° each, and 64 pads in each sector.

The guard rings restrict the leakage current from the active sensor area by insulating it from the edge of the sensor. This improves uniformity of the

electric field at the edge of the active area. The guard rings can also be used for detecting leaky pads, since high current from a short-circuited pad inside the active area can be detected by measuring the current flowing through them.

A more detailed description of the sensor tiles can be found in [21].

2.2 Lab Measurements of Si sensor characteristics

2.2.1 System description and measurement

All sensor measurements were held in a "dark box" (see Fig. 2.2) that isolated the sensors from light and was also used as a grounded Faraday cage to shield from electromagnetic noise. For each pad, capacitance, current and temperature as function of voltage were measured. The former two measurements are often referred to as C/V and I/V measurements, respectively.

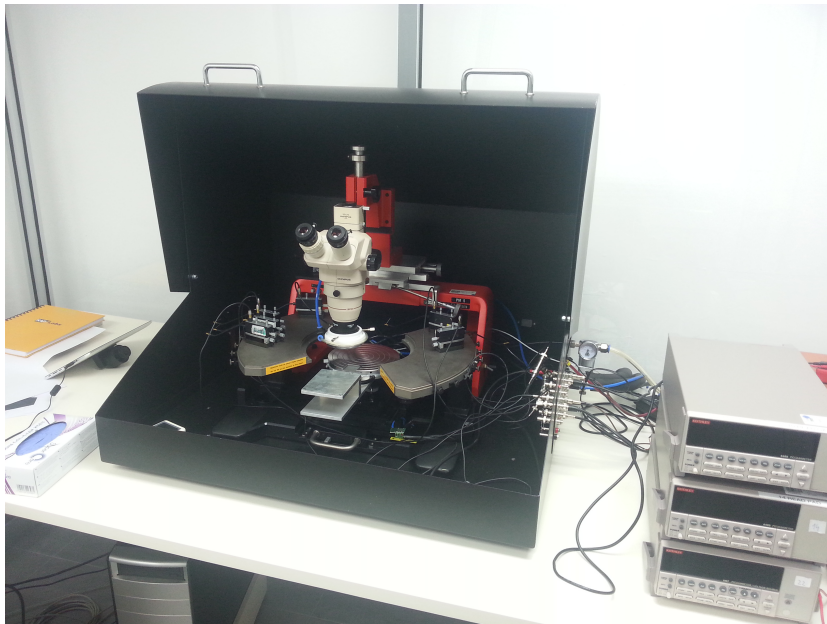


Figure 2.2: The dark box containing the probe station.

Special attention was paid to stabilize the measurement system and to

understand effects of external conditions. The connection scheme is based on the scheme used by our colleagues from DESY-Zeuthen and Cracow, presented in [23, 24].

All measurements were performed while side-neighboring pads in pulse shape formation around the measured pad were grounded and the first guard ring was also grounded via the pico-amperemeter. All of the measurement devices were connected to a data acquisition computer (DAQ) via a general purpose interface bus (GPIB) connection, and operated through a LabVIEW 8.5 program.

In [21] one can find an extensive description of the measurement system and the measurement procedure as they were applied in March 2012. Section 2.2.2 describes the improvements made on the system since that time.

2.2.2 Changes and upgrades to the sensor measurement system

2.2.2.1 Clean room

In the summer of 2014 the construction of a class 10,000 clean room in the Tel Aviv Si laboratory was finalized. Following this, the system was moved to the clean room. Fig. 2.3 displays the measurement system after reassembly in the new location.

2.2.2.2 Temperature monitoring system

It has been shown that the results of the current measurements are strongly dependent on the ambient temperature [21]. For this reason, a cooling system was integrated into the new system.

Cooling was achieved using an **MRC WBL-101** water cooler and a circulation pump (seen in Fig. 2.4a). The point of contact was a thermal chuck on which the sensor was positioned during the measurements. The water temperature could be set, and feedback was taken from a probe inside the cooler which measures the water temperature of the reservoir. The measurements were performed at a setting of 16.5° C, which resulted in a temperature of roughly 19° C on the chuck itself.



Figure 2.3: The Tel Aviv Si laboratory clean room. The sensor measurement system can be seen on the right side of the room. On the left is a bonding machine used to glue sensors to electronic boards.



(a)



(b)

Figure 2.4: The MRC WBL-101 water cooling system: (a) the water cooler. The control panel can be seen on the top; (b) the thermal chuck.

2.2.2.3 Humidity reduction mechanism

Tel Aviv being a coastal city, humidity levels can be rather high, especially during the summer time. In order to keep the surface of the sensor dry (and thus prevent a short between adjacent pads) a humidity reduction mechanism was used. This system contained a small rubber tube situated on the lower part of the microscope used to look at the sensor and position the needles on the pads' probe points (see Fig. 2.5). The tube was connected to a supply of nitrogen gas. Small holes facing downward in the tube create a soft, steady flow of nitrogen on the face of the sensor, preventing the accumulation of moisture.

All measurements (I/V and C/V) were performed while this mechanism was in operation.



Figure 2.5: Rubber tube carrying the nitrogen.

2.2.3 Capacitance measurements

For the C/V measurement the **Agilent 4263B LCR** meter was used. A base voltage in the range of 8 – 150 V with 75 steps was applied on the sensor through a base adapter. All capacitance measurements were performed with a signal amplitude $U = 1$ V and a signal frequency $f = 10$ kHz.

The total capacitance of a given pad is a sum of the geometric capacitance C_g and the inter-pad capacitance C_i , since according to [25] they are connected in parallel. For our sensors, C_g is the dominant factor and dictates the

behavior of the C/V measurement curve according to [26]:

$$C_g = A \frac{\varepsilon_{\text{Si}} \varepsilon_0}{w(V)} = \begin{cases} A \sqrt{\frac{\varepsilon_{\text{Si}} \varepsilon_0 e N_d}{2V}} & \text{for } V < V_d \\ A \frac{\varepsilon_{\text{Si}} \varepsilon_0}{w} & \text{for } V > V_d \end{cases}, \quad (2.1)$$

with the following meaning of the variables: C_g is the geometric capacitance, ε_0 is the vacuum permittivity, $\varepsilon_{\text{Si}} = 11.68$ is the relative permittivity of Si, A is the pad area, V is the bias voltage, V_d is the depletion voltage (see below Eq. (2.2)), $w(V)$ is the depletion layer width, w is the maximum depletion layer width i.e. the width of the sensor, e is the electron charge and N_d is the density of the donor.

Equation (2.1) dictates that for a bias voltage lower than the depletion voltage the width of the depletion layer grows with the voltage and the capacitance should fall as the inverse square root of the voltage. For a bias voltage that is greater than V_d the sensor is already fully depleted and thus a constant capacitance value is expected.

An example of a C/V measurement result displaying this behavior is shown in Fig. 2.6.

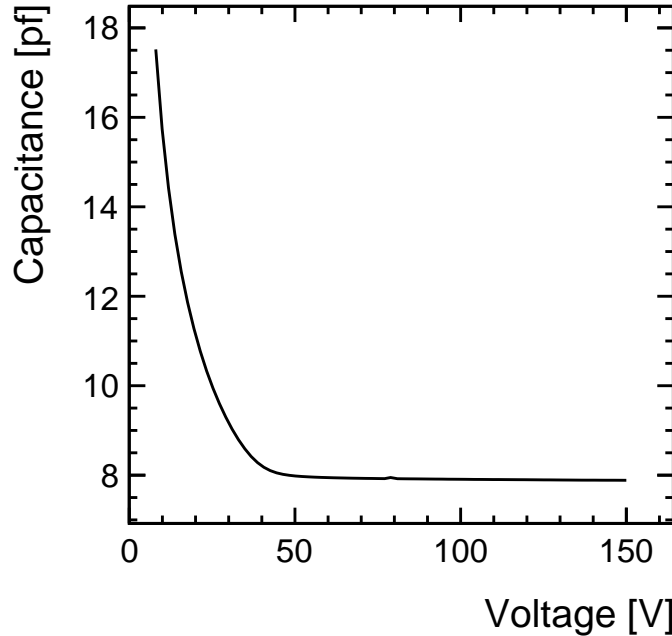


Figure 2.6: A typical curve of a C/V (capacitance vs bias voltage) measurement result for a single LumiCal sensor pad.

The total measured capacitance is estimated as the capacitance in the region $V > V_d$. From Eq. (2.1) a linear dependence on the pad area can be seen. Since the pad area rises linearly with pad number (i.e. the radial distance from the beam pipe) a linear dependence between pad capacitance and pad number is also to be expected.

2.2.3.1 Depletion voltage

As described in Eq. (2.1), the depletion layer width depends on the bias voltage applied on the diode. When the depletion layer width reaches its maximum, the diode is fully depleted. The maximum width is limited by the thickness of the sensor. The voltage needed to extend the depletion layer to the full thickness of the sensor is the depletion voltage, V_d and can be described as

$$V_d = \frac{eN_d d^2}{2\epsilon_0 \epsilon_{Si}}, \quad (2.2)$$

where d is the sensor thickness. Under normal operating conditions, only the charge produced in the depleted volume can be detected, therefore the maximal signal charge is detectable when full depletion is reached. This means that the sensor operating voltage must be higher than V_d . For this reason, V_d must be determined from the measurements. From Eq (2.2) it is clear that the size of V_d is independent of pad size or the relative location on the sensor. Therefore, different pads from different locations and even from different sensors (assuming thickness is identical) should have the same depletion voltage.

As seen in Eq. (2.1), V_d can be extracted from a C/V curve as the voltage where capacitance behavior as a function of voltage changes. This is preformed using the $\ln(C)/\ln(V)$ plot, by finding the crossing point between two linear fits, as shown in Fig. 2.7. In this example, as in many others, a slight descent in the capacitance value is observed for $V > V_d$. This is contrary to Eq. (2.1) and can be explained by the fact that some contribution from the inter-pad capacitance C_i exists, since only directly neighboring pads were grounded during the measurement. Although these provide the most significant contribution to C_i , in an ideal case all of the pads in the sensor should be grounded [26].

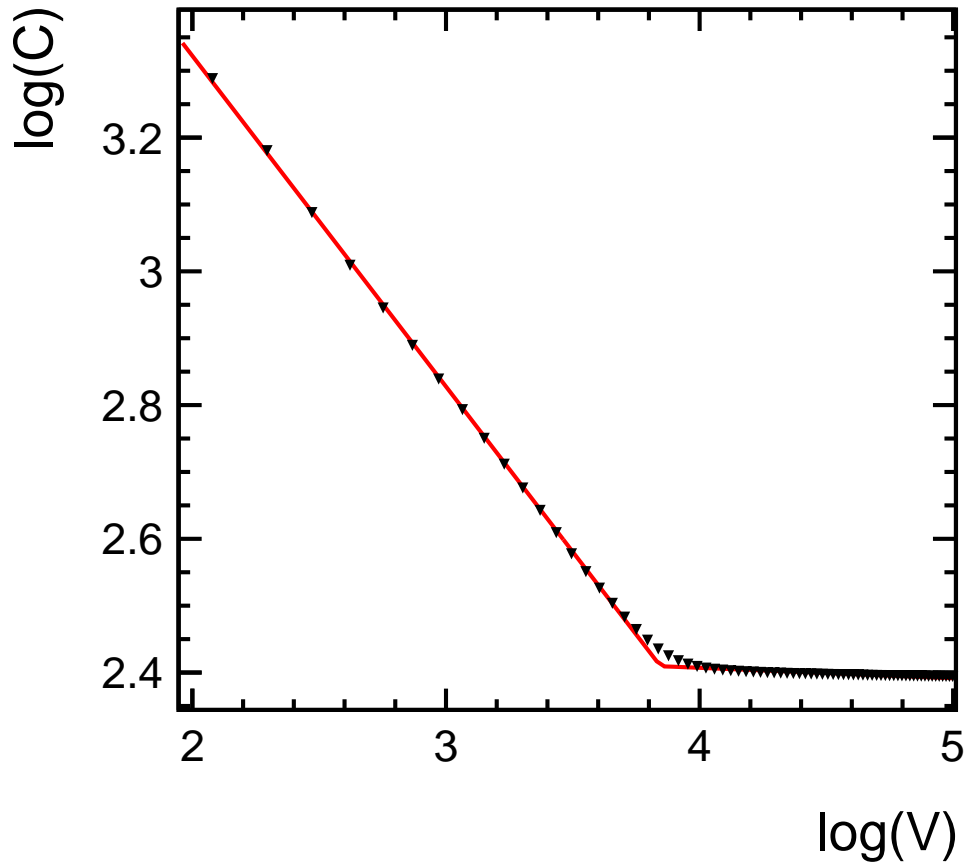


Figure 2.7: Determination of depletion voltage from a $\ln(C)/\ln(V)$ curve of capacitance measurement result. The red lines are the result of the linear fits used to find the depletion voltage.

2.2.3.2 Results

In Fig. 2.8, measured capacitance is plotted against pad number for all four sectors. The results from all three sensors are plotted together for comparison.

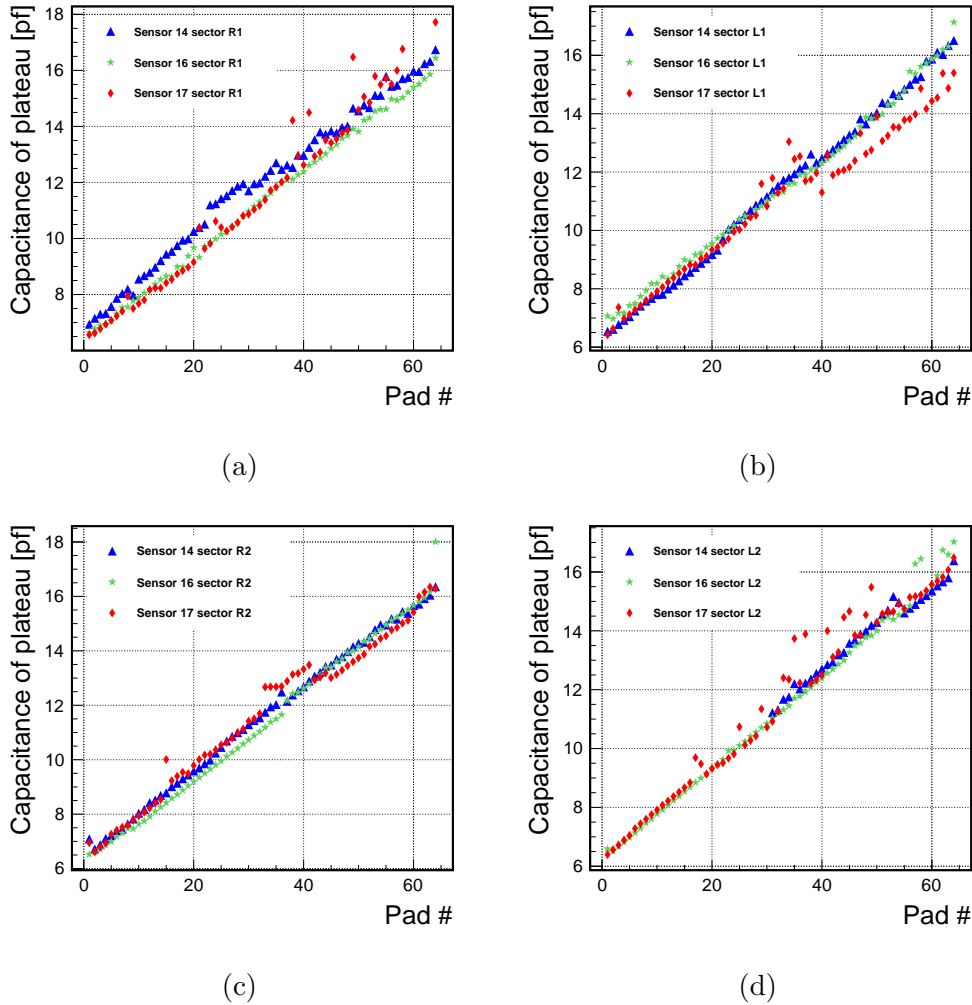


Figure 2.8: Capacitance vs pad number in sectors R1, L1, R2 and L2 (see Fig. 2.1) on plots (a) - (d) respectively. The blue, green and red datasets correspond to sensors 14, 16 and 17, respectively.

A very clear linear trend can be observed for all sectors in all sensors, corroborating the claim that for the LumiCal sensors capacitance is mainly a geometrical quality. A series of points in sector L1 of sensor 17 display capacitance values which are lower than the general trend. These measurements were performed in a single day and could not be repeated. This emphasizes the fact that measurement results are very sensitive to laboratory conditions (e.g. temperature). Apart from this, few other points deviate from the trend, probably due to small imperfections on the sensor surface (tiny scratches, dust etc.) or as a result of noise during the measurement. Some

points from sensor 14 are missing since it was broken before the measurements were completed. Five points in sector R1 of sensor 17 were omitted due to a scratch in this area of the sensor which led to very high capacitance results, which can be seen in Fig. A.1 in the Appendix.

Comparison among the different sectors implies that the capacitance is indeed independent of pad sector. No clear difference exists among the different sensors.

The distribution of V_d , determined for all pads, is presented for the three sensors in Fig. 2.9. It can be seen that for all pads, full depletion occurs in the range 35 – 70 V, with no substantial difference among the different sensors. This result is in rough agreement with past measurements [21, 23].

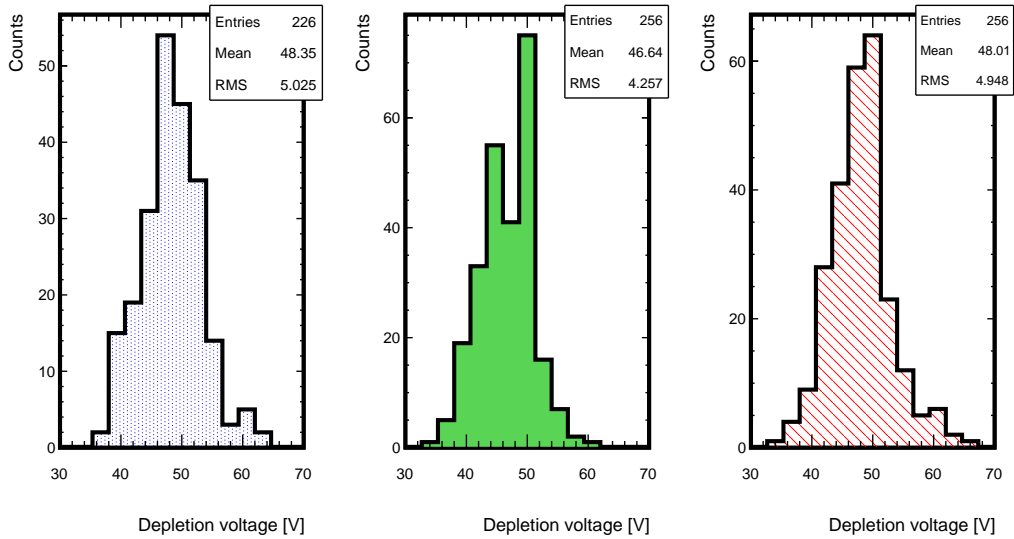


Figure 2.9: Depletion voltage histograms for all measured pads in the three sensors. The left, middle and right histograms correspond to sensors 14, 16 and 17, respectively.

The uncertainty on the calculation of the depletion voltage (as resulting from the fit described in Section 2.2.3.1) is estimated to be less than 1 V in the majority of the cases, indicating that the range of the values represents genuine differences among the pads. Since Eq. 2.2 predicts a certain value for V_d which is independent of pad size, no such difference is expected.

Experimental and physical factors may be at the origin of the wide spread of values obtained for V_d . Experimental factors that may have caused for a bias

in the estimation of V_d are mostly a result of the sensitivity of the measurement system. Since the measured values are very small, even the slightest interference such as dust on the surface of the pad or a weak electrical field from a nearby instrument may cause a shift in the result. Furthermore, the fitting procedure used to find the value of V_d is quite sensitive to "stray" points: even a small number of points that deviate from the trend may shift the result of the fitted value, as shown in Fig. A.3 in the Appendix. It should also be noted that the measurements were performed manually over a long period of time, during which the system's conditions (e.g. the electronic noise) may have changed.

There are also physical reasons that may account for the variance obtained in V_d values. Although there is no dependence on pad size in Eq. 2.2, there are two other factors that may vary in different areas of the same sensor in the production process. These are the sensor width d and the density of the donor, N_d , where V_d depends quadratically on the former and linearly on the latter. The LumiCal prototype was manufactured with a tolerance of $\pm 15 \mu\text{m}$ on the width [23]. This, along with the fact that the donor density has been found to vary among different measurements (e.g. comparing results from [23] and [21]) is another possible explanation for the wide range of values obtained for V_d .

In spite of the above, the results in Fig. 2.9 show that the average depletion voltage is in the range $46.5 - 48.5 \text{ V}$ with a spread of $\pm 5 \text{ V}$.

In order to ensure proper operation, the operating voltage should be higher than 70 V . The reason for this is that under this voltage all of the pads will be fully depleted, enabling detection of the maximal signal charge for all pads.

2.2.4 Current measurement

For the I/V measurement two **Keithley 6485** pico-amperemeters were used, one for the pad current measurement and one for the guard current measurement. For reducing the noise level in the pad current, a constant measurement range was set, the slow integration range was chosen and a fast averaging filter was applied in the pico-amperemeter. All current measurements were taken in the range of $10 - 500 \text{ V}$ with 10 V steps.

When a reverse bias is applied on a semiconductor diode, a dark current is created. The dark or leakage current is the current flowing in the absence of external effects or energy, like particles or light that move charges to the conduction band. The source of this current is charges generated

at generation-recombination centers at the surface of the device and in the depleted volume [26].

The typical behavior of current to voltage (I/V) of a reversely biased Si sensor is as follows: for voltage below V_d , the current increases according to Eq. 2.3 [26] that describes the volume generation current per unit area, J_{vol} , as function of the intrinsic carrier concentration, n_i , and the carrier generation lifetime, τ_g ,

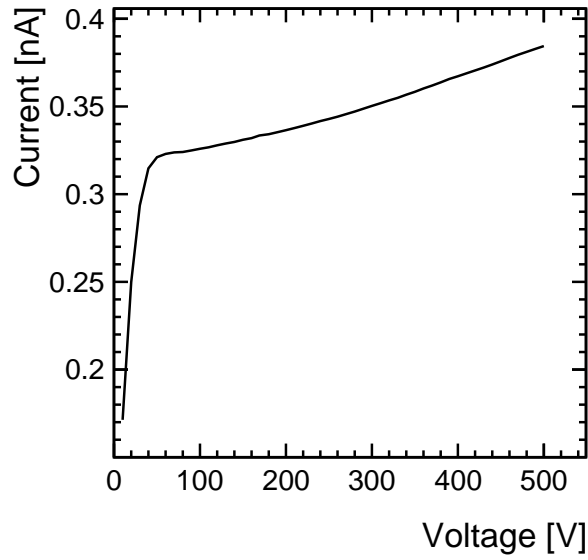
$$I_{\text{pad}} = AJ_{\text{vol}} \approx -eA \frac{n_i}{\tau_g} \sqrt{\frac{2\varepsilon_0\varepsilon_{\text{Si}}}{eN_d}} V. \quad (2.3)$$

When the space charge region fills up the entire sensor width (just before V_d), an additional surface contribution arises. After full depletion is reached the I/V curve displays a region in which the current increase is rather small. At very high voltage, electrical breakdown occurs. This can be identified by a substantial increase in current. An additional increase in voltage eventually destroys the sensor.

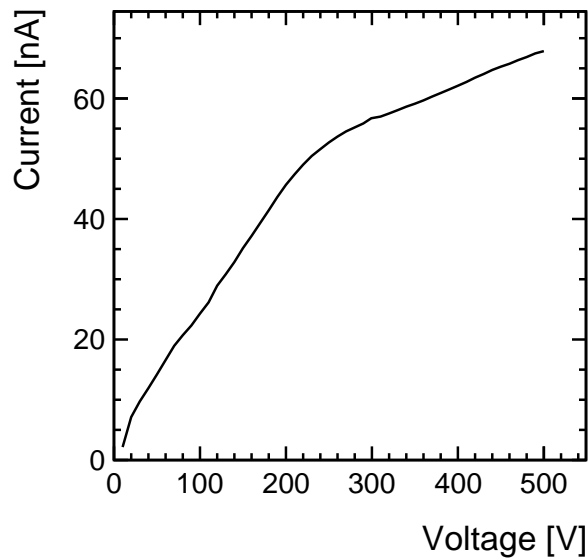
An example of an I/V measurement result is shown in Fig. 2.10a. The current measured from the guard ring is shown in Fig. 2.10b. As mentioned above, if any short-circuit or electrical breakdown occurs in the sensor, it may be detected by observing high current in the guard ring. For the LumiCal sensors, the manufacturing specification demands a guard current of less than 3000 nA for operation voltage of 200 V. In practice, measurements made by Hamamatsu obtained significantly lower values, in the range of 40 – 80 nA [23].

Leakage current measurements are a very powerful tool for sensor testing. Almost all possible problems in the sensor production process lead to a deviation of the I/V curve from the expected shape. Furthermore, the leakage current in operation mode must be less than 5 nA for proper signal generation. A higher current may cause electronics issues (e.g. due to power consumption and heating).

The leakage current expected in operation mode was estimated by averaging the current values obtained for $V > V_d$. Since determination of the depletion voltage from the I/V curve is not precise [26], the value obtained for V_d from the capacitance measurements was used.



(a)



(b)

Figure 2.10: Typical curves of an I/V (leakage current vs bias voltage) measurement result for a single LumiCal sensor pad: (a) Pad current as a function of voltage. (b) Guard current as a function of voltage.

2.2.4.1 Results

In Fig. 2.11, the leakage current is plotted against pad number for all four sectors. The results from all three sensors are plotted together for comparison.

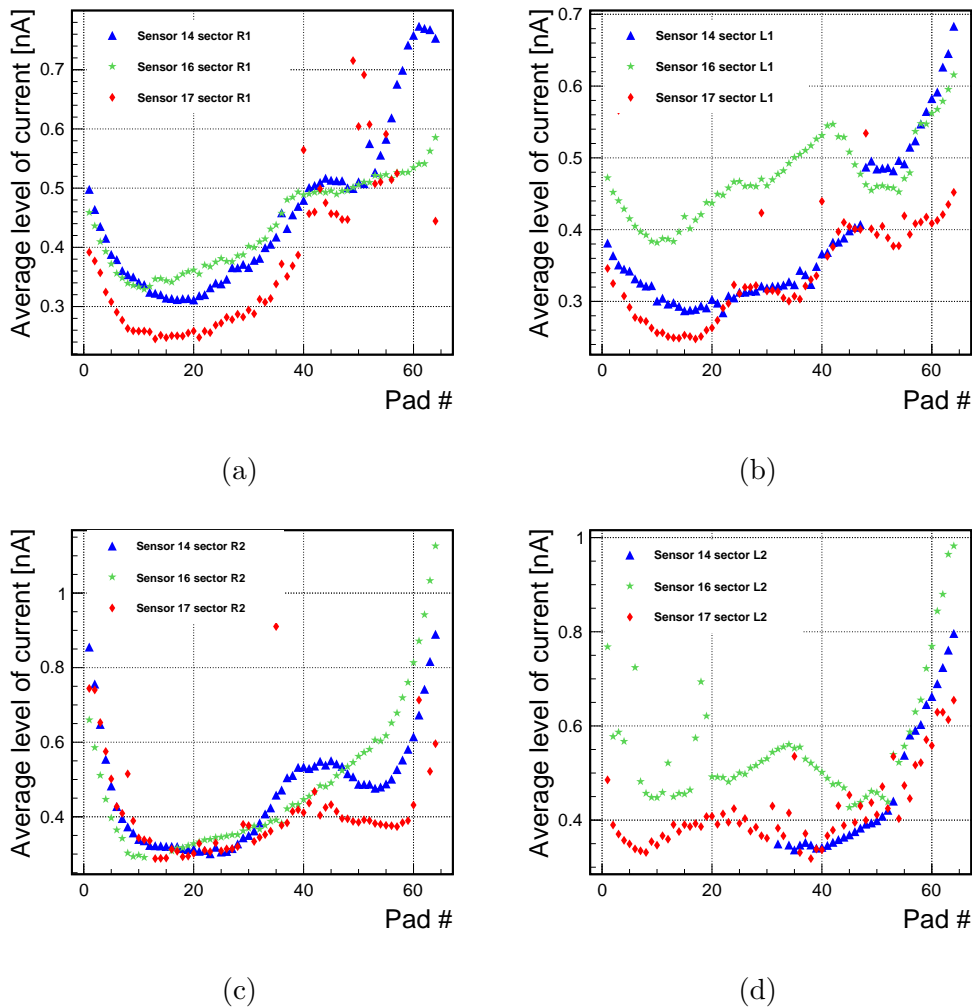


Figure 2.11: Dark current vs pad number in sectors R1, L1, R2 and L2 (see Fig. 2.1) on plots (a) - (d) respectively. The blue, green and red datasets correspond to sensors 14, 16 and 17, respectively.

Since the operation voltage was determined to be higher than 70 V, these results fairly represent the expected leakage current in operation mode. All

measured current levels are less than 1.2 nA, which is significantly less than the 5 nA threshold. This comes to suggest that for all of the measured pads, leakage current will not interfere with signal detection.

A similar trend can be viewed for some sectors in different sensors. Also seen is that the outer sectors, L2 & R2, generally display higher current levels than the inner sectors, L1 & R1 (see Fig. 2.1 for sector labeling). This is to be expected since the outer sectors are adjacent to the guards rings, suggesting that the electrical field for those pads is less uniform. Some points deviate from the trend, probably due to small imperfections on the sensor surface (tiny scratches, dust etc.) or as a result of noise during the measurement. Some points from sensor 14 are missing since it was broken before the of measurements were completed. Five points in sector R1 of sensor 17 were omitted due to a scratch in this area of the sensor which induces very high currents, which can be seen in Fig. A.2 in the Appendix.

2.3 Conclusion

Many improvements have been made to the Tel-Aviv silicon lab, first and foremost through the installation of a clean room. Three complete LumiCal sensors were studied in the silicon lab. Studies included measurements of dark current and capacitance as a function of applied voltage. All pads (with the exception of damaged areas) behave as expected. The dependence of capacitance on pad size was found to be linear, and a similar trend was observed among all sectors in all of the different sensors. Depletion voltage was determined for all measured pads and was found to lie in the range 35 – 70 V, suggesting that operation voltage for the sensors should be greater than 70 V.

For all pads, the leakage current expected in operation mode was found to be less than 1.2 nA, suggesting that it will not interfere with signal detection. The dependence of current on pad size was found to behave differently for each sector, but similarly among the sensors. The magnitude of the current was observed to be slightly higher in the outer sectors.

Chapter 3

Beam Test of LumiCal sensor prototype

The LumiCal sensors have been previously tested with a full electronic readout chain in a test beam by the FCAL collaboration. In 2010 and 2011 the FCAL collaboration performed three beam-tests. These were the first tests of the LumiCal silicon sensors prototypes equipped with a readout chain. In 2010, the readout chain was comprised of a board with two front-end Application-Specific Integrated Circuits (ASICs), which provided analog readout for 16 channels, and an external analog to digital unit (ADC). In 2011, the complete 32 channel readout module described in 3.3.3 was used. The aforementioned tests were performed on a single sensor plane and were carried out primarily to test the readout system. Results of the analysis show the feasibility of such a system and a clear signal obtained from the sensor. In order to simulate the development of an electromagnetic (EM) shower, different numbers of absorber plates were placed in front of the sensor during the tests [27, 28].

In October 2014, FCAL performed another beam test of the LumiCal sensors. In this beam test, for the first time, four LumiCal sensors with electronic boards and a full readout chain were tested together in a test beam. A dedicated mechanical structure, to be discussed in 3.3, was used in order to position the sensor planes and tungsten absorber plates together accurately. In each sensor plane, 32 pads were connected to the readout system. A tracking telescope composed of four silicon pixel detectors was also present as an auxiliary system. The primary purpose of this beam test was to use LumiCal to reconstruct the profile of the development of the EM shower caused by electrons passing through absorber planes.

In this chapter, a review of the test beam system is given.

3.1 The proton synchrotron test-beam facility at CERN

The LumiCal sensors were tested in a beam from the Proton Synchrotron (PS) accelerator, which is a key component in CERN's accelerator complex (depicted in Fig. 3.1). It is a circular accelerator with a circumference of 628 m. In the PS, protons are accelerated up to 25 GeV before moving on to the next acceleration stage - the SPS.

The PS is also utilized as a particle beam source for test beams. Protons of energy of 24 GeV are delivered to five different beam-lines referred to as T7, T8, T9, T10 and T11, enabling multiple experiments to run simultaneously [29]. Some beam lines receive the primary beam (protons) as is, while others receive a secondary beam created by directing the main beam onto a target, creating different particles via various interactions with the matter in the target. The beam energy can be selected from the range of 1 – 15 GeV, and its transverse profile can be tuned by controlling the various quadrupole magnets positioned along the beam-line. In addition, the use of Cherenkov detectors enables identification and selection of particle types.

The LumiCal beam test took place in the T9 beam-line, using secondary particles created from a target of 200 mm beryllium and 3 mm tungsten (electron enriched). The secondary beam is composed of hadrons, electrons and muons. In the test runs which are relevant for the analysis presented in this work, the beam was operating at 5 GeV.

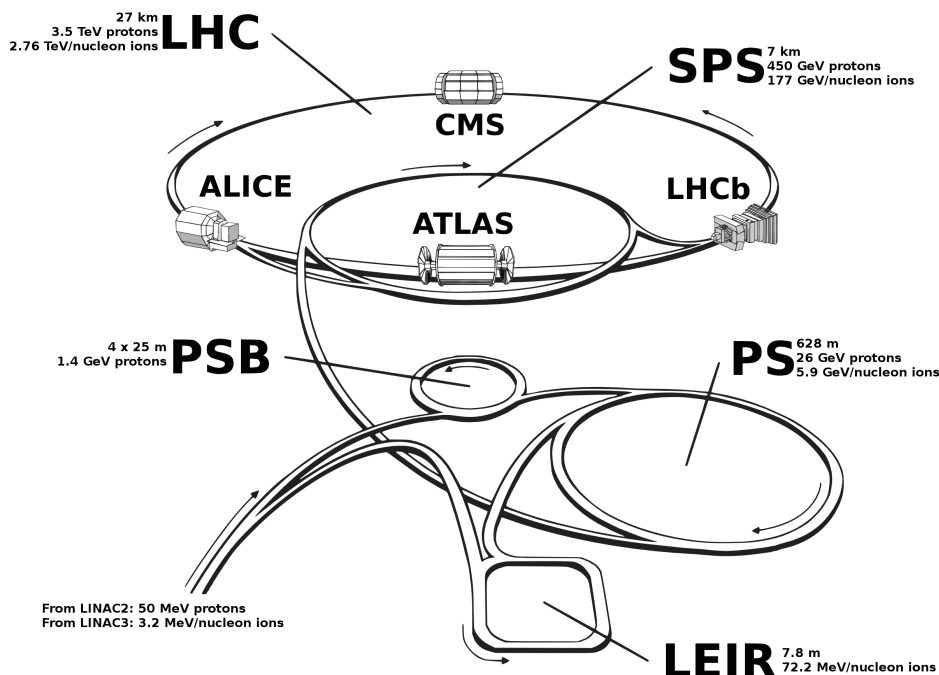


Figure 3.1: CERN's accelerator complex. The PS is one of the elements accelerating protons beams for LHC.

3.2 The telescope

As mentioned, the system set up by FCAL (to be described in Section 3.3) was accompanied by a tracking telescope. This system was set up and configured by our colleagues from Aarhus University. The telescope system comprises four **Mimosa 26** [30] silicon pixel detector planes linked with the FCAL trigger system. When a trigger was received, hits were read from the four Mimosa planes and the information was stored. The Mimosa 26 is read in 'frames'; the detector plane is continuously scanned row-by-row. When a trigger is received, information is stored from four consecutive scans of the entire plane. This means that for each trigger, data are stored from four frames, while the actual hit data are contained inside one (or sometimes two) of them. Upon reading, the frames containing the actual data were identified and the data were taken from them. The timing is monitored by a *frame number*, which is an internal clock for the telescope system that counts the number of frames. For the purpose of synchronization, the frame number of the first frame was stored alongside with the corresponding telescope data. The total readout time of the Mimosa plane is 200 μsec (50 μsec per frame).

As depicted in Fig. 3.2 the Mimosa planes were positioned up the beam-line from the LumiCal sensors, so as to form a track of a particle coming towards them. The distance between every two telescope planes was 20 cm, and the distance from the last plane to the first LumiCal sensor was 52 cm.

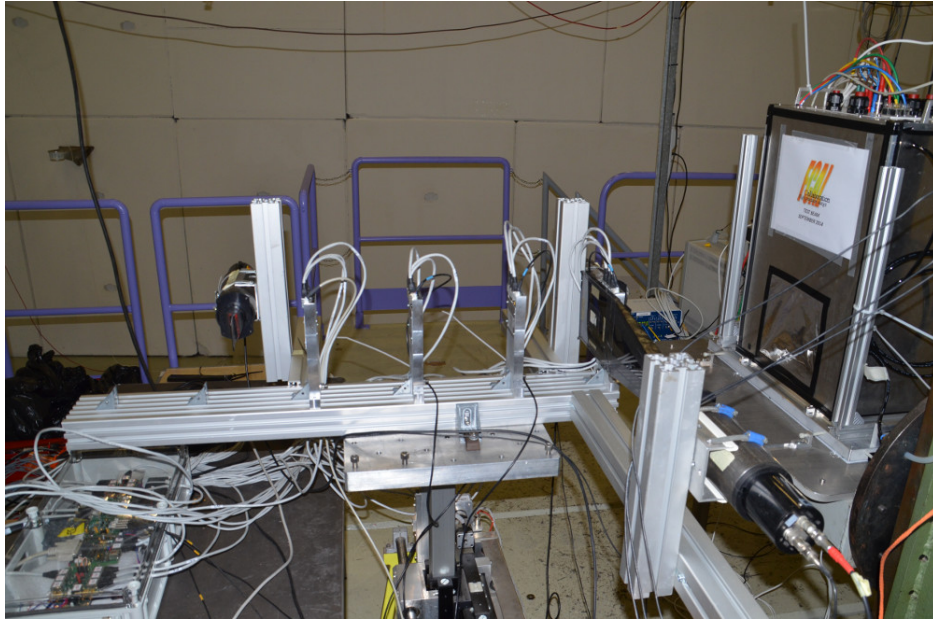


Figure 3.2: The four Mimosa planes used for the telescope (the rightmost one is surrounded by scintillators). The beam enters from the left side. On the right, the mechanical structure containing the LumiCal sensors can be seen.

3.3 Beam test setup

3.3.1 Physical layout

Since the main objective of this beam test was to demonstrate shower development, absorber plates were positioned between the sensor planes. Each plate was made of an alloy containing 93%–95% tungsten and was ~ 3.5 mm thick, which corresponds to about one radiation length [31].

In order to meet the demanding geometrical requirements of the LumiCal detector and to enable a very flexible configuration of active sensor layers together with tungsten absorbers, a very sophisticated mechanical structure

was designed and developed at CERN [32]. The overall view of the structure is presented in Fig. 3.3a. The most important component, the layers positioning structure, is presented in Fig. 3.3b. It includes three aluminum combs with 30 slots each which allow to install the tungsten absorber or active sensor layer with the required precision. The tungsten absorber plates are mounted in supporting frames, as shown in Fig. 3.4a. In order to assemble the sensor boards in the comb slot provided for the tungsten absorber, a supporting frame with identical outer dimensions was prepared as shown in Fig. 3.4b. This enables a flexible detector configuration and allows to easily change the detector prototype geometry.

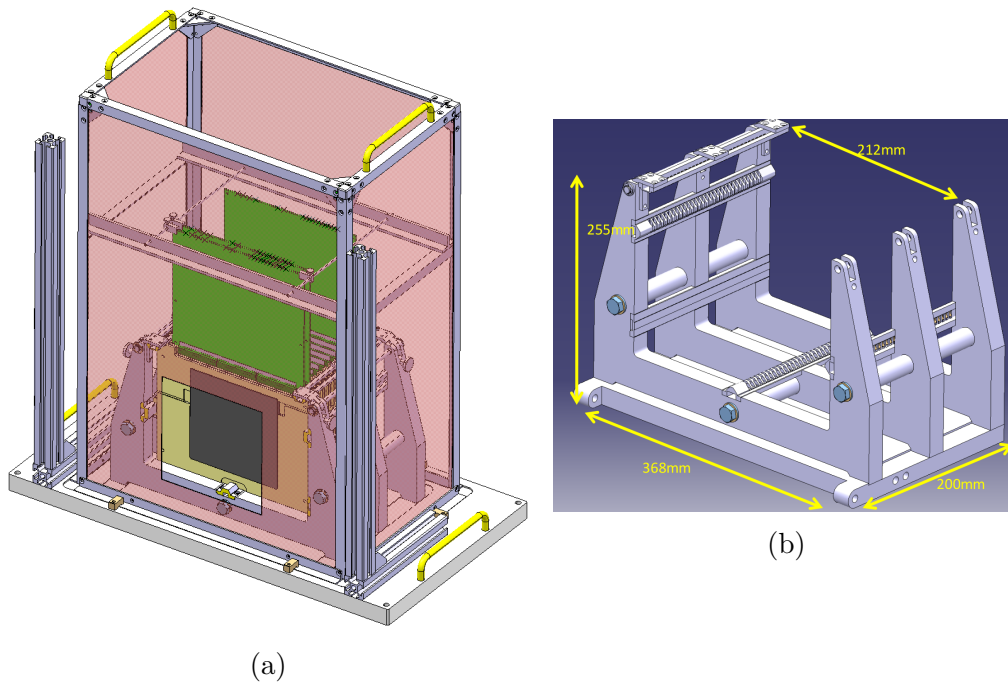


Figure 3.3: (a) Overview of the LumiCal prototype mechanical structure. (b) Design of the layers positioning structure.

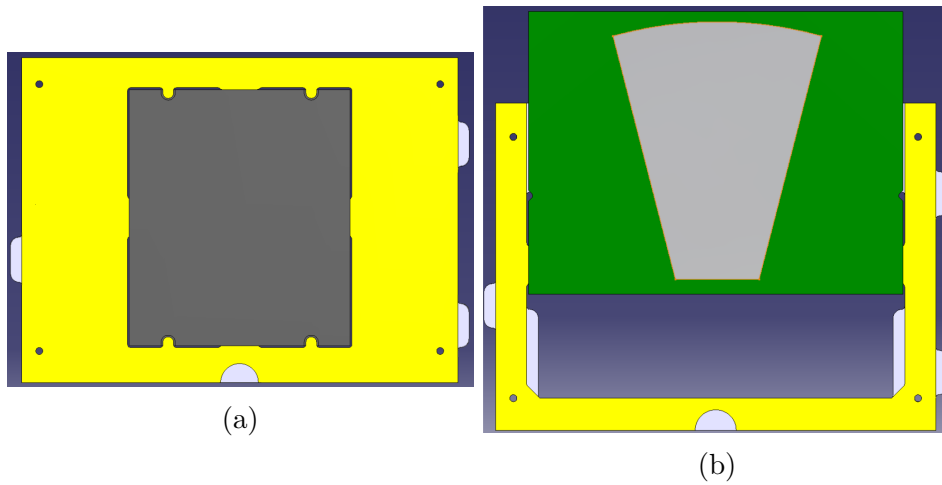


Figure 3.4: (a) Tungsten absorber (gray) in a supporting frame (yellow). (b) Sensor (gray) and board (green) partially retracted from a supporting frame (yellow).

The four LumiCal sensors, mounted on electronic boards connected to the readout chain, were placed inside this structure (as depicted in Fig. 3.5) which served also as a Faraday cage.

Two absorber plates were placed between every two sensor planes. Since the distance between each two sensor planes was 13.5 mm, ample space was available for the absorber plates. This remained unchanged for the entire duration of the beam test. However, during the test, three different configurations of absorber plates in front of the first sensor plane were used. As seen in Fig. 3.6 in the different configurations, one, three or four, absorber plates were positioned in the front.

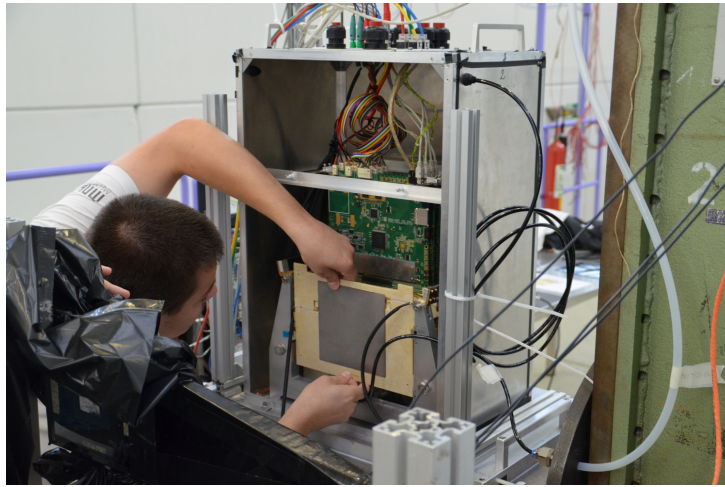


Figure 3.5: An absorber plate being assembled into the mechanical structure containing the LumiCal sensors (already in place). The readout boards can also be seen.

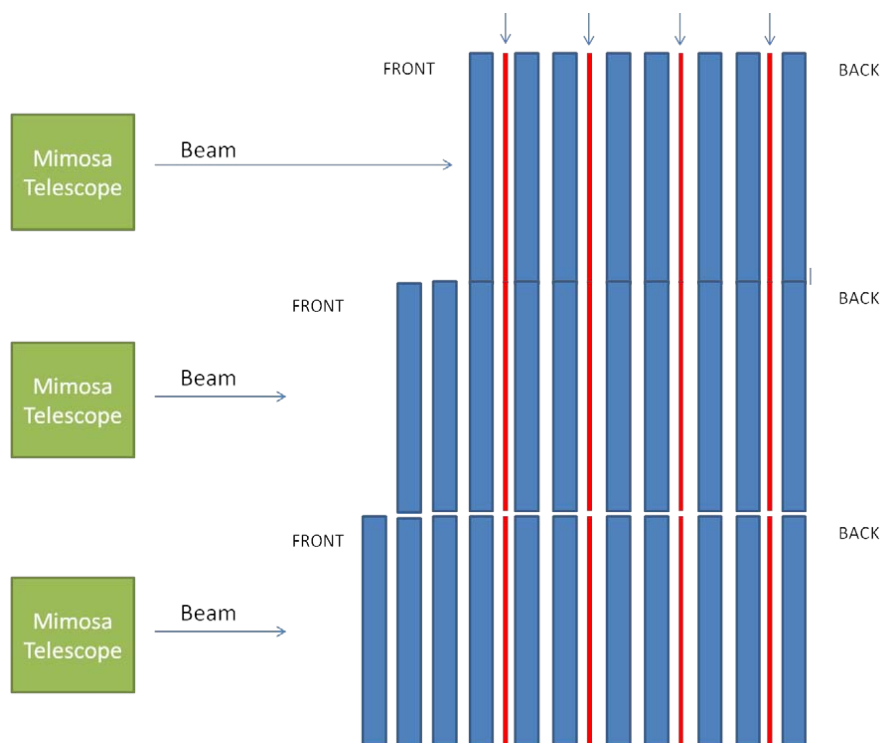


Figure 3.6: The different configurations (labeled 1-3 from top to bottom) used during the beam test. Distances are not to scale. The thin red lines represent the LumiCal sensors and the blue bars are the absorber plates.

3.3.2 Trigger system

Data taking was performed using a trigger. A trigger was fired upon verification that there was indeed a particle incoming from the beam line, and that it passed through the LumiCal planes in the area of the "active" pads (i.e. the pads that were connected to readout channels). This was accomplished using three scintillators (visible in Fig. 3.2): two scintillators were placed before the first and after the last telescope plane and a coincidence between them was required, establishing that a particle indeed entered and left the telescope area. A third scintillator, with a 9 mm-diameter circular hole in it, was positioned just before the third telescope plane, in front of the area of the active pads. Anticoincidence was required between this scintillator and the combination of the other two, thus verifying that the particle is likely to hit the LumiCal planes in a designated area (referred to as "the trigger area").

Another factor which was incorporated into the trigger signal is the particle type. As stated in Section 3.1, Cherenkov detectors were available in the test beam facility. Using these detectors, the beam particle components can be identified and passed to the trigger system. Two different runs of operation were used: hadron runs and $e + \mu$ runs. Since the study of this work was carried out on μ samples, all of the analysis described in the following sections was carried out on the latter.

3.3.3 Connections and data taking

The LumiCal readout module is comprised of a front-end ASIC, an ADC ASIC, and a field-programmable gate array (FPGA) based data concentrator. The front-end ASIC provides amplification and shaping for the analog signal obtained from the sensor. Two different gain values are available in order to accommodate two operation modes: calibration mode, in which low signals from minimum ionizing particles (MIPs) are collected and a physics mode, in which higher signals from energetic particles are collected. The ADC converts the signal to a digital form. The data concentrator collects the incoming data and stores it in event packets according to the incoming triggers. A block diagram of the readout chain is presented in Fig. 3.7.

No central DAQ unit existed for the system. Instead, both sub-systems (telescope and LumiCal sensors) had a DAQ computer in charge of control and data taking. Furthermore, each sub-system had its own internal clock. For this reason, coordination between the two sub-systems had to be carried

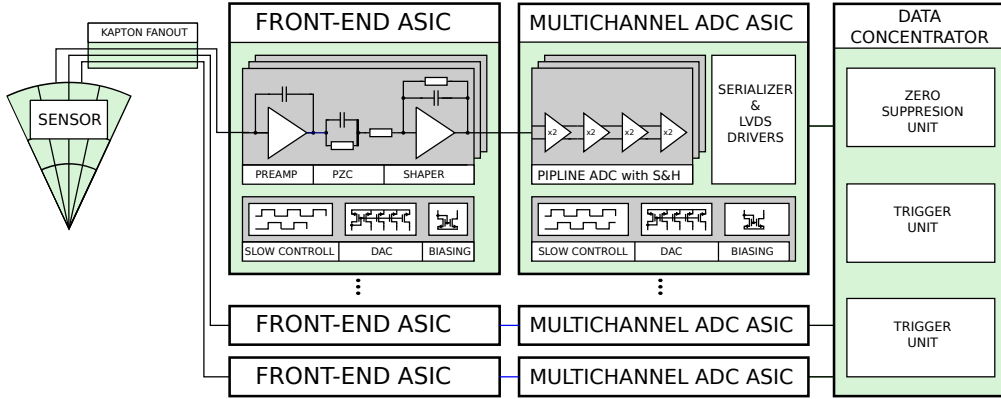


Figure 3.7: Block diagram of the LumiCal readout chain.

out. This was achieved using a trigger logic unit (TLU). The TLU receives the trigger signal and generates a *TLU number*, which is an integer number counting the number of triggers delivered. The TLU then passes on the trigger signal and the TLU number to other relevant units. The TLU number of each event packet was stored alongside with the digital information. In order to coordinate between the TLU number and the telescope frame number, a dedicated auxiliary unit (AUX) was used, saving the two numbers from the same event together. In this manner, matching between events stored in the LumiCal DAQ and the telescope DAQ could be made. Figure 3.8 displays the connections and the flow of information in the system.

In each of the sensor planes, the connected pads were pads 51-64 of sector L1 and 47-64 of sector R1 (see Fig. 2.1). Channel numbering was assigned as listed in Table 3.1. Upon the arrival of a trigger, the available 32 channels were recorded with 32 samplings. The sampling time was $T_{\text{smp}} = 50\text{ns}$, resulting in a total read time of $1.6\mu\text{s}$. Half of the channels were amplified with a different gain from the other half. For each trigger, the TLU number from the LumiCal DAQ, the TLU number from the AUX and the telescope frame number from the AUX were stored, for the purpose of synchronization between LumiCal and telescope data.

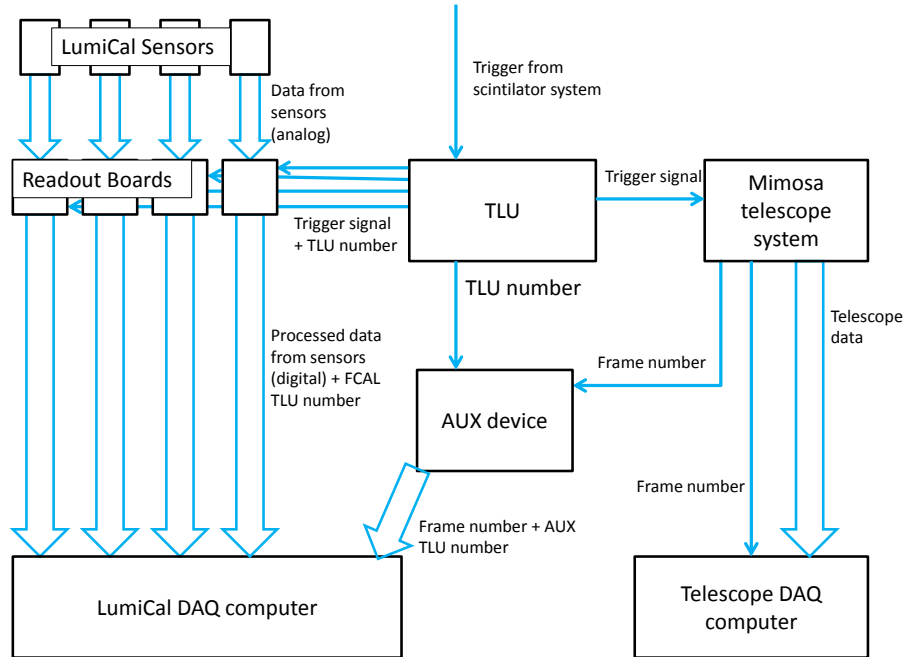


Figure 3.8: A schematic representation of the connections and the path of the signal in the system. Data is symbolized by a thick arrow, while simple bit information (e.g. the trigger signal) is symbolized by a thin arrow.

Channel number	Sector and pad number	Channel number	Sector and pad number
0	L1-51	16	R1-62
1	L1-52	17	R1-61
2	L1-53	18	R1-60
3	L1-54	19	R1-59
4	L1-55	20	R1-58
5	L1-56	21	R1-57
6	L1-57	22	R1-56
7	L1-58	23	R1-55
8	L1-59	24	R1-54
9	L1-60	25	R1-53
10	L1-61	26	R1-52
11	L1-62	27	R1-51
12	L1-63	28	R1-50
13	L1-64	29	R1-49
14	R1-64	30	R1-48
15	R1-63	31	R1-47

Table 3.1: The numbering of the output channels in the readout system.

Chapter 4

Analysis results of data from LumiCal beam test

In this chapter, analysis results of the data from the beam test described in [chapter 3](#) are presented. The goal of the analysis was to test the uniformity of response of the four sensors that were tested in a muon beam.

4.1 Tracking information from telescope

4.1.1 Signal processing

The hit information was stored digitally for each pixel, with no information on the signal strength, in the Mimosa plane. In order to extract tracks from it, several analysis steps must be performed:

1. clusters of pixels that represent hits must be built;
2. relative alignment of the different planes has to be carried out;
3. track parameters need to be determined.

Reading the data and forming clusters was executed using the Telescope A Pixel Analysis Framework (TAF [\[33\]](#)), designed especially for analysis of telescope data. The framework is also designed to perform alignment and track finding, however these stages were carried out using software supplied by Aarhus University. The limitations of this software are as follows [\[34\]](#):

- only two of the telescope planes were aligned;
- tracks were formed only from events with hits in all four planes.

Another limitation of the tracking procedure comes from the fact that the Mimosa readout time is much longer than that of the LumiCal and is also long compared with the beam rate. For this reason, there may be more than one track reconstructed in the telescope for a single event recorded in the LumiCal system (a single trigger), without any way to determine which is the correct track.

4.1.2 Results

Once tracks have been formed, track parameters can be used to propagate the expected hit position to the LumiCal planes. Figure 4.1 presents an example scatter plot of all the hits which were associated with tracks in the four telescope planes, and the expected hit positions in the first LumiCal plane, in the plane transverse to the beam direction z .

Observing these hitmaps one may conclude that

- the trigger area is well observed in all four planes, growing sharper with proximity to the last telescope plane. This is consistent with the hole scintillator being in very close proximity to the last plane;
- in spite of the above, many hits that were associated with tracks are found outside of the trigger area. This can point to either bad tracking or to track building from hits belonging to incorrect tracks.

This picture changes slightly for the better if only events with one recorded track are considered. In an effort to explain the second aforementioned point, it is interesting to look at the distribution of track multiplicity presented in Fig. 4.2. In most cases there is indeed only one track corresponding to one LumiCal event. As expected, there are events in which two tracks or more are reconstructed. The disturbing fact is that there is also a relatively large number of events for which no tracks were found. This suggests inefficiency in the tracking algorithm (since there can be no trigger without a track), which is probably a result of the software limitations mentioned above.

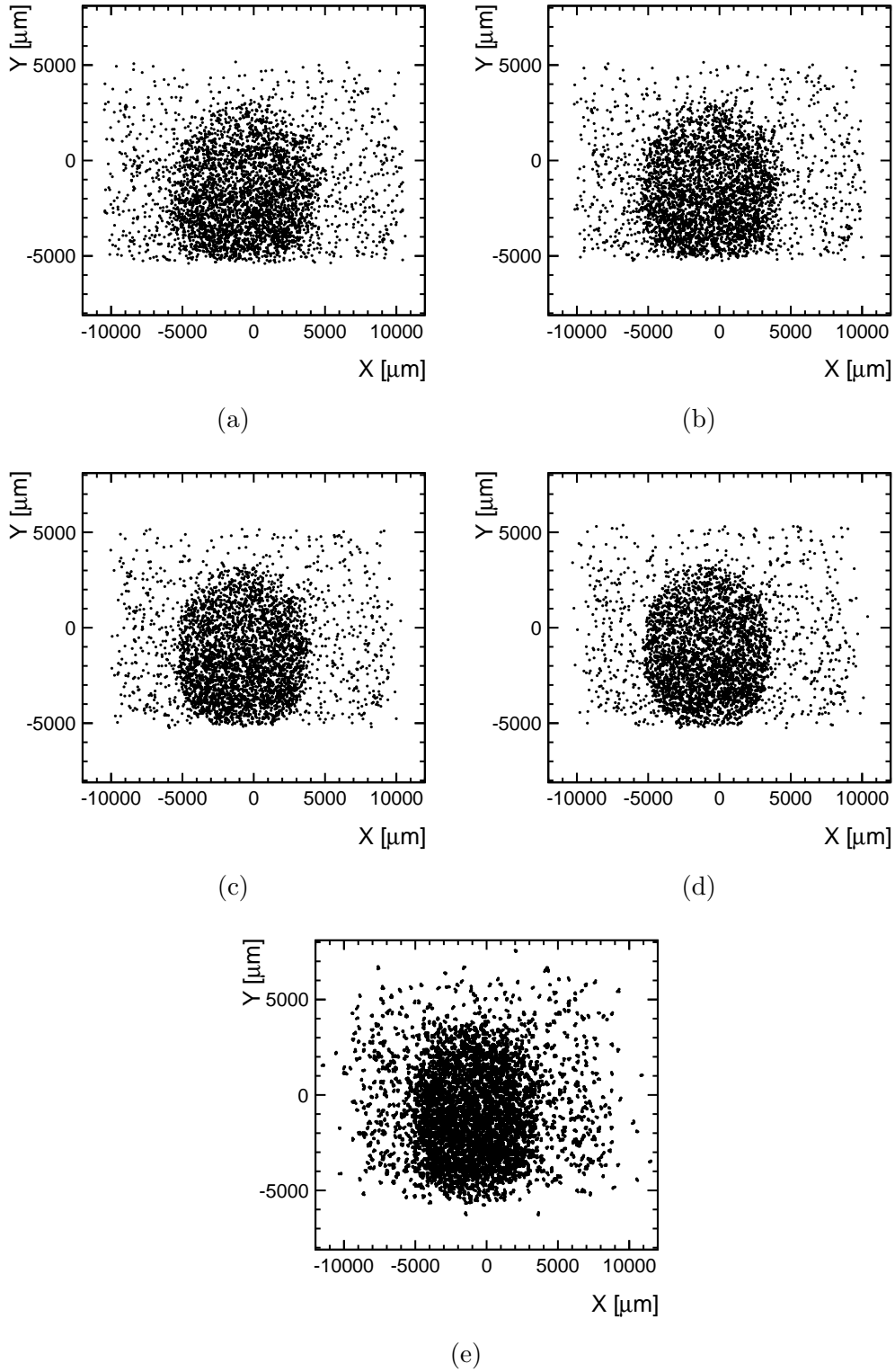


Figure 4.1: Hitmaps of hits associated with tracks for selected e/μ runs. Plots (a) - (d) correspond to telescope planes 1-4 respectively, and (e) displays the expected hit position in the first LumiCal plane. The trigger area can be clearly seen, as well as hits outside it.

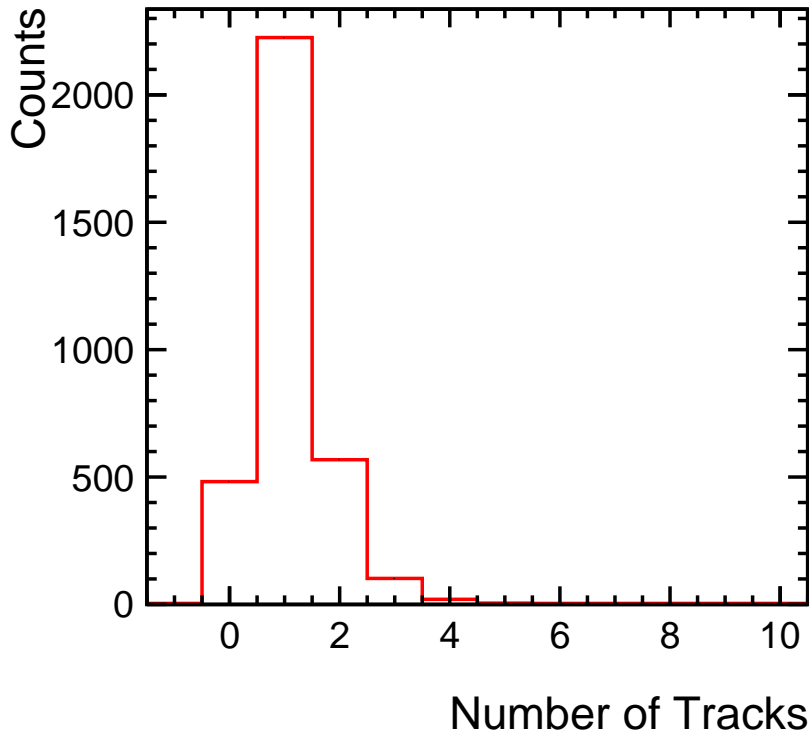


Figure 4.2: The number of tracks found per event for the same data set as in Fig. 4.1.

As mentioned above, due to system limitations the reconstruction of an incorrect track was not improbable. This fact may explain the deviant points in Fig. 4.1. Another possible explanation for the points outside of the trigger area could be inefficiency of the hole scintillator. Particles that hit this scintillator without producing a signal above threshold were not recorded and therefore the condition for anticoincidence was met, even though these particles did not pass in the designated area.

Determining the accuracy or resolution of the tracking process was done using distributions of residuals. Residuals are the distance between an actual hit position to the expected hit position in the same plane according to the calculated track parameters. Representative residuals plots for the four planes can be seen in Fig. 4.3. The Gaussian-like shape of the distributions, along with the fact that they are centered around zero and the similarity between the vertical and horizontal directions suggest that there are no major problems in alignment. From this, a resolution of $\approx 10 \mu\text{m}$ can be inferred for all planes and for both x and y directions.

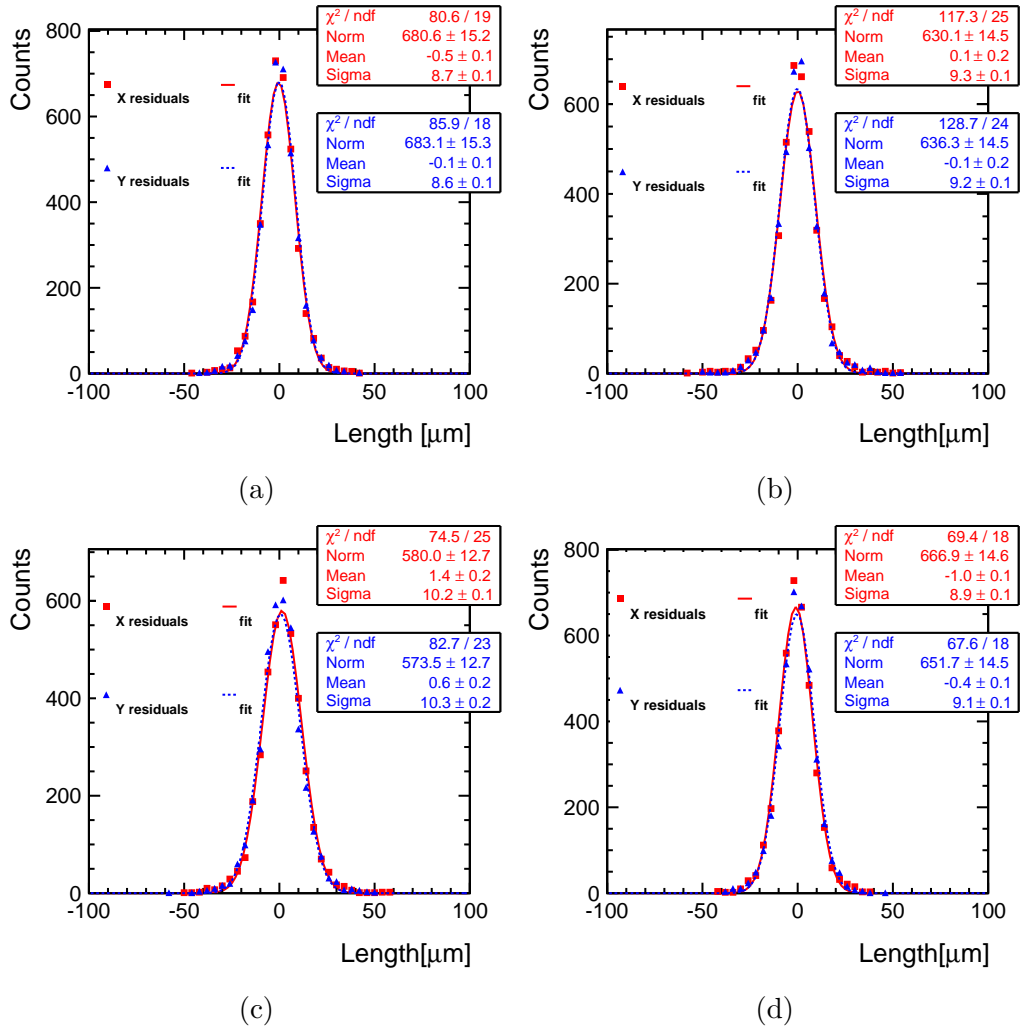


Figure 4.3: Residuals plots for the same data set as in Fig. 4.1. Plots (a) - (d) correspond to telescope planes 1-4, respectively. The square (triangle) markers and the solid (dashed) line represent the distribution and a fit to a Gaussian function, respectively, for the horizontal (vertical) direction.

4.1.3 Track selection

In an attempt to further improve the quality of tracks used for the analysis, the distribution of χ^2 value for the different tracks was considered. For each track, χ^2 was defined as

$$\chi^2 = \sum_{i=1}^4 \left(\frac{(x_i - x_i^p)^2}{\sigma_x^2} + \frac{(y_i - y_i^p)^2}{\sigma_y^2} \right), \quad (4.1)$$

where i sums over the four Mimosa planes. The coordinates (x_i, y_i) are the measured hit positions which were associated with the track, while (x_i^p, y_i^p) are the projected hit positions from the track parameters for the same plane. The variables $\sigma_{x/y}$ are the tracking resolutions in the horizontal and vertical directions respectively, $\sigma_x = \sigma_y = 10 \mu\text{m}$.

The function of a straight line in 3D space has six parameters. In our case, the constraints on the track direction to be not parallel to the x or y directions leaves four independent parameters in the function. Since the χ^2 is calculated using four (x_i, y_i) pairs, there are in total eight independent measurements that go into the calculation. Thus, the number of degrees of freedom (NDF) for this χ^2 calculation is $8 - 4 = 4$.

Figure 4.4a displays the distribution of χ^2 values for all muon candidate events (selected as detailed below in Section 4.2.2) in configuration 1. This distribution peaks at $\chi^2 \approx 2$, as is expected from such a distribution with $\text{NDF} = 4$, displayed in Fig 4.4b.

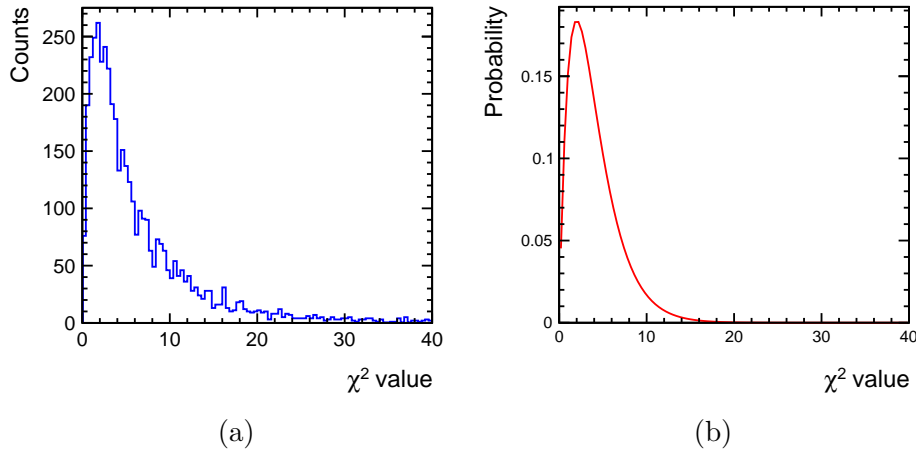


Figure 4.4: (a) The distribution of track χ^2 for all muon events in configuration 1. (b) A theoretical χ^2 distribution for $\text{NDF}=4$.

In order to disregard anomalous tracks, $P(\chi^2)$, the χ^2 probability distribution, was considered (i.e. the probability to get a certain χ^2 value or higher, given a certain NDF). This distribution (displayed in Fig. 4.5) is expected to be uniform when originating from a "true" χ^2 distribution. A deviation from a uniform distribution is observed near $P(\chi^2) = 0$ in Fig. 4.5, indicating badly reconstructed tracks with very large χ^2 values. In order to further investigate this curve, the distribution was plotted again with finer binning and a zoom-in of the area near $P(\chi^2) = 0$ is presented in Fig. 4.6. As expected for outliers, a dominant peak is observed at very low probability values. Only events with tracks with $P(\chi^2) > 0.0005$ were selected for further analysis.

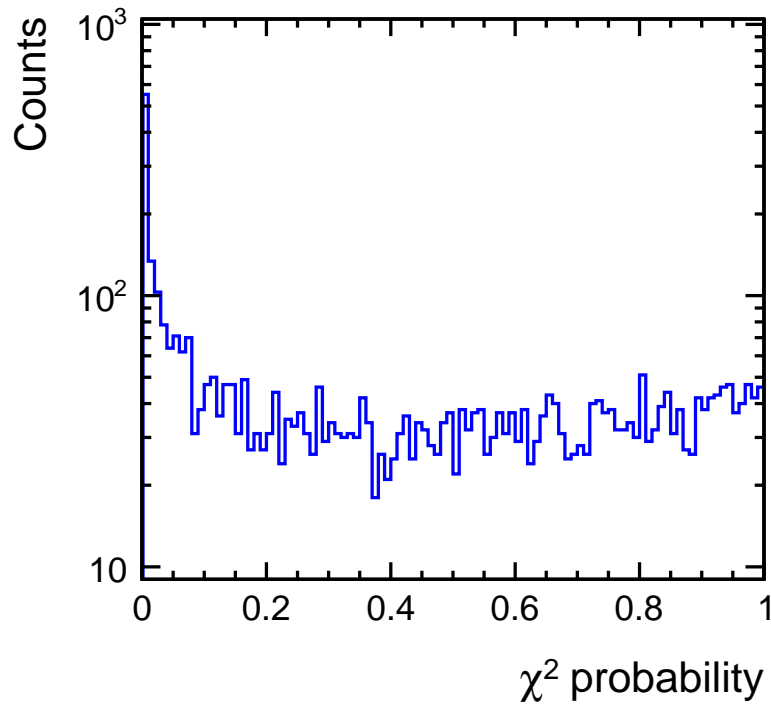


Figure 4.5: The tracks χ^2 probability distribution for all muon events in configuration 1.

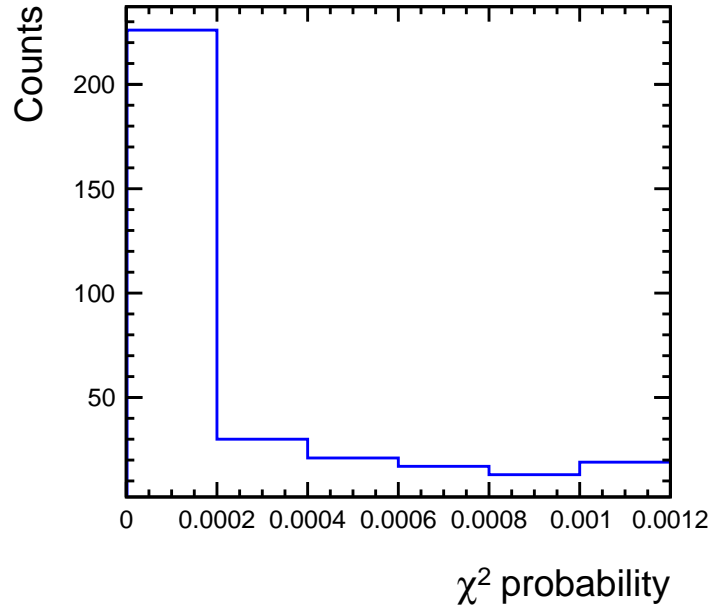


Figure 4.6: The distribution from Fig. 4.5, with an increased number of bins and zoomed near probability 0.

To conclude, fair tracking has been achieved using the data from the telescope. Avoiding the problem of not knowing which track is the right track was partially achieved by considering only single track events. Furthermore, track selection with the help of the χ^2 probability distributions was used in order to eliminate anomalous tracks.

4.2 LumiCal data analysis

4.2.1 Signal processing

When reviewing the data collected from the LumiCal readout channels, one does not directly receive the physical signal. Because of the electronic system and the sampling method used, the data must be processed in order to obtain the true signal amplitude. System parameters that must be taken into consideration in this procedure are the sampling time, T_{smp} , and the shaper's shaping time constant, τ .

An example of the raw data collected directly from the sensors is presented

in Fig. 4.7. First and foremost, since half of the channels had a different gain from the other half, their signal amplitude needed to be corrected. The gains were determined with dedicated capacitance tests [35]. Using the determined gain values, the amplitudes of half of the channels were corrected. Since the units were arbitrary at this point, the absolute number had no meaning. It was only important to make sure that the amplitudes from the different channels are comparable.

The type of multi-channel readout electronics which was custom-designed for the silicon sensor is known to generate correlated or common mode noise (CMN). This can be seen in Fig. 4.7, where the 32 samples of an event in the 32 read-out channels tend to oscillate in a coherent manner, around their individual base-line (BL). Prior to addressing this problem, the BL for each channel was calculated as an average of the samples 1 – 15 and 25 – 32 which did not contain a signal,

$$s_{\text{BL}} = \frac{\sum_{i=1}^{N_s} s_i}{N_s}, \quad (4.2)$$

where s_i are the relevant samples and N_s is the number of samples (22 in this case). Subtracting the BL from the data sets it to 0.

The signal arrival time with respect to the time of the trigger is constant up to one sampling interval. Furthermore, the duration of the signal (5 – 6 time samples) depends mostly on the sampling time and the shaping time and only slightly on the signal's amplitude. The above suggests that the same samples can be used for the calculation of the BL for all events in all channels. Since the CMN is characteristic of the specific chip used for the readout, it must be calculated individually for each chip. In our case, each board had four chips (i.e. eight channels per chip). The calculation of the CMN is a sample-by-sample average of the signal from channels connected to a certain chip, using only empty channels. For the i 'th sample, the CMN quantity v_i^{CMN} is defined as

$$v_i^{\text{CMN}} = \frac{1}{N_C} \sum_{j=1}^N (s_{ij} - s_{\text{BL}}), \quad (4.3)$$

where j is an index running over all the relevant channels in the chip, s_{ij} is the i 'th sample in the j 'th channel and N_C is the number of channels.

An example of the CMN for a single event is shown in Fig. 4.8. After calculating the CMN, it is removed from the sample by subtracting it from each channel for the appropriate chip.

As shown in Fig. 4.9, the result is a much cleaner sample-set, showing only the signal with a base-line of 0.

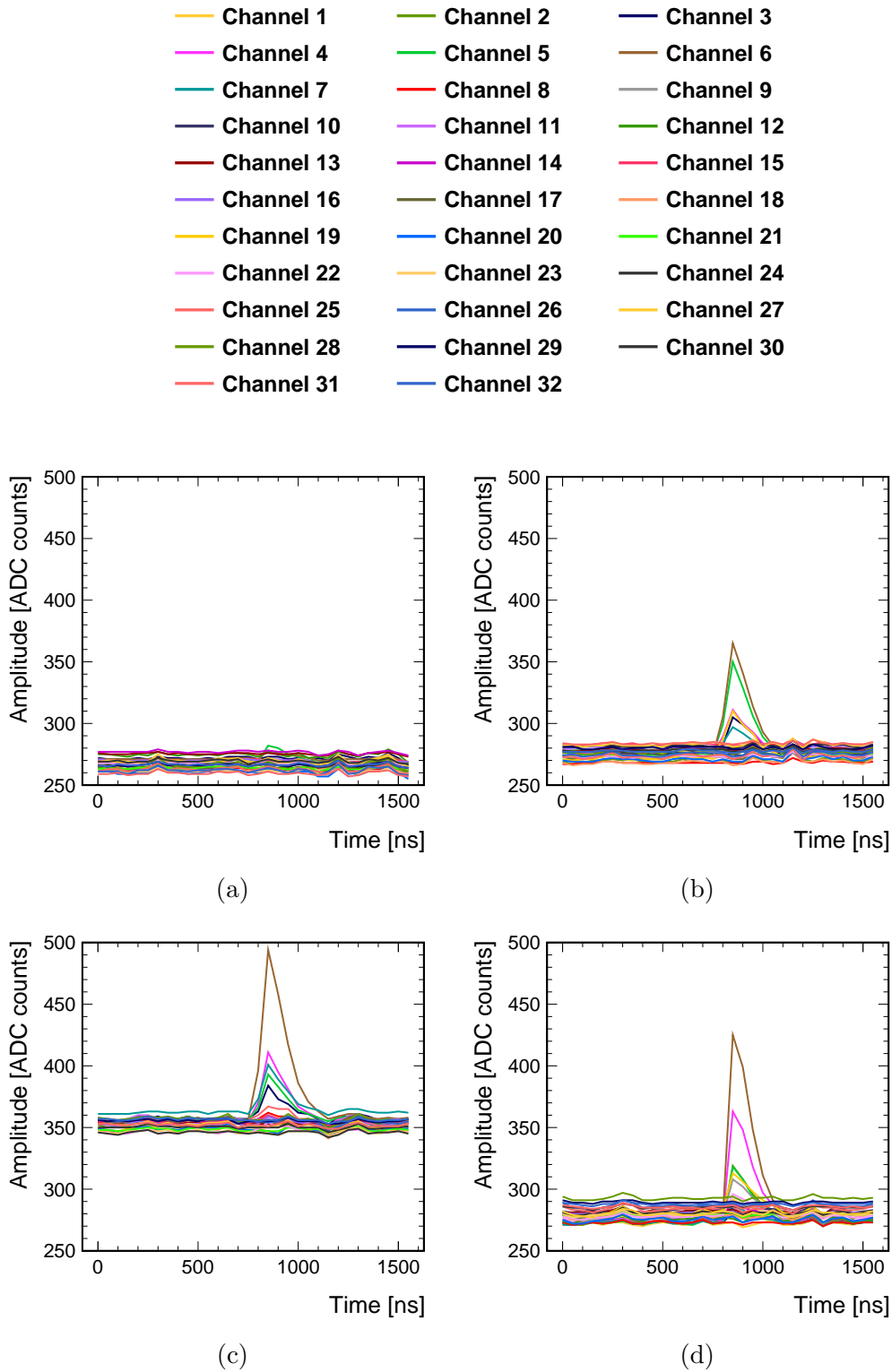


Figure 4.7: An example of a single event record in LumiCal (expressed as signal amplitude for each time sample). Plots (a) - (d) represent planes 1-4, respectively. Each readout channel is represented by a single line (see legend).

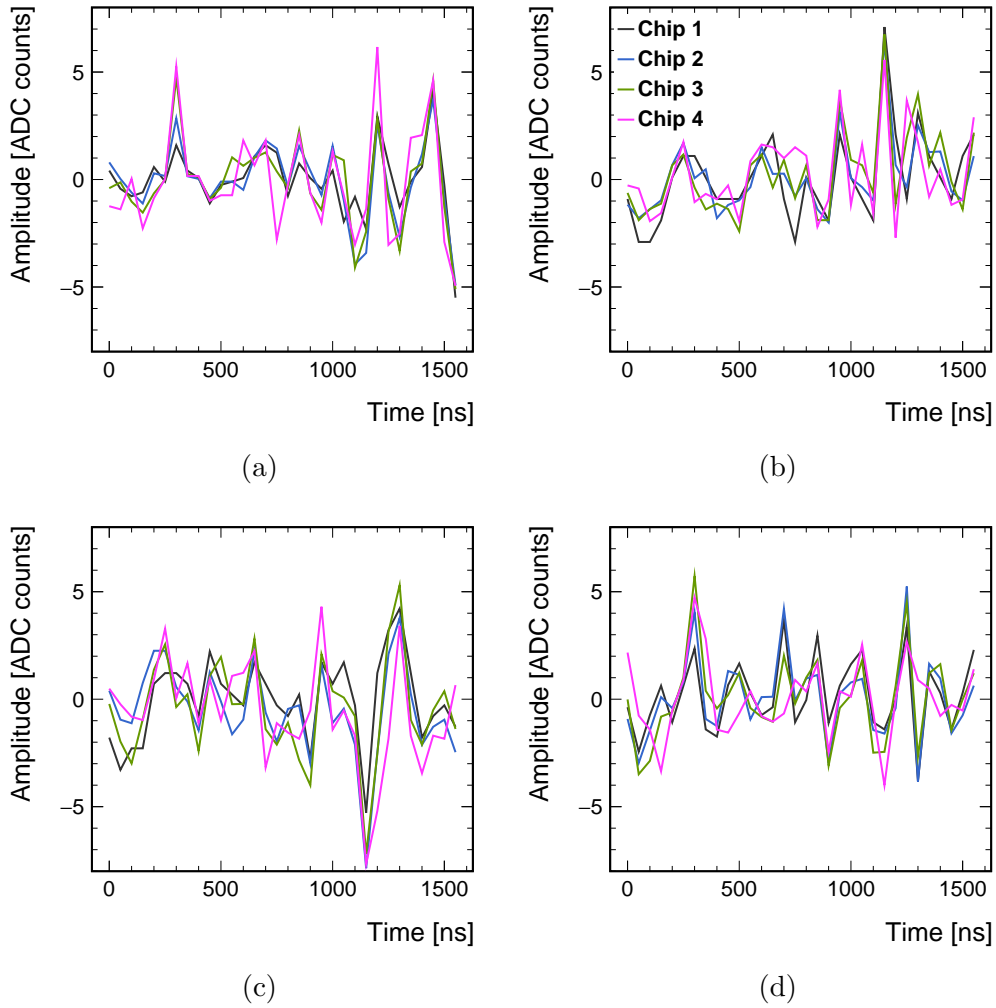
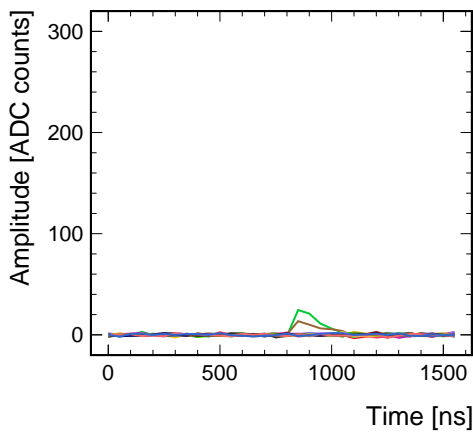
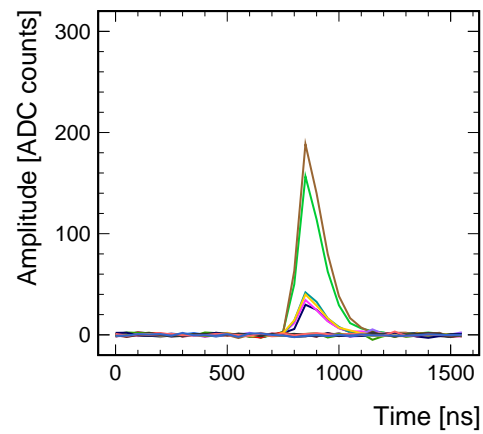


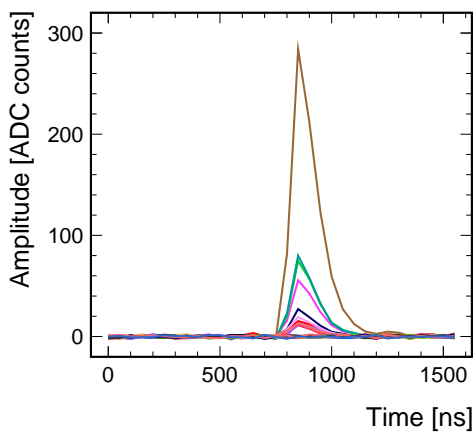
Figure 4.8: The calculated common mode noise (expressed as signal amplitude for each time sample) for the event in Fig. 4.7. Plots (a) - (d) represent planes 1-4, respectively. The common mode noise from each chip is represented by a single line (see legend).



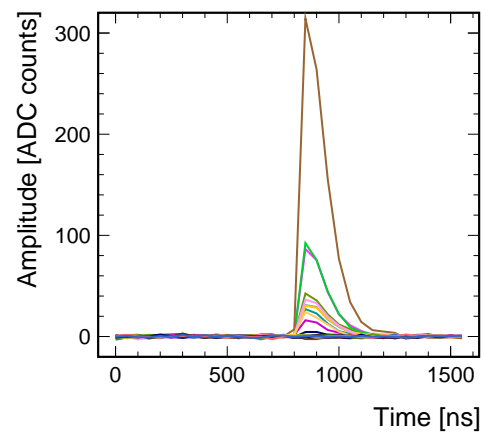
(a)



(b)



(c)



(d)

Figure 4.9: The data from the event in Fig. 4.7 after removal of the base-line and subtraction of the common mode noise. Plots (a) - (d) represent planes 1-4, respectively.

At this point the sample-set represents the incoming signal after shaping. In order to reverse the shaping process and reconstruct the original signal, a deconvolution method was utilized. The motivation for this can be found in [36], and the success of usage of this method for this readout system is described in [37]. Each sample was calculated using a weighted sum of three successive samples s'_k , s'_{k-1} and s'_{k-2} ,

$$a_k = w_1 * s'_k + w_2 * s'_{k-1} + w_3 * s'_{k-2}, \quad (4.4)$$

where $s'_k = s_k - s_{\text{BL}} - v_k^{\text{CMN}}$ is a BL and CMN removed sample and the weights are

$$w_1 = \frac{e^{x-1}}{x}, \quad w_2 = -\frac{2e^{-1}}{x}, \quad w_3 = \frac{e^{-(x+1)}}{x}, \quad (4.5)$$

where each of the weights depends on the sampling time T_{smp} and the shaping time constant τ , and x is their ratio,

$$x = \frac{T_{\text{smp}}}{\tau}. \quad (4.6)$$

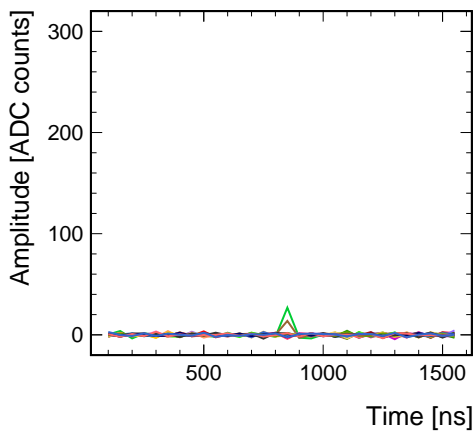
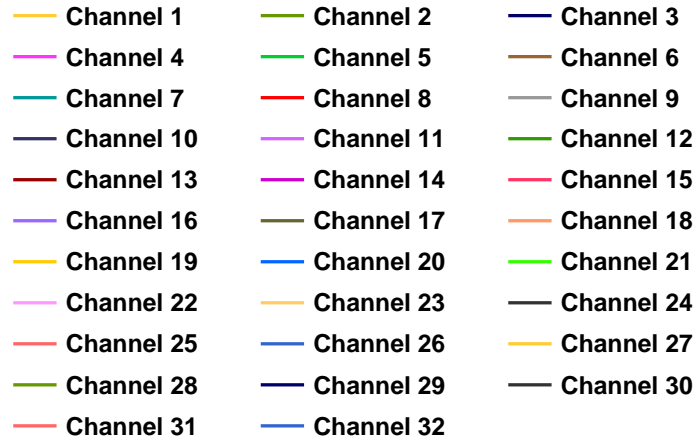
For our system $T_{\text{smp}} = 50$ ns as mentioned, and $\tau \approx 70$ ns (as reported from analysis of electronics performed by our colleagues in Krakow) so $x \approx \frac{5}{7}$. Following this, the obtained values for w_1, w_2 are ~ 1 whereas $w_3 \sim 0.1$.

The resulting sample set after deconvolution is shown in Fig. 4.10. Since the second weight w_2 is negative, a negative deconvoluted value is obtained for the first sample immediately after the samples with high amplitude.

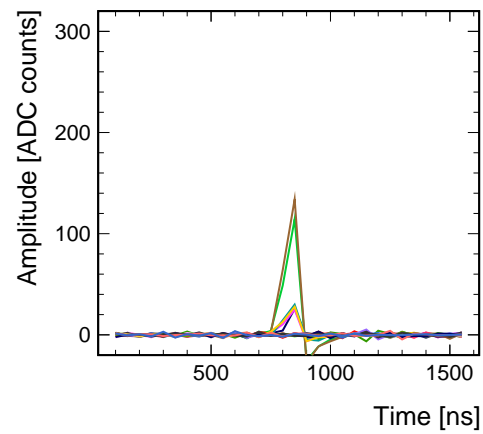
In a perfectly synchronized system, deconvoluting the samples (after removal of BL and CMN) should produce the final signal in its true digital form. However, in our system the ADC readout sampling was asynchronous, meaning that the sensor signals are digitized with an ADC clock independent of the beam clock. This can result in "smearing" of the signal over several time samples. The trigger arrival time for this system was in the proximity of the 17th sample of the 32 time-samples. For this reason, after applying the deconvolution, three cases can be observed,

1. the signal was received in the samples 16,17;
2. the signal was received in the samples 17,18;
3. the signal was received in sample 17 only.

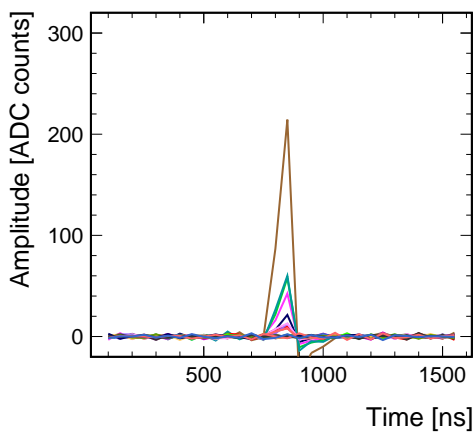
This is also portrayed in Fig. 4.11.



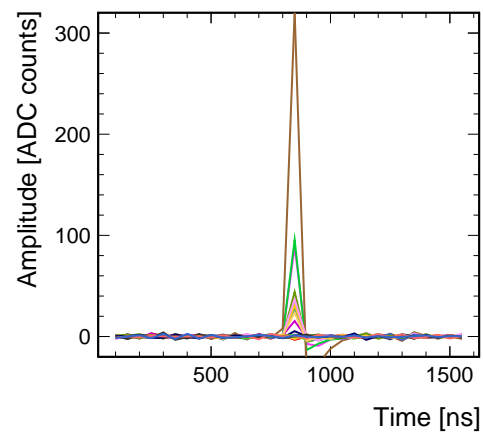
(a)



(b)



(c)



(d)

Figure 4.10: The data from the event in Fig. 4.9 after employment of the deconvolution method. Plots (a) - (d) represent planes 1-4, respectively.

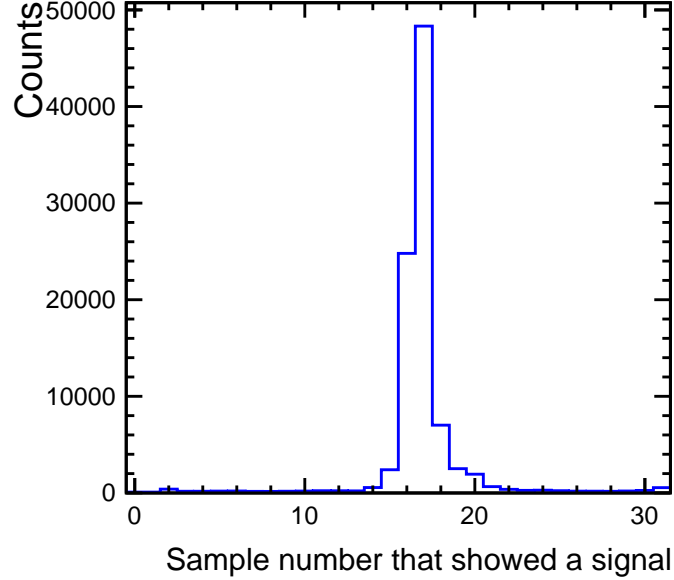


Figure 4.11: The sample number after deconvolution that showed a signal (amplitude three times higher than noise) for all channels in all events in configuration 3.

For the last case, it is obvious that the measured amplitude is simply the amplitude of the lone sample that had passed the noise threshold. For the cases in which two samples had a signal, the amplitude was reconstructed as (based on [38]):

$$A = (a_1 + a_2) \frac{\tau e^{-\frac{T_{\text{smp}}(t-1)+\tau}{\tau}}}{T_{\text{smp}}(1 - t(1 - e^{-\frac{T_{\text{smp}}}{\tau}}))}, \quad (4.7)$$

where A is the amplitude in ADC counts, a_1 and a_2 are the amplitudes of first and second deconvoluted samples used for the calculation, respectively, and t is the trigger arrival-time (in units of sampling time), given by

$$t = \frac{\frac{a_2}{a_1}}{\frac{a_2}{a_1} + e^{-\frac{T_{\text{smp}}}{\tau}}}. \quad (4.8)$$

Upon preliminary review of the collected data, it was discovered that in configuration 3 no signal was collected from the last LumiCal plane. This is most likely due to some damage to the FPGA connection on its readout board that occurred during the insertion of the last absorber plane.

4.2.2 Muon selection

The study described in the following sections was performed only on muon events, since 5 GeV muons are MIPs for the absorber planes and the LumiCal sensor. This means that the mean rate of energy loss through matter is close to the minimum. Since the Bethe-Bloch function, which describes the energy dependence of energy loss in matter, is rather flat around its minimum [26], the energy loss of MIPs is only weakly dependent on momentum. Therefore, a fairly constant detector-response is expected for MIPs and they can be used for calibration.

Furthermore, since muons are not very likely to interact with the absorber plates, no shower will develop as they pass through the experimental setup and one can expect a similar behavior in all four sensor planes. This makes muon events good candidates for uniformity studies and for inter calibration.

As mentioned in 3.3.2, the runs used for this work contained events from electrons and muons. Since the information from the Cherenkov detectors was not available on an event-by-event basis, there was no way to know if a specific event was a μ event or an e event. For this reason, a procedure for discriminating between μ and e events using the available information had to be developed. This was achieved using topological cuts based on the number of hits in the FCAL system. For a certain event in each sensor the number of hits N was defined as the number of channels which passed the noise threshold (i.e. sample 17 had a signal which was at least three times higher than the noise). For each event the center-of-gravity (COG) of the number of hits was defined as

$$Z_{\text{COG}} = \frac{\sum_{i=1}^4 N_i Z_i}{N_{\text{tot}}}, \quad (4.9)$$

where Z_{COG} is the COG coordinate along the beam-line, N_i is the number of hits for the i 'th plane ($N_{\text{tot}} = \sum_{i=1}^4 N_i$) and Z_i is the location of the i 'th plane along the beam-line.

Since muons do not generate showers, one does not expect the number of hits per plane to be more than 4 (in the extreme case that the charge from a single hit is shared among four adjacent pads. This can happen if a muon hits the sensor very close to the intersection of four pads). This means that the total number of hits in all planes must be no more than 16 (and

typically much less). Electrons that create showers, on the other hand, will leave more hits in the sensors. Furthermore, due to the constant number of hits per sensor, the COG for muon events is expected to be roughly the geometrical center of the system (between the second and the third sensor plane). For showers, the COG can vary according to the number of hits in each plane and can be either further up or further down the beam-line with respect to the geometrical center (depending on the shower profile and the specific configuration of absorber planes in question).

The result of the above is that electron and muon events will be located in different regions of the $Z_{\text{COG}}/N_{\text{tot}}$ plane, making it possible to select the muon events according to these parameters [39].

Note that in configuration 3, due to the absence of data from the last plane, all the above still applies with modifications: no more than 12 total hits are expected and the COG is in the position of the second plane.

Figure 4.12 displays a scatter plot of $Z_{\text{COG}}/N_{\text{tot}}$ for all events in configuration 1. The muon events are concentrated in the low N_{tot} values and around Z_{COG} values which correspond to the geometrical center of the system ($Z = 0$ is the location of the first LumiCal sensor plane), whereas a cluster of shower events can be observed in the region of high N_{tot} values and a Z_{COG} which is higher than the geometrical center. Some events also appear in low N_{tot} values, far from the geometrical center. These outlying events do not precisely fit the criterion of either muons or showers, and can be a result of different occurrences (e.g. detector inefficiency, particles that hit some of the planes in pads which were not inside the trigger area, muons interacting with the last plane etc.). Since it was not possible to classify these events, they were not used in further analysis.

Applying a cut of $N_{\text{tot}} < 13$ and $10 \text{ cm} < Z_{\text{COG}} < 30 \text{ cm}$ (see red lines in Fig. 4.12) filters out the electron events from the sample. The cut on the number of hits was chosen to be 13 instead of 16 in order to improve the purity of the muon sample.

This procedure was used in order to select only the muon events for further analysis, resulting in ≈ 13500 muon triggers which were collected and used for the study.

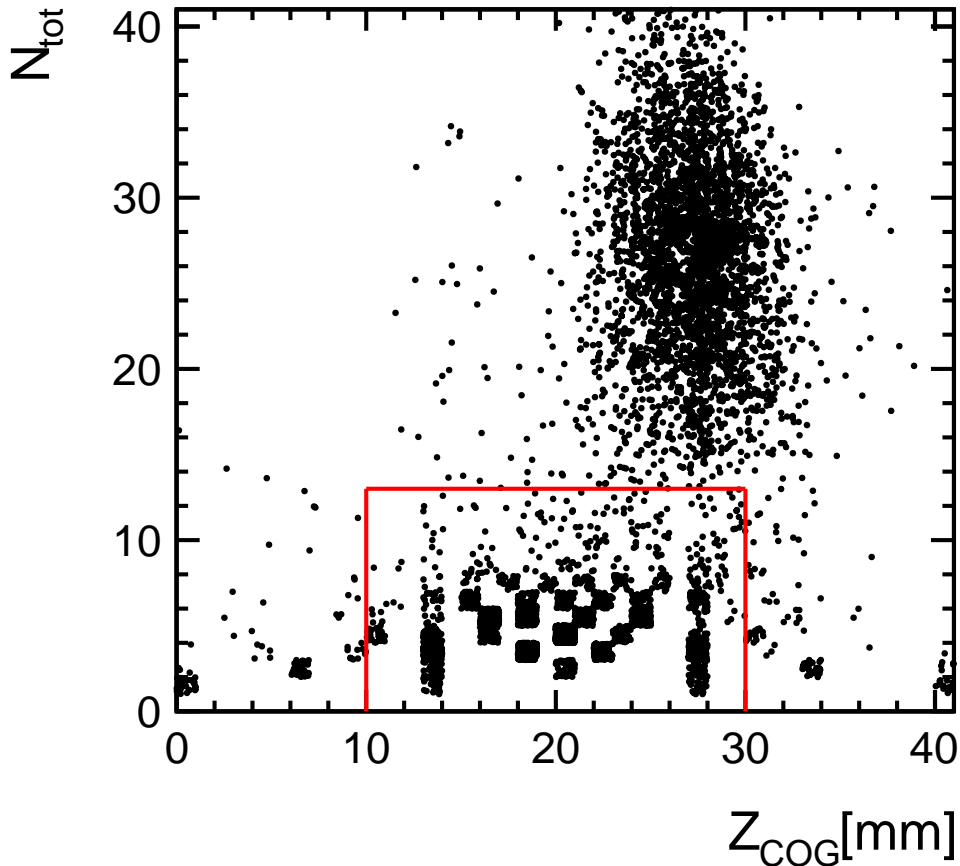


Figure 4.12: Scatter plot of N_{tot} (event total number of hits) vs Z_{COG} (hits' COG coordinate along the beam line) for all events in configuration 1. The events in the region enclosed by the red lines correspond to muon events.

4.2.3 Synchronization with telescope and plane alignment

As mentioned in Section 3.3.3, two clocks existed for the system: the telescope frame number and the TLU number. For each trigger the former was sampled directly from the telescope DAQ and from the AUX, while the latter was saved from the LumiCal DAQ and from the AUX. In order to synchronize between the two subsystems (LumiCal and telescope), the data from both were matched according to these two numbers. The AUX facilitates this by indicating which TLU number matches which frame number, so that if for some reason an event is lost in one subsystem, the corresponding event

in the other subsystem can be ignored. As stated in Section 4.1, in order to minimize problems that come from tracking inaccuracy/inefficiency, only events with a single track in the telescope which passed the track selection criteria were considered for this synchronization process.

Performing this enabled the association of a hit position on the first LumiCal plane (in the telescope reference frame) for each event in LumiCal. This procedure is demonstrated in Fig. 4.13. The hitmap was generated as follows: the location for each hit was taken from the telescope data, while the color coding was assigned according to the channel in the first LumiCal plane which passed the noise threshold in that specific event. The structure

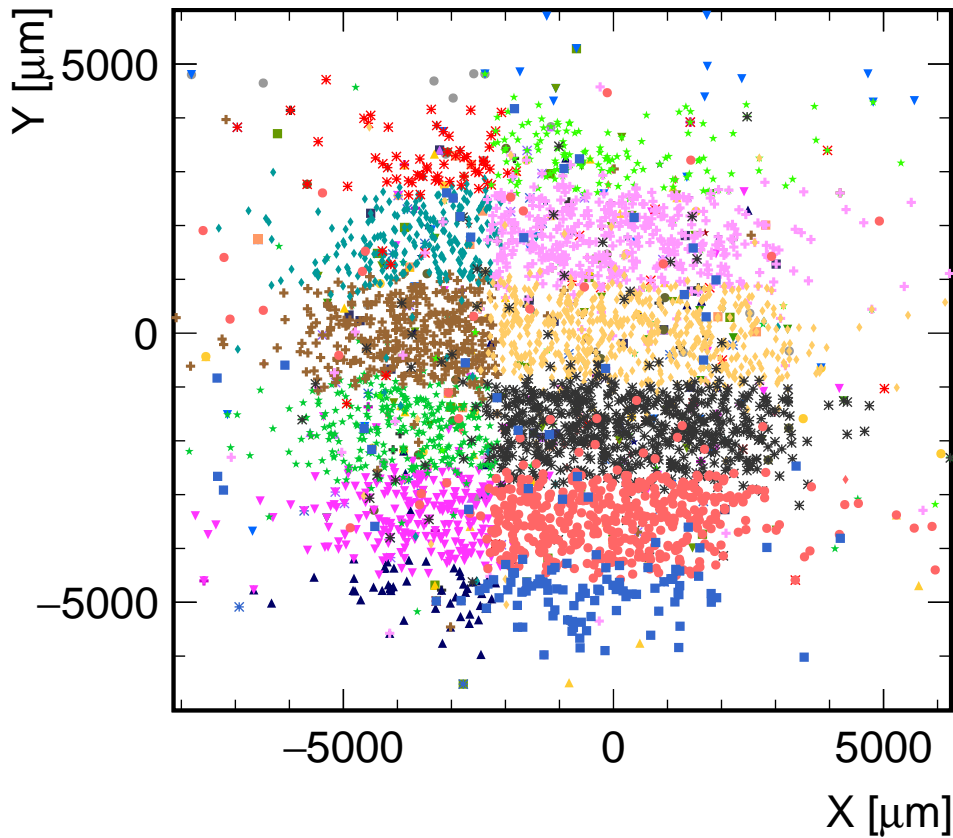


Figure 4.13: Hitmap demonstrating the synchronization process. Inside the circular trigger area the structure of the sensor (borders between pads) can be observed.

of the sensor can be well observed, indicating that the assignment of hit po-

sition matches the data from the LumiCal sensor. The hit positions can be propagated to the next planes of LumiCal, providing similar results. The propagation to the next planes is relevant primarily for muons, which do not interact with the absorber planes and thus reach the next layers as expected from a straight track (electrons and hadrons interact and create showers, resulting in many hits in many different locations).

Hitmaps like the one in Fig. 4.13 can be used for the relative alignment of the LumiCal sensor planes. In order to achieve this, borderlines describing the structure of the pads in the sensor were defined (see, for example, Fig. 4.14). Given a constant and known pad pitch, the entire structure can be parametrized using three parameters, (x, y) location and a rotation angle, α , all given in the reference frame of the tracks from the telescope. Aligning the planes means finding the parameters which best describe the sensor structure as portrayed in the hitmap. In order to do so, an error function was defined,

$$\Delta = \sum_{i=1}^{N_{\text{hits}}} \sigma_i(x, y, \alpha), \quad (4.10)$$

where

$$\sigma_i(x, y, \alpha) = \begin{cases} 0 & \text{if the location of point } i \text{ is inside the pad that showed} \\ & \text{a signal in the corresponding event,} \\ 1 & \text{otherwise.} \end{cases}$$

Minimizing this error function with respect to the three parameters produces the best estimation of the planes' relative location, and enables a common reference when studying position related aspects of the results (as will be presented in Section 4.2.5).

The alignment procedure was carried out for each of the sensor planes, in each of the operating configurations (as the planes may have shifted during the assembly of the additional tungsten plates). The results are presented in Table A.1 in the Appendix.

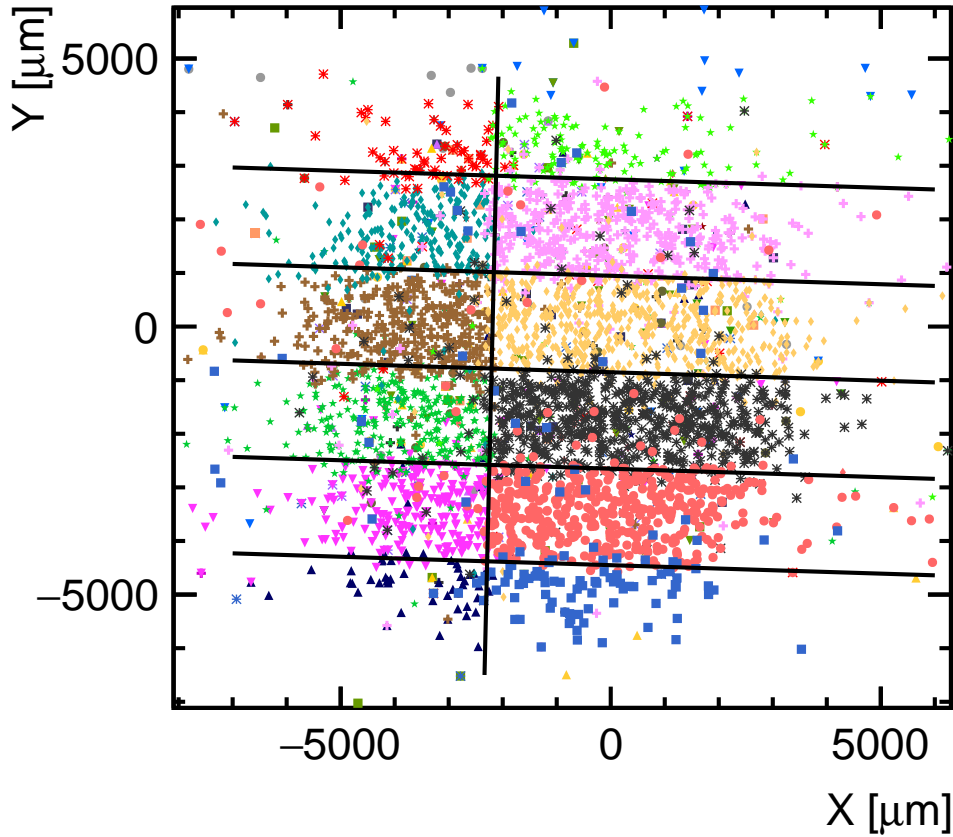


Figure 4.14: The hitmap from Fig. 4.13, with added borderlines.

4.2.4 Sensor signal strength

The ionization which takes place in the silicon sensor transversed by a charged particle is subject to fluctuations, and these fluctuations are significant especially for thin sensors. The main reason for the fluctuations is the rare occurrence of knock-on electrons, with enough energy to become ionizing particles themselves. The distribution of the deposited charge can be described by the Landau function, which is characterized by a most probable value (MPV). This MPV can be used to describe the detector response to MIPs [26].

Due to the electronic system, the signals recorded originate not only from charge deposition but also from noise. This noise is fairly well modeled by a Gaussian distribution around 0. As a result, the distribution of the signal

received from the deposition of charge is a convolution of a Gaussian with the Landau function. A typical example of the signal distribution obtained for muon events in a single readout channel is presented in Fig. 4.15. The Gaussian noise around 0 (left peak) and the convolution of a Gaussian with a Landau function distribution resulting from the signal (right peak) can be observed. On the one hand, a clear separation between the two peaks (signal and noise) can be observed, enabling a selection criterion for signal events. It should be however noted that both distributions have some impurity and that even after selection one remains with some noise events.

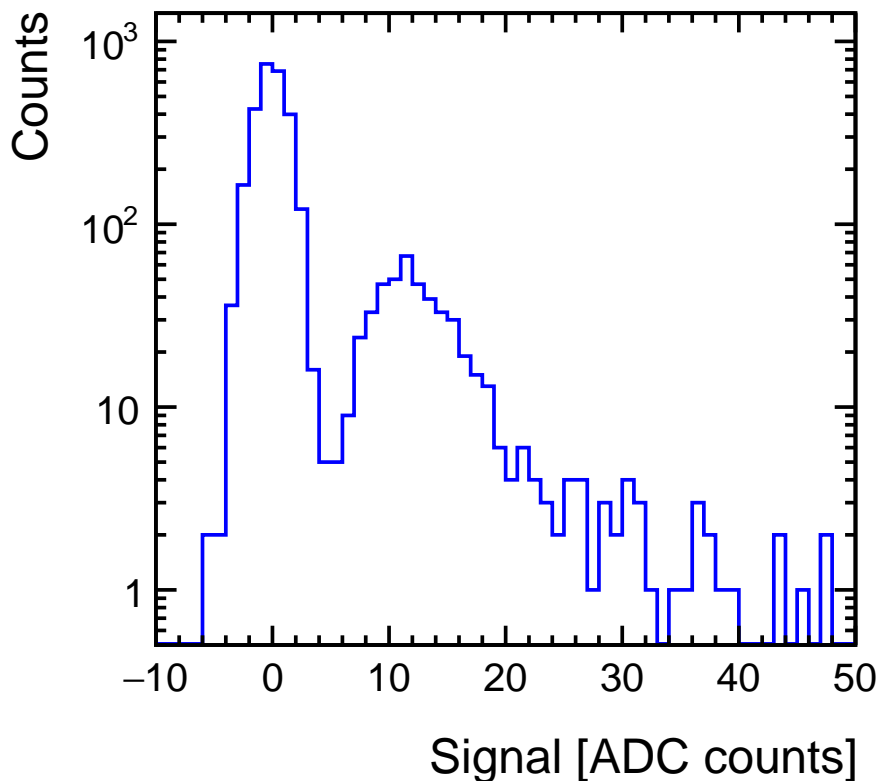


Figure 4.15: The distribution of the signal obtained in channel 22 of plane 1 from all muon events of configuration 1.

In order to test uniformity (both within the sensors and among the sensors), the MPV of the signal was determined for each of the 12 pads which were inside the trigger area, for all sensors. This was accomplished by fitting distributions like the one in Fig. 4.15 to the sum of a Gaussian and a convolution of a Gaussian with a Landau function. An example of such a fit is

displayed in Fig. 4.16a. A ratio plot between the data and the fitted function is displayed in 4.16b. It is worth noting that around the important region of the MPV (left side) the ratio is ≈ 1 .

The MPVs resulting from all of the fits are presented in Fig. 4.17.

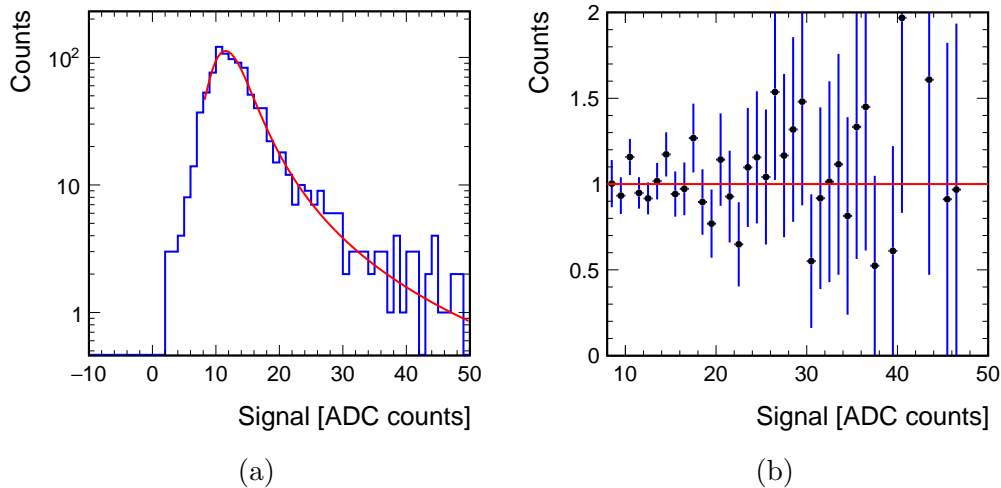


Figure 4.16: (a) A fit of the signal distribution (without events considered as noise) in channel 5 of plane 1. The red line is the result of fitting the expected signal function (see text). (b) Plot of the ratio between the data (vertical blue lines) and the fitted function (red horizontal line).

Figure 4.18 provides a good illustration of the results presented in Fig. 4.17, enabling to test for uniformity. In addition to the MPV result for each pad, a weighted mean for each sensor and is also plotted. While the MPV values from the different pads in each plane are roughly in agreement, a clear difference in the weighted mean values can be seen among the different sensors. In order to further test this conclusion, a different approach was taken. The distribution summed over all pad signals in a plane was fitted in the same manner as detailed above for single pads. Figure 4.19 presents a comparison between the MPVs obtained in this manner and the weighted means of the results of the first approach. A good agreement (up to one standard deviation) between the two approaches can be observed for all sensors, confirming the uniformity within each sensor. Furthermore, a clear difference among the sensors persists, validating the claim that there is indeed a difference in the response among the different sensors. Possible reasons for this could be differences in the manufacturing process, or a variance in the degradation of the various sensors.

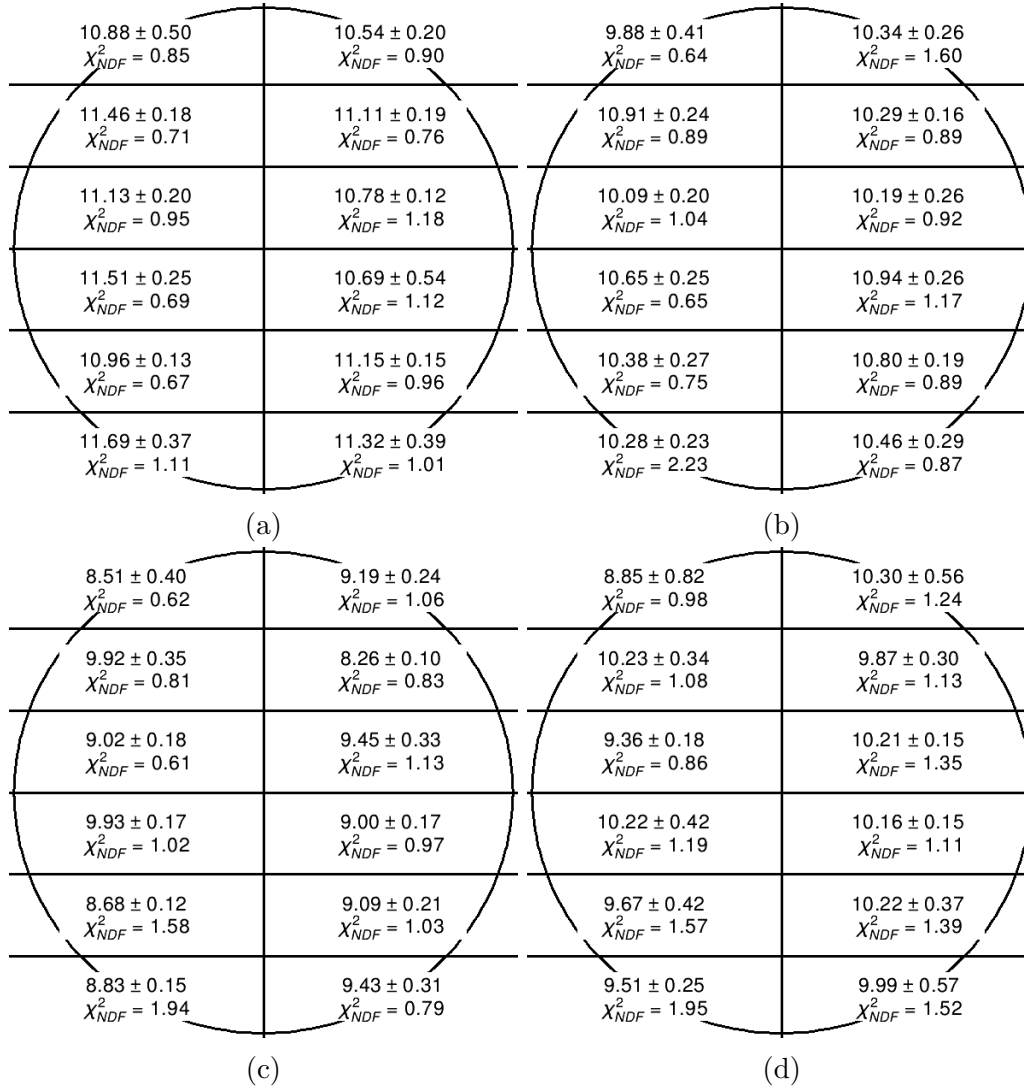


Figure 4.17: Fitted MPVs (most probable value of the signal distribution) for all pads in all planes. Plots (a)-(d) represent planes 1-4, respectively. For each pad the MPV and its uncertainty from the fit are given in units of ADC counts. The χ^2_{NDF} (χ^2/NDF) of the fit is also given.

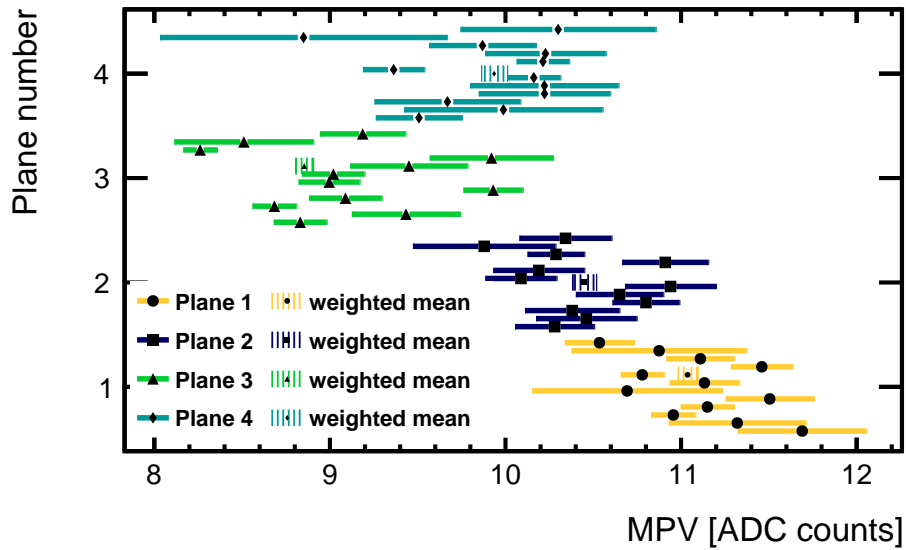


Figure 4.18: Scatter plot of fitted MPVs (most probable value of the signal distribution) for all pads in all planes, with error bars. Different colors represent different planes. Also shown are weighted means of all the results from each of the planes, as described in the legend.

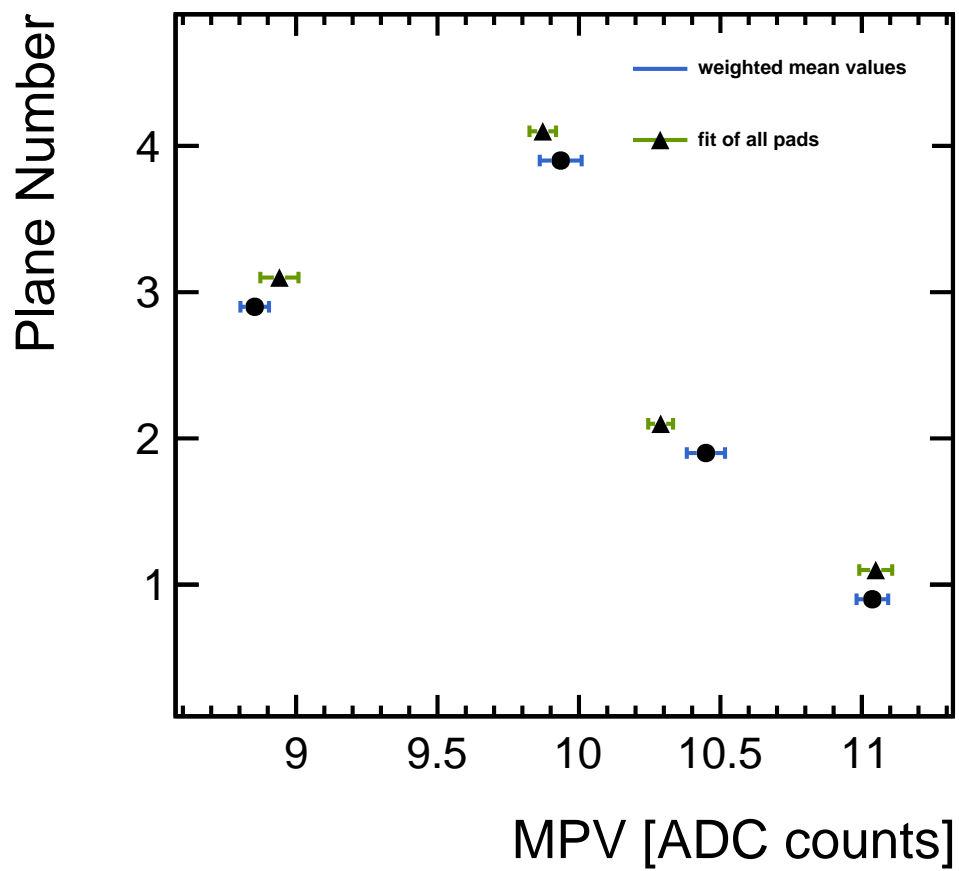


Figure 4.19: Comparison between the MPVs (most probable value of the signal distribution) obtained by fitting the signal from all pads in each plane (filled triangles) and the weighted means of the individual fit results (filled circles)

4.2.5 Charge sharing and position reconstruction

In principle, when studying different aspects of the sensor, one should calibrate the signal values obtained from each channel according to the MPV obtained for it. Signal values are then expressed in MIPs and a common reference value is available for different channels in different sensors. However, this study does not compare the signal from different sensors directly. This fact, combined with the above results that there is no significant difference in the response in different pads of the same sensor, makes the calibration unnecessary. Therefore, the study presented below was carried out without calibrating the signal values.

The pads in the LumiCal sensor are electrically separated. In principle this means that if energy was deposited in a specific pad, charge should be induced in that pad only. In reality, for particles that hit the sensor in an area which is close enough to the edge of a pad, *charge sharing* can be observed. For such a particle, the collected charge is distributed in some manner between the pad that was hit and the adjacent pad (or pads, if the hit was close enough to two edges). This is due to the fact that induced electrons/holes in the area of one pad may affect the electrical field in the neighboring pad. This effect has been previously observed for the LumiCal sensors in beam test studies [21] [38]. In this study, carried out on the muon events only, an attempt was made to characterize this phenomenon for MIPs and develop a method for using charge sharing information in order to perform in-situ reconstruction of MIP hit positions.

For each hit, two relevant pairs of pads were selected in order to measure the magnitude of charge sharing; one for the radial direction and one for the azimuthal direction. The selection was carried out as follows: the primary pad was selected as the pad showing the highest signal from all of the channels inside the trigger area, while demanding that the signal value passes the noise threshold. The second pad is easy to determine for the azimuthal direction as only one possibility exists - the pad that lies "across" from the primary pad (see Fig. 4.14). For the radial direction there are two possibilities - the pad above or below the primary pad. For this case the pad with a higher signal value was selected.

The charge sharing between a given pair of pads was quantified using signal

imbalance (SigImb), defined as follows:

$$\text{SigImb} = \frac{E_1 - E_2}{E_1 + E_2}, \quad (4.11)$$

where E_1 is the energy (in ADC counts) measured in the upper (right) pad of the pair and E_2 is the energy measured in the lower (left) pad. SigImb=1 (-1) means that all the charge was collected from the upper/right (lower/left) pad. For SigImb = 0, the charge is equally distributed between the two pads. Using the alignment parameters obtained for each plane in each configuration, the location of the boundaries in the telescope reference frame can be well defined (as shown in Fig. 4.14). This enables measuring of the distance from a given hit to a desired border (radial or azimuthal). After selecting a pair of pads as described above, the distance between the hit location and the border between the two pads was determined. Another selection which was made for this study is that the distance to the border should not exceed $900 \mu\text{m}$ (half of the pad pitch).

The result of the above is that for each hit, a SigImb value and a distance can be determined. Charge sharing was characterized by investigating the connection between these two quantities.

One such example is shown in Fig. 4.20. The results for all planes in both directions are in Figs. A.4 and A.5 in the Appendix. For most events, especially these which are close to the center of the pad, charge sharing is not visible (SigImb $\approx \pm 1$) confirming that this phenomenon occurs only close to the edges. If one considers the events closer to the edge, a substantial number of hits which display charge sharing can be observed. In order to better demonstrate the connection between the two quantities, a profile plot of Fig. 4.20 is displayed in Fig. 4.21. The profiles for all planes in both directions are in Figs. A.6 and A.7 in the Appendix. It can be clearly seen that a gradual change in SigImb occurs as the hit position approaches the location of the edge. The region that displays charge sharing is estimated to be $\approx \pm 350 \mu\text{m}$ around the edge.

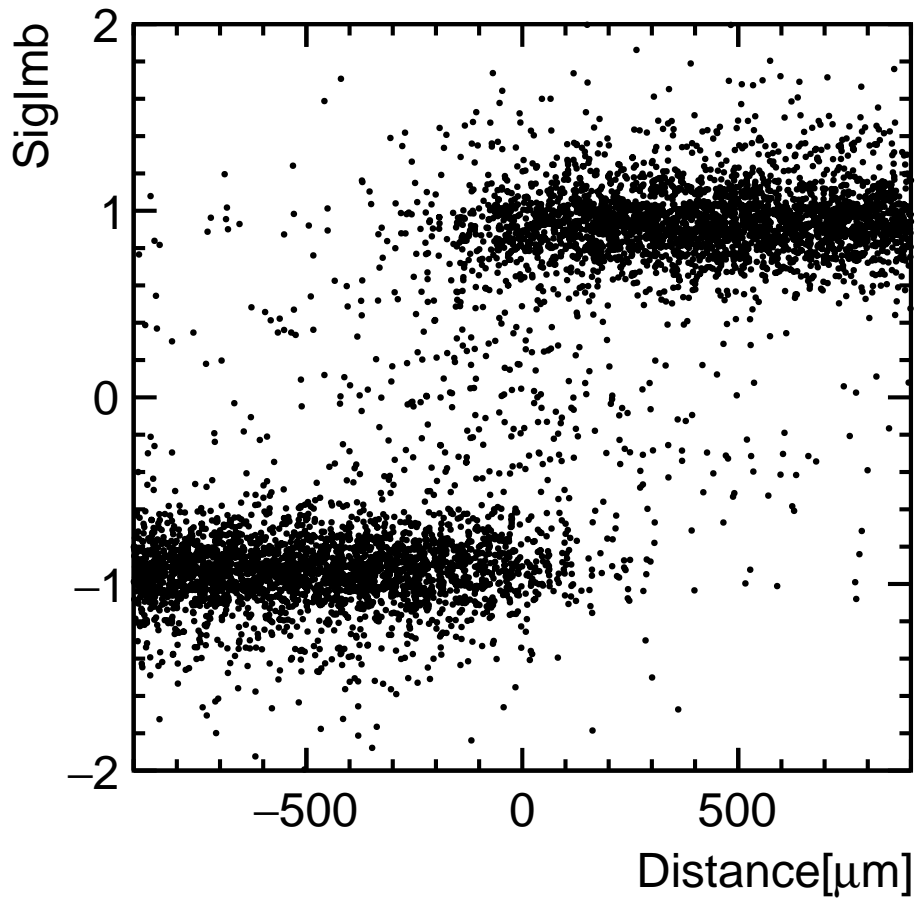


Figure 4.20: A scatter plot of Signal Imbalance (defined in Eq. 4.11) vs the distance to pad edge obtained from the telescope, for the radial direction in plane 1. Positive (negative) distances relative to the pad edge stand for hits which are above (below) the edge.

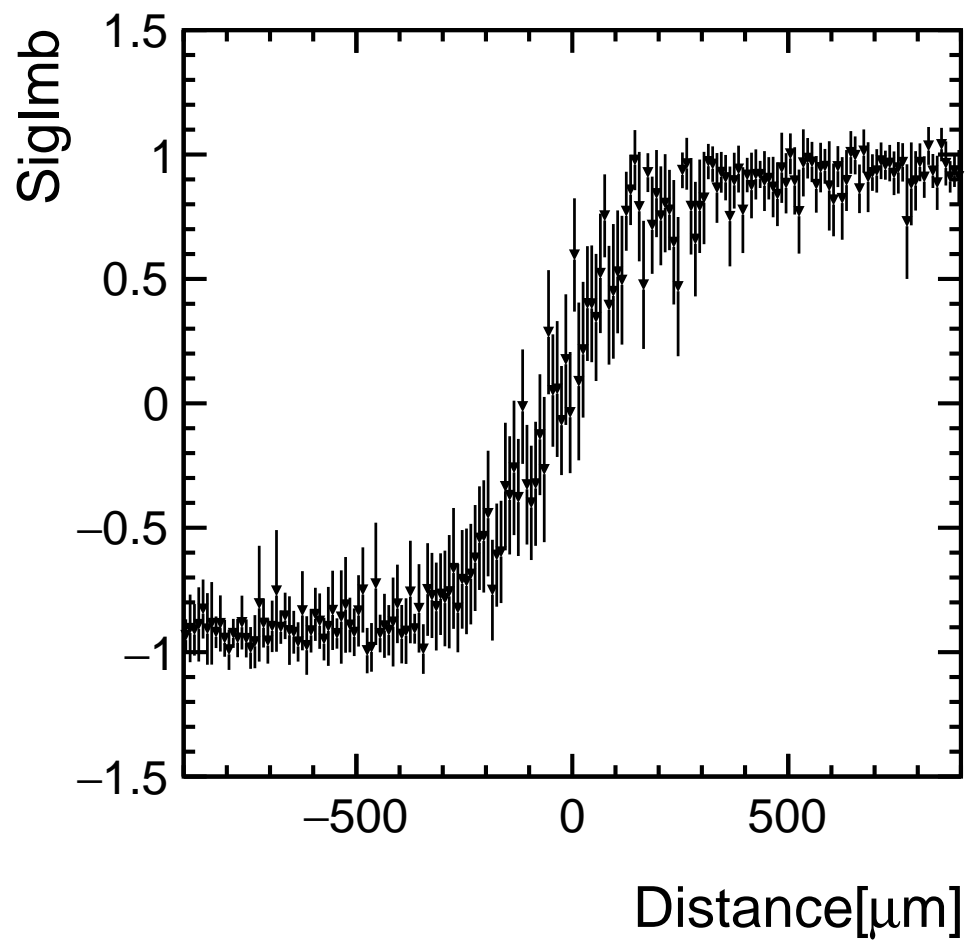


Figure 4.21: A profile plot of Fig. 4.20, computed as a weighted mean of the set of values for each distance bin. The uncertainty is computed as a standard uncertainty ($\frac{\sigma}{\sqrt{N}}$) for the same values.

As mentioned, the distances pad edges were acquired using the data from the telescope. After the profile presented in Fig. 4.21 is mapped, it can be used to define the distance from the edge as a function of SigImb, for the regions of the pad in which charge sharing occurs. This distance reconstruction function is obtained by fitting the profile to an analytic, continuous function. Two such examples are presented in Fig. 4.22, also showing that the relevant events for distance reconstruction fulfill the condition $-0.7 < \text{SigImb} < 0.7$. The results for all planes in both directions are in Figs. A.8 and A.9 in the Appendix. In this manner the distance can be reconstructed from SigImb values only, allowing for this to be done in situ, where a telescope is not available. If for a certain hit the distance in both directions (radial and azimuthal) can be successfully reconstructed, the exact hit position can be determined. This effectively allows for position reconstruction and tracking (in the reference frame of the LumiCal sensors) without a telescope, under the aforementioned limitations.

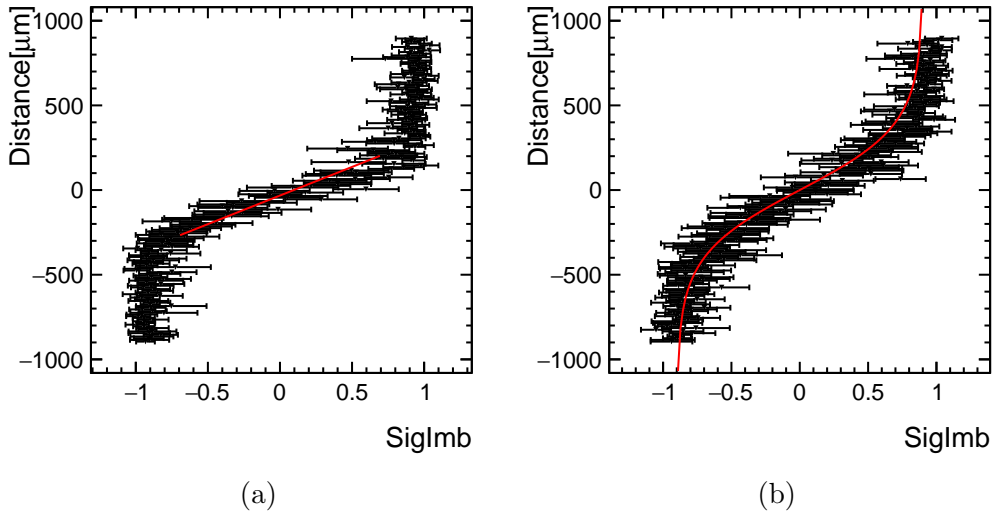


Figure 4.22: Two examples of fit results for a distance reconstruction function: (a) Plane 1 radial direction - linear fit. (b) Plane 4 radial direction - fit to \tanh^{-1} . The data is a 90° rotation of profiles like the one in Fig. 4.21. The red line represents the fitted function.

In order to test the precision of the distance reconstruction function, residuals were calculated. For each SigImb value calculated (i.e. two for each hit - radial and azimuthal) the distance was reconstructed using the distance reconstruction function. This result was compared with the actual position

measured by the telescope for the same hit. For this test, only those hits were selected which were located less than $300\ \mu\text{m}$ from the edge and passed the signal over noise threshold requirement in both pads used for the reconstruction. This results in rather low statistics for the residuals, but guarantees that the SigImb values are accurate and truly represent an instance of charge sharing. The residuals (the difference between reconstructed position and telescope position) distributions are presented in Figs. 4.23 and 4.24, along with fits to a Gaussian function. All residual means are close to 0 within their uncertainties, indicating that the reconstruction function is not shifted systematically with respect to the telescope. The resolution of the reconstruction, evaluated using the standard deviation of the fitted Gaussian, is $\approx 200 - 300\ \mu\text{m}$ for all cases, except for the azimuthal direction of plane 4 (this is probably a result of low statistics).

The above-mentioned resolution is quite large with respect to the width of the charge sharing region. This may be largely due to lack of data; out of the 13500 muon triggers which potentially supply 54000 hits for this study, only ≈ 16000 hits are positioned (according to telescope data) in the area which displays charge sharing. Furthermore, only $\approx 52\%$ of these 16000 are actually usable for the position reconstruction. This is due to the fact that many muon events are "lost in the noise"; as mentioned above, the magnitude of muon signals under the gain conditions which were used is not significantly higher than the noise values. When charge sharing occurs, the signal splits between the two sharing pads, decreasing in size for a given pad. This decreases the probability for the signal to pass the noise threshold, increasing the chance for it to be dismissed as noise. In future board designs for beam test readouts, availability of an option for significantly higher gain for the MIP signals could prevent such issues.

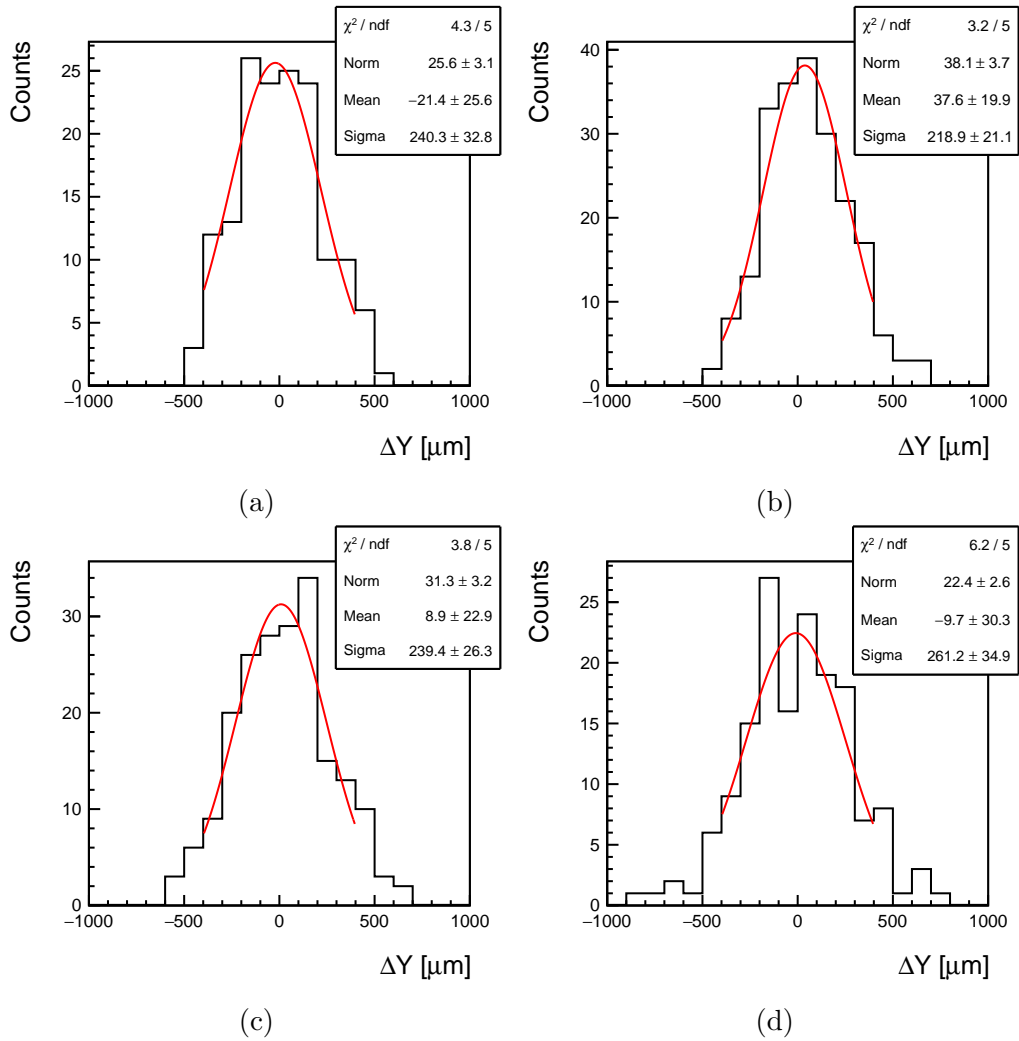


Figure 4.23: Position reconstruction residuals along the radial direction, fitted with a Gaussian function. Plots (a) - (d) represent planes 1-4, respectively.

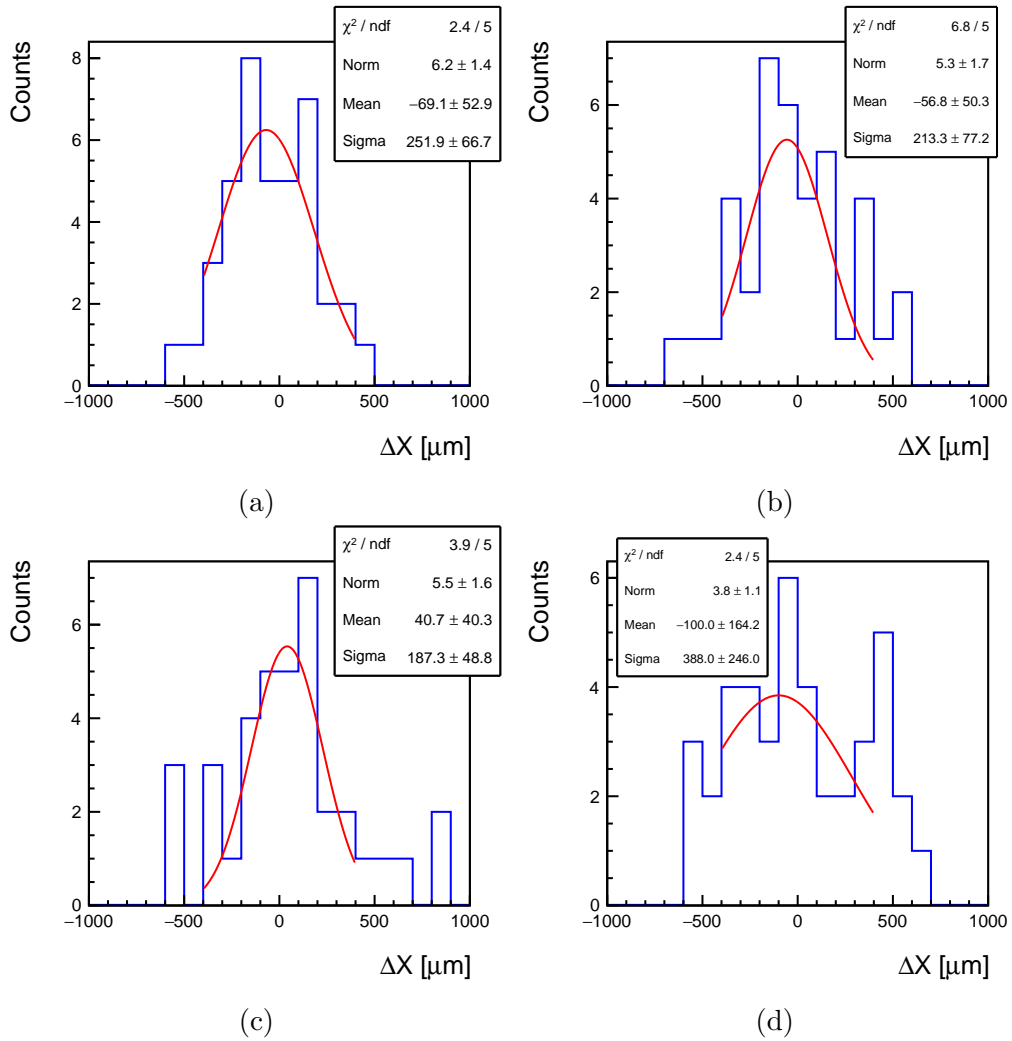


Figure 4.24: Position reconstruction residuals along the azimuthal direction, fitted with a Gaussian function. Plots (a) - (d) represent planes 1-4, respectively.

In spite of the above, it has been shown that position reconstruction is generally achievable, pending more accurate data and more statistics from future beam tests. It is possible to determine the position of a MIP hit (if it is close enough to the border between pads) using SigImb only i.e. without any tracking devices, as will be the state in situ.

4.3 Conclusion

An array of four LumiCal sensor prototypes equipped with a full chain of readout electronics was tested in CERN's PS test-beam facility, including the use of a telescope tracking system. The signals from muons on 12 pads from each plane were investigated. The responses of different pads in each sensor were found to be similar up to a few percent, pointing to uniformity within each sensor of up to one standard deviation between two different calculation procedures. However, a difference in response was recorded among the different planes. The charge sharing of adjacent pads was also investigated and mapped. The ability for reconstruction of a MIP hit position using charge sharing information was investigated and found to be achievable with a resolution of $300\ \mu\text{m}$, but further study in future beam tests may reduce this number.

Summary

The design of the luminosity calorimeter (LumiCal) for a future linear collider is based on a tungsten-silicon sandwich calorimeter. Three such silicon sensors, produced by Hamamatsu, were tested and characterized in the silicon lab of Tel Aviv University. The results were found to be compatible with previous works, and uniformity was found among the different sensors. Measured leakage current and capacitance of pads in corresponding sectors of different sensors display similar trends as a function of the pad size. An array of four sensors equipped with read-out electronics was tested with a 5 GeV beam of electrons, muons and hadrons in CERN's PS test-beam facility. A subsample of muon beam events was selected for the present study, which is the first study of the LumiCal sensors under a muon beam. The response to MIP signals of 12 pads in each sensor was investigated. The signal strength was found to be uniform within each sensor, with signals from different pads in the same sensor being in agreement within the uncertainty. However, a varying response to muon signals was recorded in pads from different sensors. A technique for reconstruction of MIP hit position using charge sharing information is also presented.

The results of this thesis contribute to the understanding of the LumiCal sensors, and bring up the need for additional beam tests with higher statistics and modified readout board designs. Furthermore, the present study is a first attempt in demonstrating that under running conditions, muons can be used to control the stability of the LumiCal response and monitor the geometrical alignment.

Acknowledgements

First, I would like to thank my supervisors, Prof. Halina Abramowicz and Prof. Aharon Levy, for their support and assistance, for introducing me to new ideas and opportunities and for making everything happen.

I would like to thank my friends from our group:

Dr. Alexander Borysov, for assistance with countless matters and lots of good conversations.

Dr. Orel Guetta, for making me a better programmer, for the patience and for the endless e-mail ping-pongs.

Dr. Yan Benhammou and Meny Ben-Moshe, for encouragement and aid in the lab and outside it.

Special thanks go to Itamar Levy, for recruiting and bringing me up into the world particle physics and silicon detectors, for always taking special interest and for constant support in everything I do.

I would like to thank all of the colleagues and friends from the FCAL collaboration, from workshops and test beams.

An enormous gratitude goes to my family for the support during this work, especially to MeyBar and Arbel: you are (sometimes literally) the reason I wake up in the morning.

This work is partly supported by the Israeli Science Foundation, the German-Israel Foundation, the EU Horizon 2020 Research and Innovation programme under Grant Agreement no. 654168 (AIDA-2020), and the I-CORE grant.

Appendix - Additional Plots

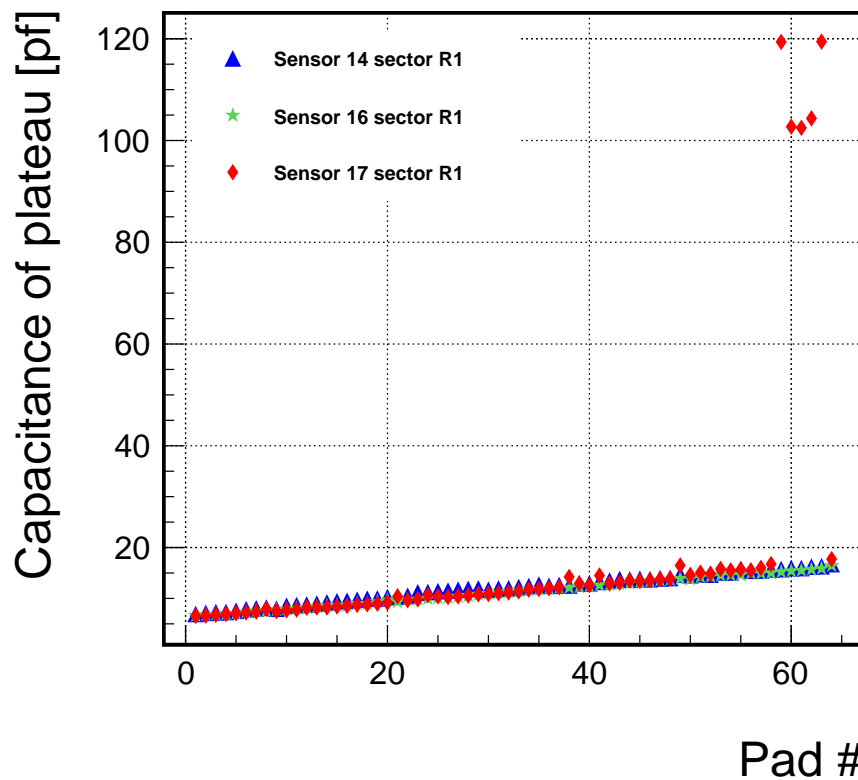


Figure A.1: Capacitance vs pad number in sector R1, with all of the data points. The 5 points from sensor 17 which display very high capacitance values are due to a scratch in the sensor. These points were omitted from Fig. 2.8a in Sec. 2.2.3.2 and are presented here for completeness.

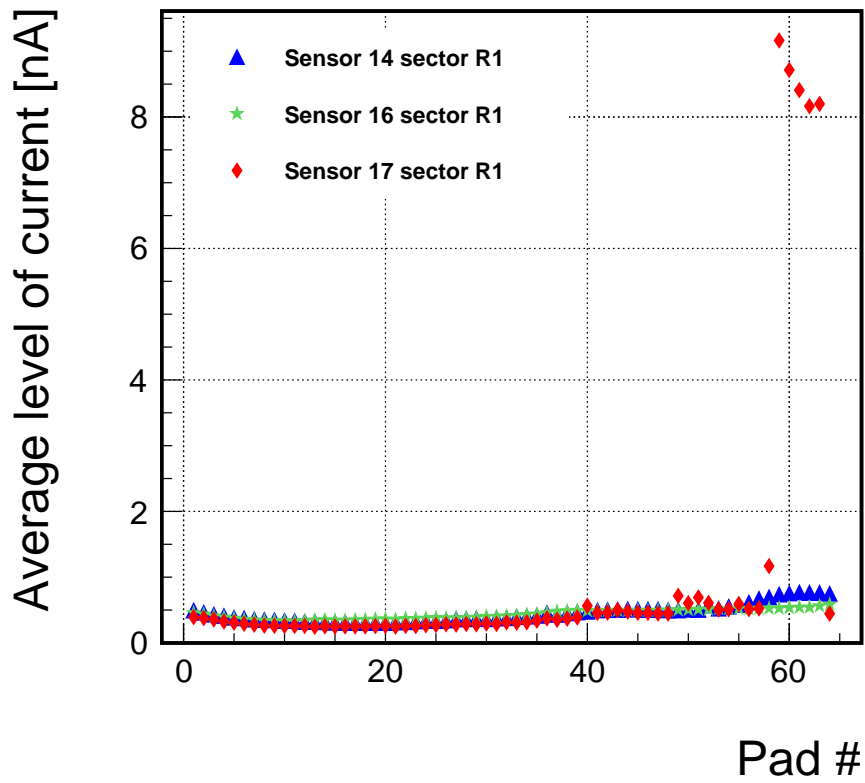


Figure A.2: Current vs pad number in sector R1, with all of the data points. The 5 points from sensor 17 which display very high current values are due to a scratch in the sensor. These points were omitted from Fig. 2.11a in Sec. 2.2.4.1 and are presented here for completeness.

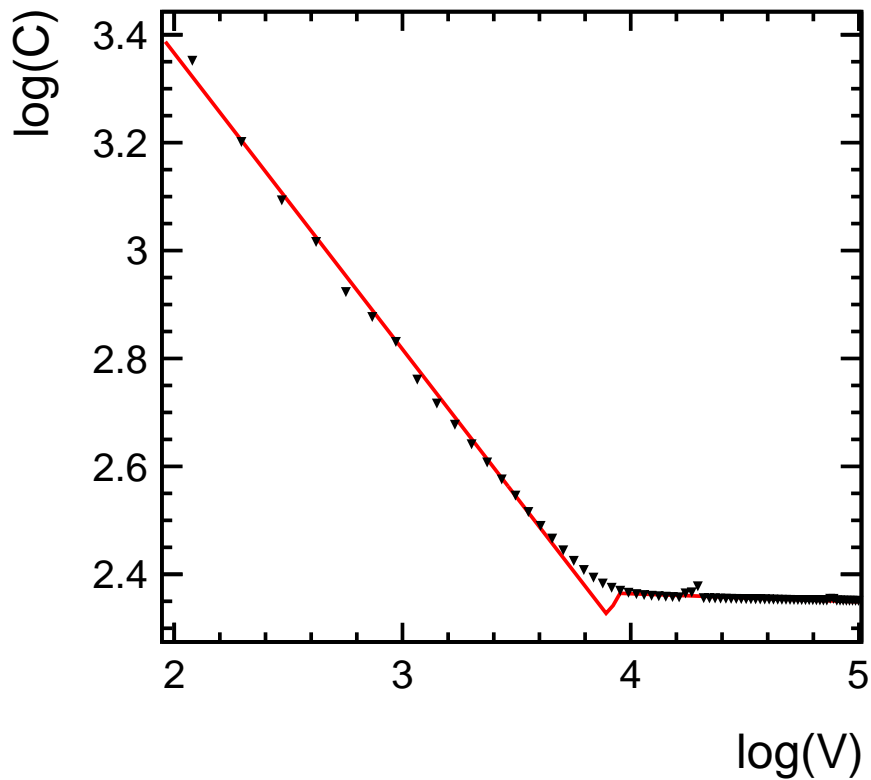
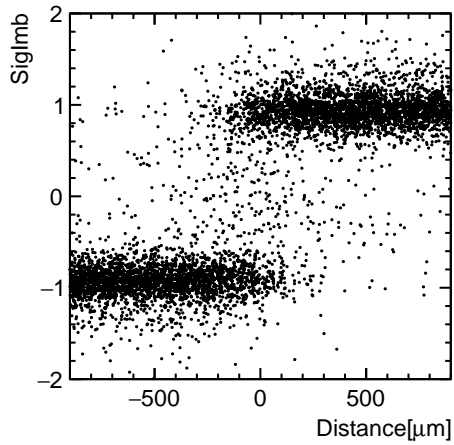
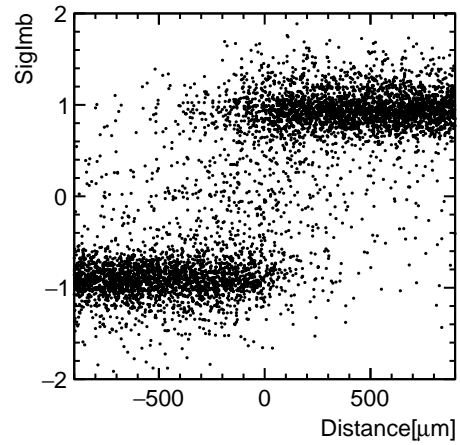


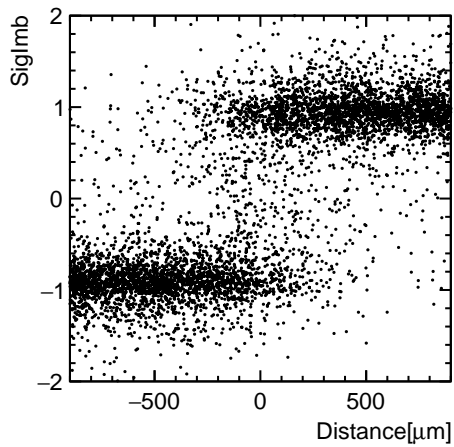
Figure A.3: Fit used to find the depletion voltage. Unlike the one presented in Fig. 2.7, the resulting depletion voltage (represented by the crossing point of the two linear fits) is slightly shifted due to a few stray capacitance measurements in the right region of the graph. This is one of the experimental factors for the wide spread of values obtained for the depletion voltage, as discussed in Sec. 2.2.3.2



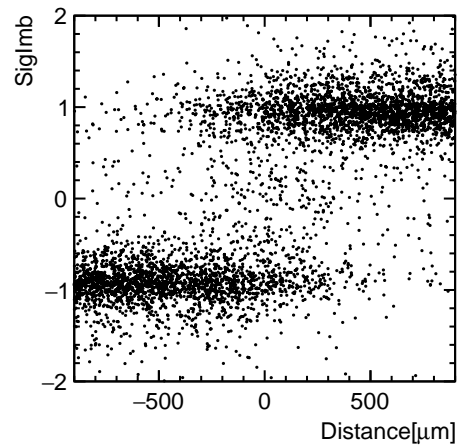
(a)



(b)



(c)



(d)

Figure A.4: A scatter plot of Signal Imbalance (defined in Eq. 4.11) vs the distance to pad edge obtained from the telescope, for the radial direction. One example of such a plot is presented in Fig. 4.20 from Sec. 4.2.5. Plots (a) - (d) represent planes 1-4, respectively.

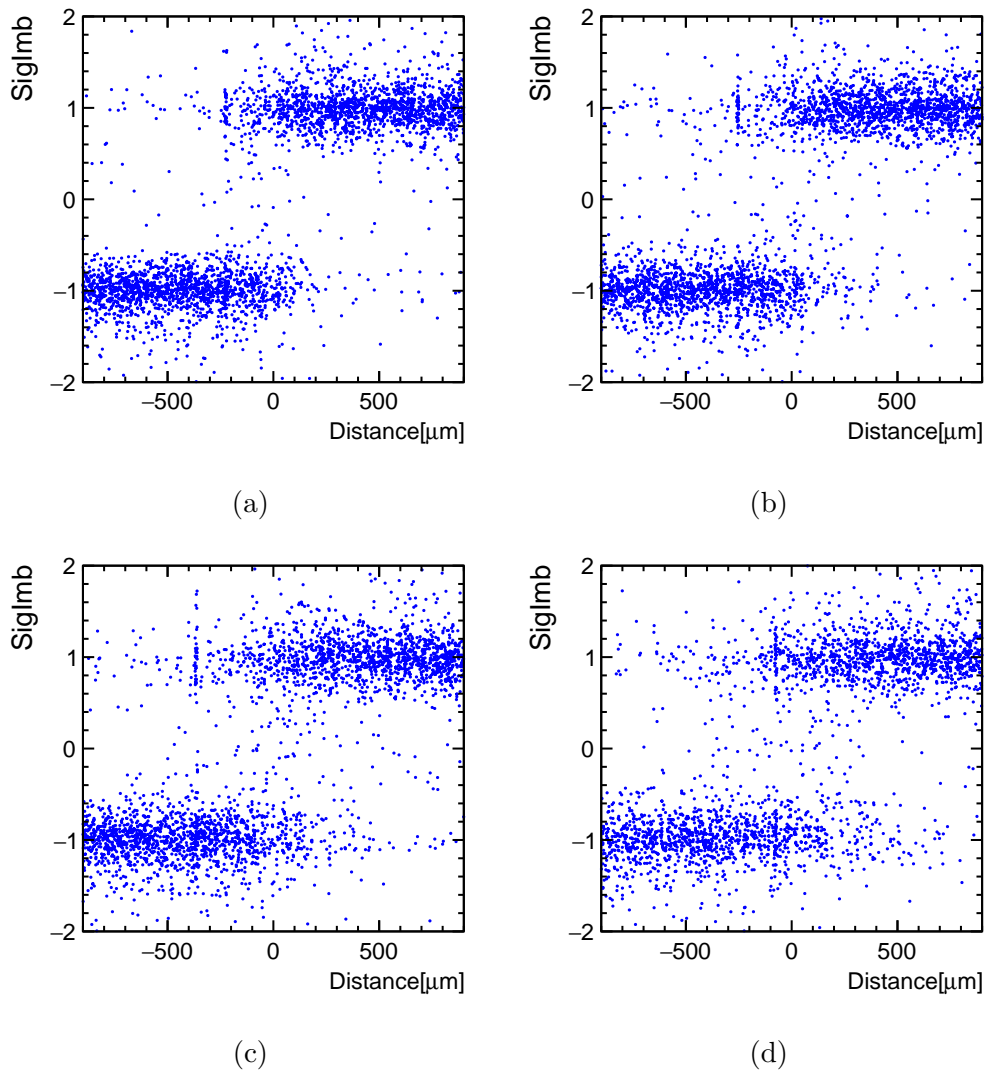


Figure A.5: A scatter plot of Signal Imbalance (defined in Eq. 4.11) vs the distance to pad edge obtained from the telescope, along the azimuthal direction. One example of such a plot is presented in Fig. 4.20 from Sec. 4.2.5. Plots (a) - (d) represent planes 1-4, respectively.

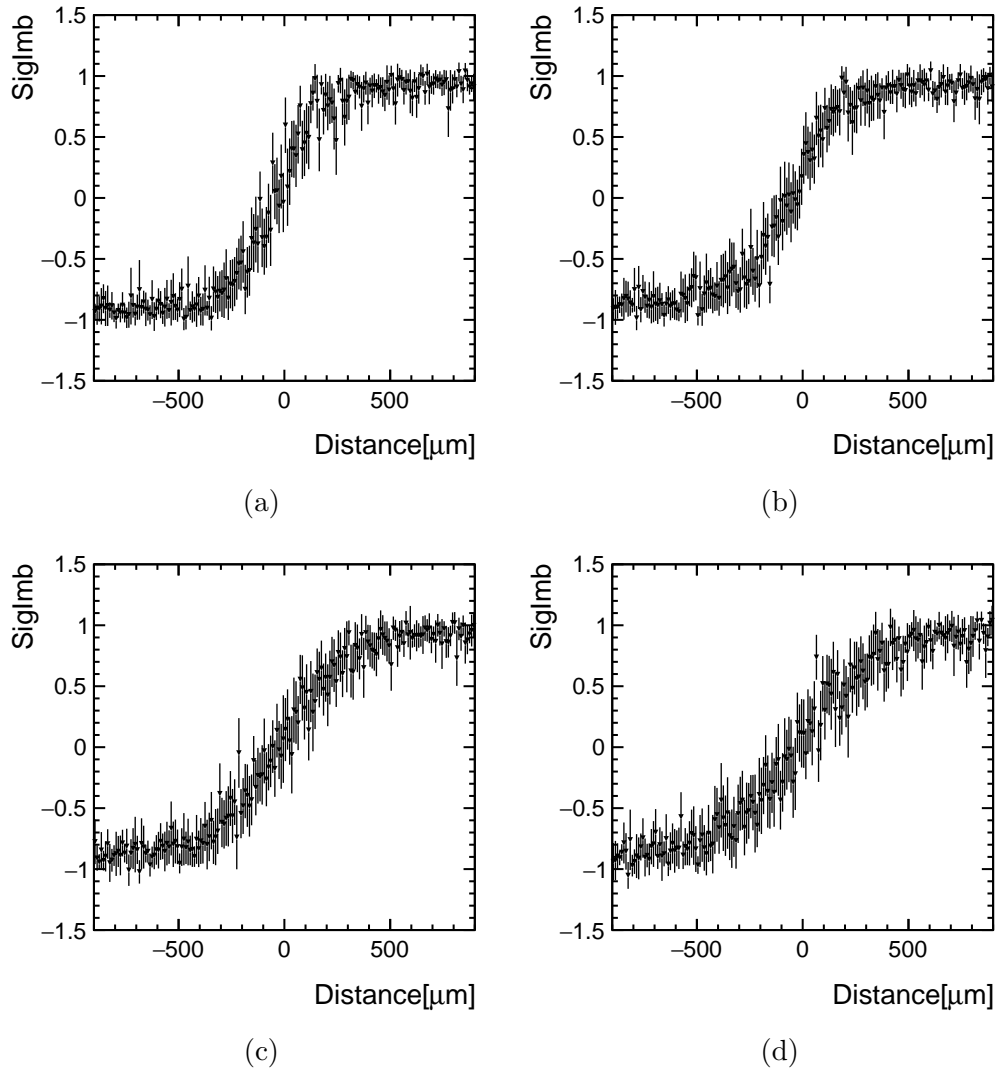


Figure A.6: A SigImb profile plot for the radial direction, computed as a weighted mean of the set of values for each distance bin. The error is computed as a standard error ($\frac{\sigma}{\sqrt{N}}$) for the same values. One example of such a plot is presented in Fig. 4.21 from Sec. 4.2.5. Plots (a) - (d) represent planes 1-4, respectively.

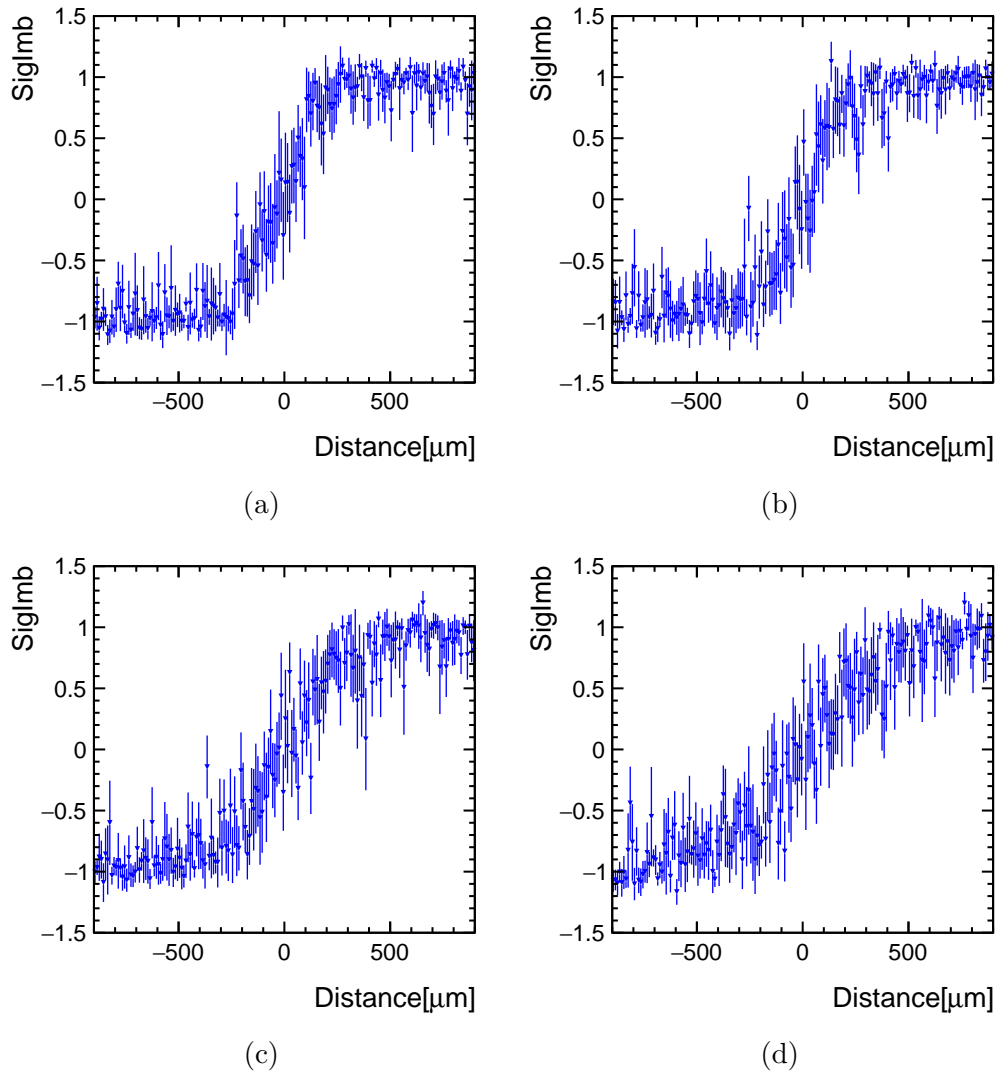
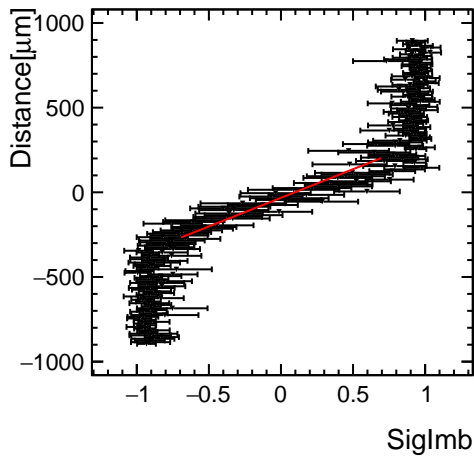
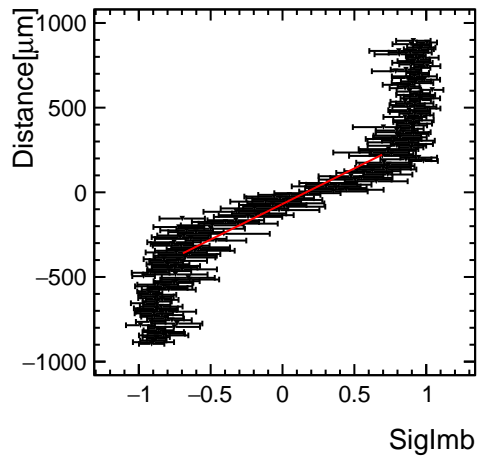


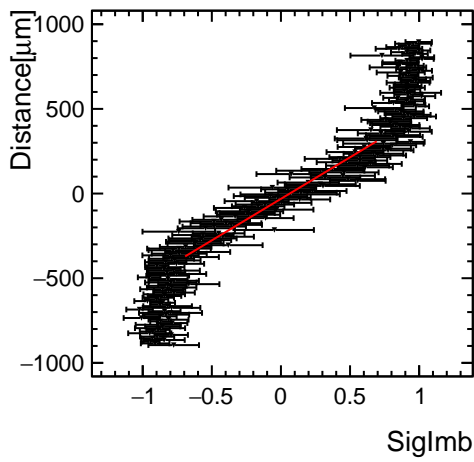
Figure A.7: A SigImb profile plot along the azimuthal direction, computed as a weighted mean of the set of values for each distance bin. The error is computed as a standard error ($\frac{\sigma}{\sqrt{N}}$) for the same values. One example of such a plot is presented in Fig. 4.21 from Sec. 4.2.5. Plots (a) - (d) represent planes 1-4, respectively.



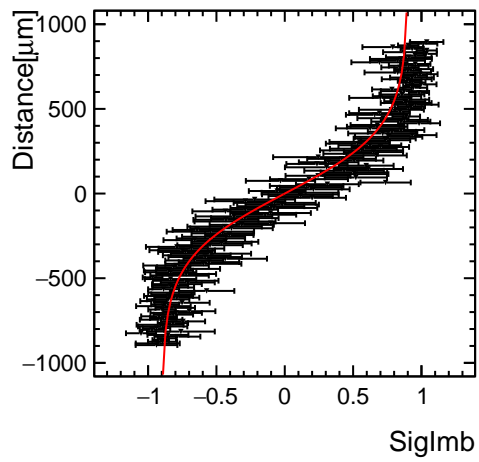
(a)



(b)

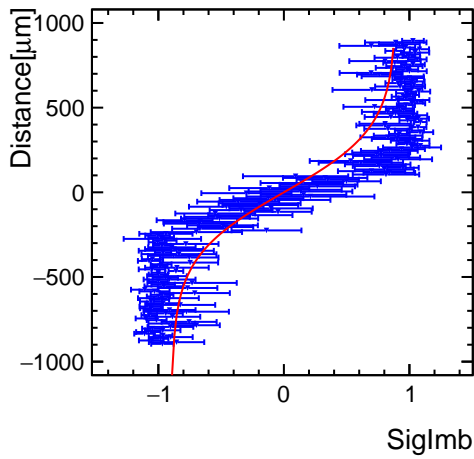


(c)

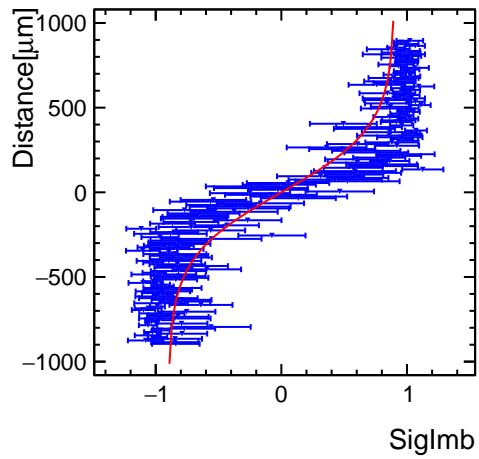


(d)

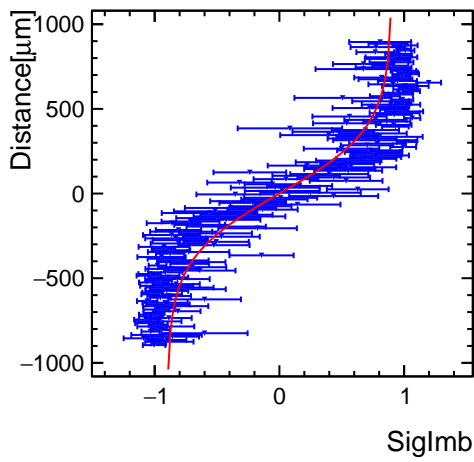
Figure A.8: Fit results for the distance reconstruction functions for the radial direction. The red line represents the fitted function. Two examples of such fits are presented in Fig. 4.22 from Sec. 4.2.5. Plots (a) - (d) represent planes 1-4, respectively.



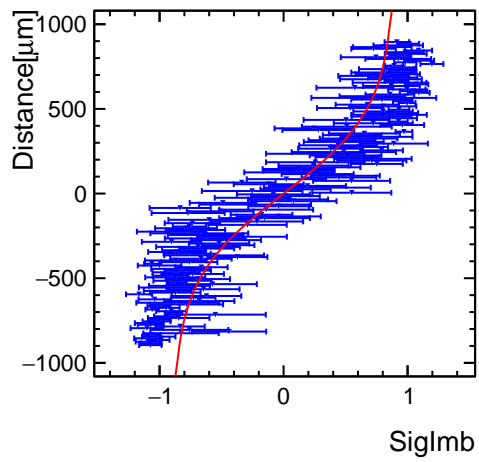
(a)



(b)



(c)



(d)

Figure A.9: Fit results for the distance reconstruction functions along the azimuthal direction. The red line represents the fitted function. Two examples of such fits are presented in Fig. 4.22 from Sec. 4.2.5. Plots (a) - (d) represent planes 1-4, respectively.

Configuration/Plane	$X_{\text{center}}[\mu\text{m}]$	$Y_{\text{center}}[\mu\text{m}]$	$\alpha_{\text{rotation}}[\text{deg}]$
1/1	-2230	-820	2
1/2	-2180	-1030	1.5
1/3	-1930	-710	1.1
1/4	-2230	-550	1
2/1	-2230	-900	1.2
2/2	-2180	-1070	1.4
2/3	-2030	-760	1.1
2/4	-2280	-550	1
3/1	-2230	-900	1.2
3/2	-2180	-1070	1.4
3/3	-2030	-760	1.1

Table A.1: Alignment results for LumiCal planes in all configurations. The results are in the telescope reference frame. The differences among the planes are small but noticeable, whereas the differences among the three configurations for each plane are negligible and are probably a result of statistical fluctuation. The alignment procedure is discussed in Sec. 4.2.3.

Bibliography

- [1] O. S. Brüning, *et al.*, “LHC Design Report,”. Geneva: CERN, 2004. URL: <https://cds.cern.ch/record/782076>.
- [2] G. Aad *et al.*, “Observation of a new particle in the search for the Standard Model Higgs boson with the ATLAS detector at the LHC,” *Phys. Lett.* **B716**, 1 (2012), arXiv:1207.7214.
- [3] S. Chatrchyan *et al.*, “Observation of a new boson at a mass of 125 GeV with the CMS experiment at the LHC,” *Phys. Lett.* **B716**, 30 (2012), arXiv:1207.7235.
- [4] S. Dawson *et al.*, “Working Group Report: Higgs Boson - Community Summer Study 2013: Snowmass on the Mississippi,” 2013, arXiv:1310.8361. URL: <http://inspirehep.net/record/1262795/files/arXiv:1310.8361.pdf>.
- [5] G. Weiglein *et al.*, “Physics interplay of the LHC and the ILC,” *Phys. Rept.* **426**, 47 (2006), hep-ph/0410364.
- [6] T. Behnke, *et al.*, “The International Linear Collider Technical Design Report - Volume 1: Executive Summary,” 2013, arXiv:1306.6327.
- [7] T. Barklow, *et al.*, “ILC Operating Scenarios,” 2015, arXiv:1506.07830.
- [8] L. Linssen, *et al.*, “Physics and Detectors at CLIC: CLIC Conceptual Design Report,” 2012, CERN-2012-003.
- [9] H. Schmickler, *et al.*, “A Multi-TeV Linear Collider based on CLIC technology: Conceptual Design Report.” URL: http://project-clic-cdr.web.cern.ch/project-CLIC-CDR/CDR_Volume1.pdf, 2012.

-
- [10] P. Lebrun, *et al.*, “The CLIC Programme: Towards a Staged e+e- Linear Collider Exploring the Terascale : CLIC Conceptual Design Report,” 2012, CERN-2012-005.
- [11] H. Abramowicz *et al.*, “Physics at the CLIC e+e- Linear Collider – Input to the Snowmass process 2013,” 2013, arXiv:1307.5288.
- [12] The ILD Concept Group, “The International Large Detector: Letter of Intent,” 2010, arXiv: 1006.3396, DESY-2009-87, FERMILAB-PUB-09-682-E, KEK-REPORT-2009-6.
- [13] E. Aihara, H., *et al.*, “SiD Letter of Intent,” 2009, 0911.0006, Letter of Intent for SiD detector concept presented to ILC IDAG.
- [14] M. Vos, “Clic detector and physics status and plans,” 2016. Talk given at CLIC workshop, CERN. URL: <https://indico.cern.ch/event/449801/session/2/contribution/6/attachments/1214266/1772535/clic2016.pdf>.
- [15] H. Abramowicz *et al.*, “Forward Instrumentation for ILC Detectors,” JINST **5**, 12002 (2010), arXiv:1009.2433, DESY-10-142.
- [16] S. Actis *et al.*, “Quest for precision in hadronic cross sections at low energy: Monte Carlo tools vs. experimental data,” Eur. Phys. J. **C66**, 585 (2010), arXiv:0912.0749.
- [17] C. M. Carloni Calame, *et al.*, “NNLO massive corrections to Bhabha scattering and theoretical precision of BabaYaga@NLO,” Nucl. Phys. Proc. Suppl. **225**, 293 (2012), arXiv:1112.2851.
- [18] K. Moenig, “Physics needs for the forward region,” AUG 2004. Talk given at the FCAL Meeting, Zeuthen. URL: https://www-zeuthen.desy.de/lcdet/Aug_04_WS/talks/moenig_lum04.pdf.
- [19] H. Abramowicz, *et al.*, “A luminosity detector for the International Linear Collider,” 2007, LC-DET-2007-006. URL: <http://alzt.tau.ac.il/~ronen/msc/msc.pdf>.
- [20] I. Sadeh, “Luminosity Measurement at the International Linear Collider,” MSc thesis, Tel Aviv University, 2008. URL: <http://inspirehep.net/record/874739/files/arXiv:1010.5992.pdf>.

-
- [21] I. Levy, “Detector development for the instruments in the forward region of future linear colliders,” MSc thesis, Tel Aviv University, 2012. URL: <https://cds.cern.ch/record/1605236/files/CERN-THESIS-2012-346.pdf>.
- [22] R. Schwartz, “Luminosity measurement at the compact linear collider,” MSc thesis, Tel Aviv University, 2012. URL: http://inspirehep.net/record/1296574/files/601251587_CERN-THESIS-2012-345.pdf?version=1.
- [23] E. J. Bwocki, W. Daniluk *et al.*, “Silicon Sensors Prototype for LumiCal Calorimeter,” Dec 2009, EUNET-Memo-2009-07.
- [24] M. Bergholz, “I/V and C/V Measurements on Hamamatsu Si - Detectors,” Jun 2009. FCAL Meeting, Zeuthen. URL: <https://indico.desy.de/getFile.py/access?contribId=14&sessionId=0&resId=0&materialId=slides&confId=2000>.
- [25] A. Cerdeira *et al.*, “Analytical expressions for the calculation of pixel detector capacitances,” IEEE Transactions on Nuclear Science **44**, 63 (1997).
- [26] L. Rossi, “Pixel detectors: from fundamentals to applications,” Particle acceleration and detection, Springer, 2006.
- [27] “FCAL Collaboration.” URL: <http://fcal.desy.de/>.
- [28] H. Abramowicz *et al.*, “Performance of fully instrumented detector planes of the forward calorimeter of a Linear Collider detector,” JINST **10**, P05009 (2015), arXiv:1411.4431.
- [29] “CERN East Area documentation.” URL: <http://sba.web.cern.ch/sba/BeamsAndAreas/East/East.htm>.
- [30] “MIMOSA 26 information.” URL: <https://twiki.cern.ch/twiki/bin/view/MimosaTelescope/MIMOSA26>.
- [31] F. X. Nuiry, “Detailed description of tungsten plates used for TB 2014.” URL: <https://agenda.linearcollider.org/event/6856/contribution/4/material/slides/1.pdf>.
- [32] F. X. Nuiry, “Update on the mechanical infrastructure for fcal tests - preparation for test beam,” OCT 2013. Talk given at the FCAL Meeting, Zeuthen

- URL: <https://indico.desy.de/getFile.py/access?contribId=15&sessionId=6&resId=0&materialId=slides&confId=8669>.
- [33] “TAF - Telescope A Pixel Analysis Framework.” URL: <http://www.iphc.cnrs.fr/TAF.html>.
- [34] O. Rosenblat, “Status of testbeam telescope data analysis,” MAR 2015. Talk given at the FCAL Meeting, CERN.
URL: https://indico.cern.ch/event/349308/contribution/1/attachments/689919/947470/Oron_telescope_talk.pdf.
- [35] J. Moron, “LumiCal boards calibration.” URL: https://asic.fis.agh.edu.pl/fcal/lumi_calibration.pdf.
- [36] S. Gadomski, *et al.*, “The Deconvolution method of fast pulse shaping at hadron colliders,” Nucl. Instrum. Meth. **A320**, 217 (1992).
- [37] O. Novgorodova, “Characterisation and Application of Radiation Hard Sensors for LHC and ILC,” PhD thesis, Brandenburg Tech. U., 2013. URL: <http://www-library.desy.de/cgi-bin/showprep.pl?thesis13-052>.
- [38] S. Kulis, “Development of prototype luminosity detector modules for future experiments on linear colliders,” PhD thesis, AGH-UST, Cracow, Dec 2012. URL: <https://cds.cern.ch/record/1613815>.
- [39] T. Preda, “A method for muon-electron discrimination in the Lumi-Cal test-beam.” URL: <https://agenda.linearcollider.org/event/6846/contribution/3/material/slides/>.

תקציר

התכנון של גלאי לומינוסיטי המיועד למאיצים ליניארים עתידיים מבוסס על מכלול מדידת אנרגיה שכבתי הבנוי משכבות של טונגסטו וסיליקון. שלושה חיישני סיליקון שיוצרו ע"י חברת Hamamatsu נבחנו ונמדדו במעבדת הסיליקון של אוניברסיטת תל אביב. התוצאות מצביעות על אחידות בתכונות החשמליות בין החיישנים השונים. מערך של ארבעה חיישני סיליקון המצוידים ברכיבי קריאה אלקטרונית נבחנו באמצעות קרן מיואונים של 5 מיליארד אלקטרון וולט (GeV) ב CERN בז'נבה. התוצאות מעידות על אחידות בתגובה לאותות בתוך כל חיישן, ולהבדל קל בין החיישנים השונים. כמו כן, מוצגת בעבודה זו טכניקה לשחזור מיקום פגיעתו של חלקיק מיון מינימלי (MIP) על ידי שימוש במידע לגבי חלוקת מטען בין תאי החיישן.

אוניברסיטת תל-אביב
הפקולטה למדעים מדויקים
ע"ש ריימונד וברלי סאקלר

אחידות גללים עבור מכלולי המדידה באיזור הקידמי
של מאיצים לינאריים עתידיים.

חיבור זה הוגש כחלק מהדרישות לקבלת התואר
מוסמך אוניברסיטה (M.Sc.) באוניברסיטת תל אביב
בבית הספר לפיזיקה ואסטרונומיה

על ידי
אורון רוזנבלט

12 בספטמבר 2016

המחקר לעבודה זאת נעשה במחלקה לאנרגיות גבוהות באוניברסיטת תל
אביב בהדרכת פרופסור **הלינה אברמוביץ'** ופרופסור **אהרן לוי**.